Characterization of Facies and Permeability Patterns in
Carbonate Reservoirs Based on Outcrop Analogs

Final Report

By

Charles Kerans
F.J. Lucia
R.K. Senger
G.E. Fogg
H.S. Nance
S.D. Hovorka

July 1993

Work Performed Under Contract No. DE-AC22-89BC14470

QAe7708

DISCLAIMER

CONTENTS

FIGURES

TABLES

SUMMARY

More than 13 billion barrels (Bbbl) of mobile oil and 17 Bbbl of residual oil will remain in San Andres and Grayburg reservoir at abandonment under current development practices. Through development and application of new recovery technology a large part of this resource can be recovered. This report focuses on research for the development and testing of new techniques for improving recovery of this resource. Outcrop and subsurface geologic and engineering data are utilized to develop new methodologies through the integration of geologic observations and engineering data for improving numerical models that predict reservoir performance more accurately.

Extensive regional mapping of the 14-mi by 1,200-ft San Andres outcrop, located on the Algerita Escarpment, Guadalupe Mountains, New Mexico, demonstrates that the San Andres carbonate-ramp complex is composed of multiple depositional sequences that have significant basinward shifts in reservoir-quality facies tracts occurring across sequence boundaries. Detailed geologic and petrophysical mapping of three reservoir-quality facies tracts demonstrates that the fundamental scale of geologic description for reservoir characterization is the parasequence and its component rock-fabric-based facies. Descriptions of cores from the Seminole San Andres Unit illustrate that the parasequence is also the fundamental geologic scale for reservoir mapping in the subsurface.

Outcrop and subsurface petrophysical data show that the parasequence framework can be quantified in petrophysical terms through rock-fabric-based transforms. Three basic rock-fabric/petrophysical classes, each having distinct porosity, permeability, and saturation characteristics, can be used to quantify both the outcrop and subsurface. In the outcrop, these relationships are used to convert permeability and rock-fabric data into porosity and saturation values. In the subsurface, these relationships together with relationships between rock-fabric, acoustic travel time, and resistivity are used to transform wireline log data into porosity, permeability, and saturation values.

The problem of characterizing the petrophysical properties on an interwell scale was approached geostatistically. Statistically significant differences in permeability occur between rock-fabric facies. Variogram analysis of closely spaced permeability data within a rock-fabric unit shows a high degree of variability which is near random on the small scale. Flow modeling experiments of a single rock-fabric unit show that a facies-averaged geometric-mean permeability can be used to predict recovery efficiency. To predict production rate, however, conditional simulations using a long-scale permeability structure are required.

Reservoir-flow simulations of the 2,500-ft-long by 160-ft-high package of parasequences located at Lawyer Canyon underscore the importance of knowing the rock-fabric architecture between wells. Results from this research show that the spatial distribution of facies relative to the waterflood direction can significantly affect how the reservoir produces. Bypassing of unswept oil occurs due to cross flow of injected water from high permeability zones into lower permeability zones where high permeability zones terminate. An area of unswept oil develops because of the slower advance of the water-injection front in the lower permeability zones. When the injection pattern is reversed, the cross-flow effect changes due to the different arrangements of rock-fabric flow units relative to the flow of injected water, and the sweep efficiency is significantly different. Flow across low-permeability mudstones occurs showing that these layers do not necessarily represent flow barriers.

INTRODUCTION

Objectives

The primary objective of this research is to develop methods for better describing the three-dimensional geometry of carbonate reservoir flow units as related to conventional or enhanced recovery of oil. San Andres and Grayburg reservoirs were selected for study because of the 13 Bbbl of remaining mobile oil and 17 Bbbl of residual oil in these reservoirs. The key data base is provided by detailed characterization of geologic facies and rock permeability in

reservoir-scale outcrops of the Permian San Andres Formation in the Guadalupe Mountains of New Mexico. Emphasis is placed on developing an outcrop analog for San Andres strata that can be used as (1) a guide to interpreting the regional and local geologic framework of the subsurface reservoirs and (2) a data source illustrating the scales and patterns of variability of rock-fabric facies and petrophysical properties, particularly in lateral dimension, and on scales that cannot be studied during subsurface reservoir characterization. The research approach taken to achieve these objectives utilizes the integration of geologic description, geostatistical techniques, and reservoir flow simulation experiments.

OUTCROP ANALOG MAPPING, ALGERITA ESCARPMENT

Geologic Setting of the San Andres Formation, Algerita Escarpment

Outcrop studies for the San Andres/Grayburg Reservoir Characterization Research Laboratory (RCRL) were located in the northern Guadalupe Mountains where complete exposures of the San Andres lie in this northwest corner of the Northwest Shelf (figs. 1 and 2). The key exposure, the Algerita Escarpment, contains a 1,200-ft-thick San Andres section spanning 17 mi of oblique-dip carbonate-ramp profile with a diverse array of carbonate-ramp facies (figs. 3 and 4). The combination of superb exposure on the Algerita Escarpment and the proximity of these outcrops to reservoirs of equivalent angle and geologic setting (fig. 1) made it the ideal spot for evaluating the utility of outcrop heterogeneity models used for interpreting equivalent subsurface reservoirs.

Sequence-Stratigraphic Studies for Reservoir Framework Analysis

The application of sequence-stratigraphic concepts, first developed for exploration and basin evaluation applications, proved useful for constructing both regional and interwell-scale geologic models used in production geology studies. The depositional sequence provides a
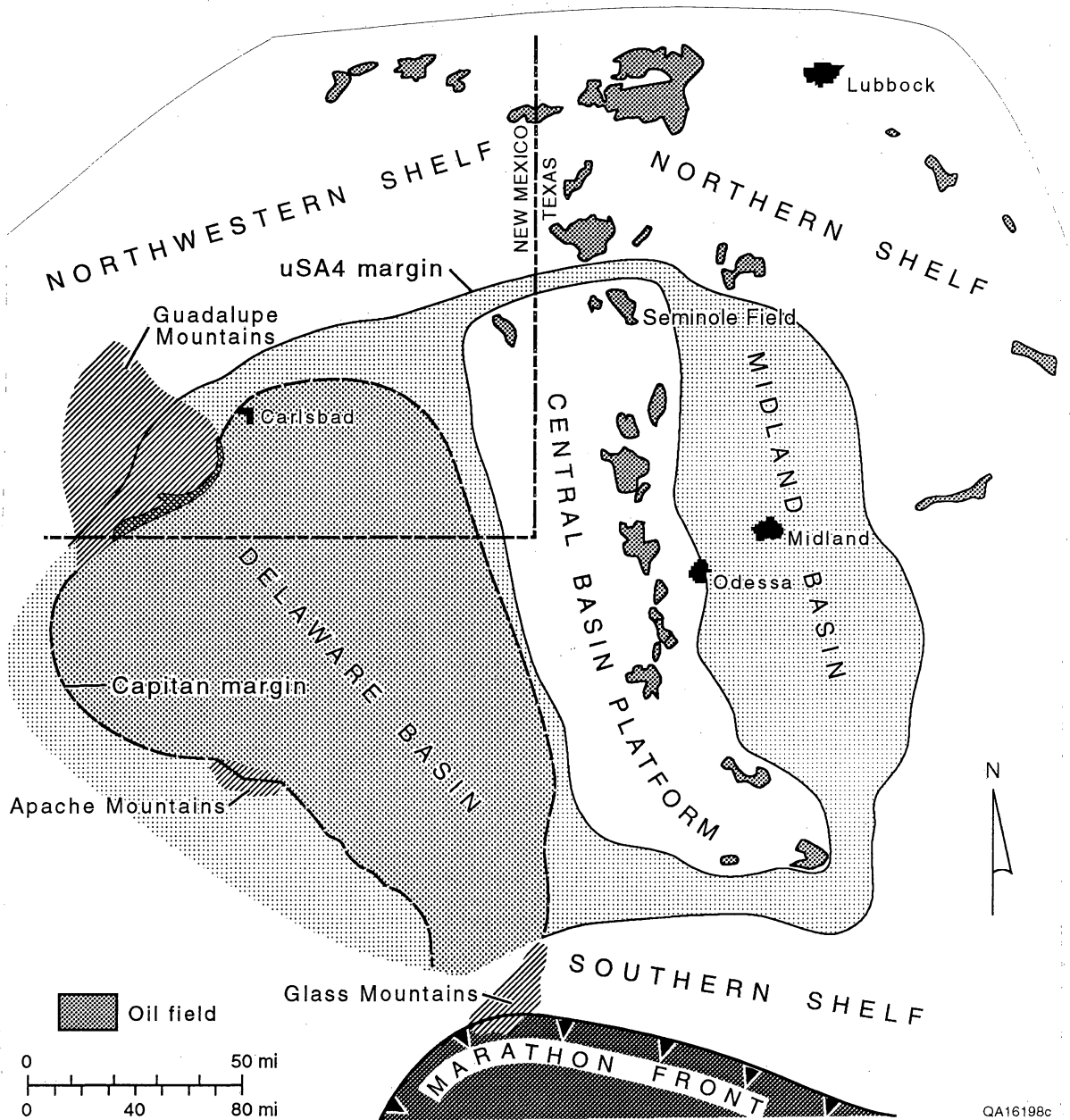
Figure 1. Generalized paleogeographic setting of the San Andres Formation, Permian Basin, showing San Andres reservoirs that have produced more than 10 MMbbl of oil. Also shown are the Guadalupe Mountain outcrop area and the Seminole field.
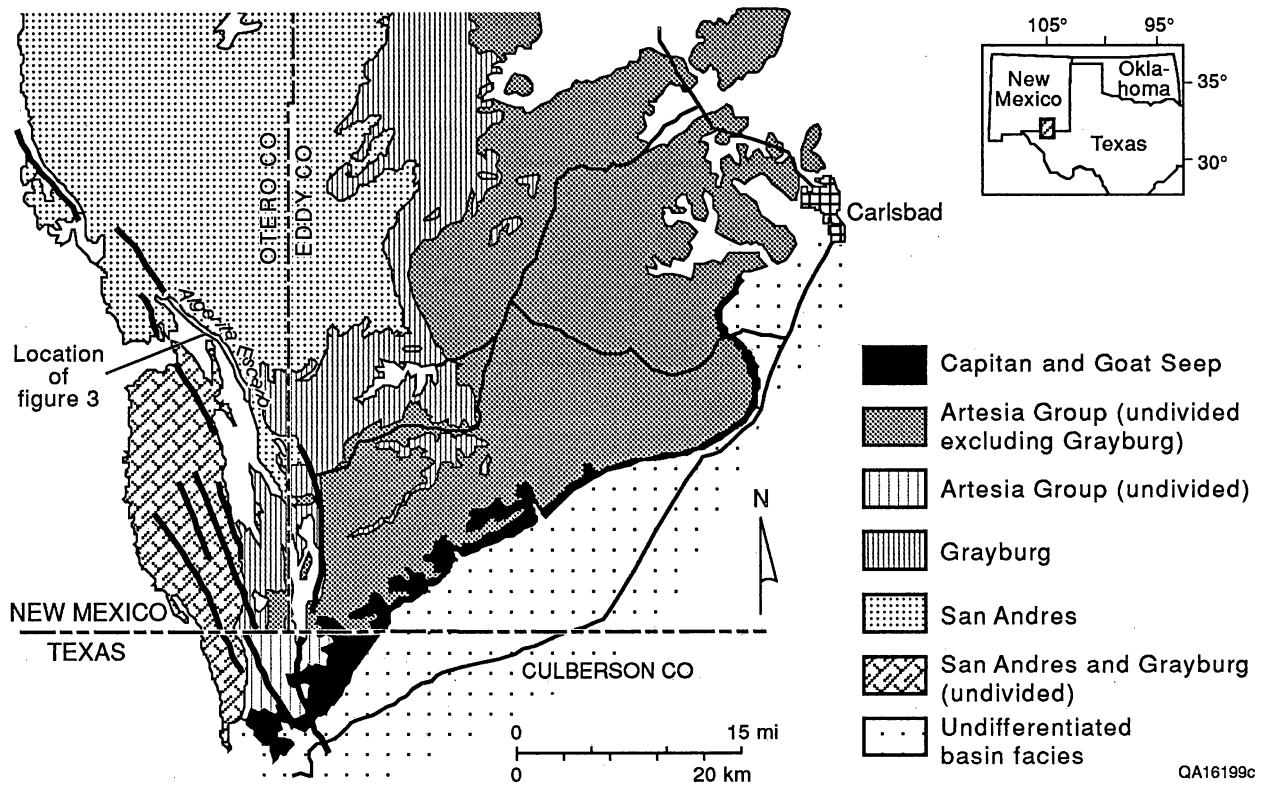
Figure 2. Geologic map of the Guadalupe Mountains complied from Hayes (1964) and King (1948) showing the Algerita Escarpment study area in the northern Guadalupe Mountains.
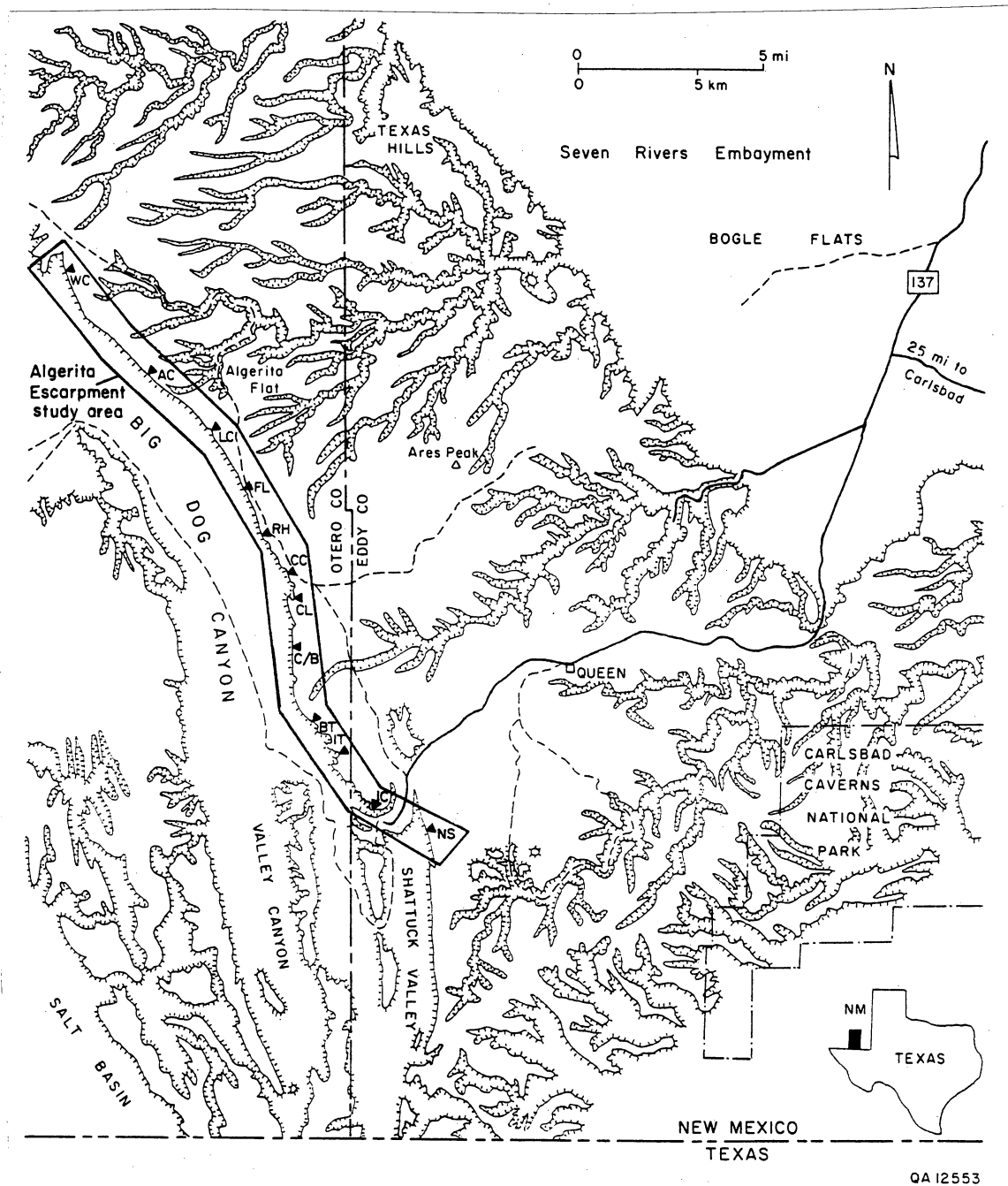
Figure 3. Physiographic map of the Algerita Escarpment area (modified from Moore and Wilde, 1986) showing locations of regional measured sections. Measured sections indicated are Woods Canyon (WC), Algerita Canyon (AC), Lawyer Canyon (LC), Fenceline (FL), Rawhide (RH), Cougar Canyon (CC), Coats Lake (CL), Coats/Brister Intermediate (C/B), Brister Tank (BT), Irabarne Tank (IT), Irabarne Canyon (IC), North Shattuck Valley (NS).

6
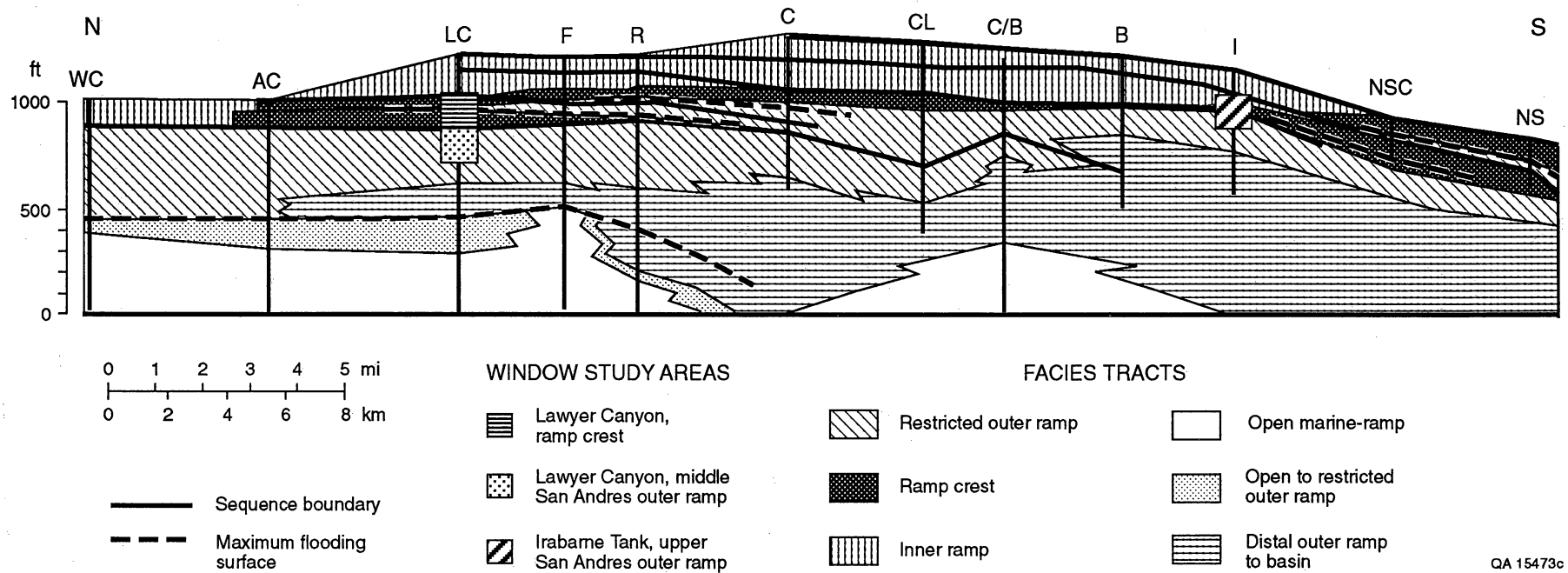
Figure 4. Sequence-stratigraphic model for the San Andres Formation of the Algerita Escarpment showing regional measured sections (see figure 3) and location of detailed parasequence windows. Measured sections indicated are Woods Canyon (WC), Algerita Canyon (AC), Lawyer Canyon (LC), Fenceline (FL), Rawhide (RH), Cougar Canyon (CC), Coats Lake (CL), Coats/Brister Intermediate (C/B), Brister Tank (BT), Irabarne Tank (IT), Irabarne Canyon (IC), North Shattuck Valley (NS).

conceptual model that can be tested and also lends a predictive capability to the data collected. In early studies of the San Andres in outcrop and in the subsurface, most workers (Hindrichs and others, 1986) thought this formation recorded a single upward-shallowing unit. A regional stratigraphic analysis by Sarg and Lehmann (1986) of the San Andres and associated units in the Guadalupe Mountain outcrop significantly revises this framework, introducing sequence-stratigraphic concepts into the analysis of the San Andres ramp complex.

Sarg and Lehmann (1986) divided the San Andres into two major third-order depositional sequences: (1) a lower sequence resting unconformably on the Leonardian Yeso Formation and comprising the lower and middle lithologic units of the San Andres and (2) an upper sequence approximately equivalent to the upper San Andres of Hayes (1964). Sarg and Lehmann (1986) suggested that these sequences, which were defined on the Algerita Escarpment on the basis of a subtle downward shift in onlap, could be correlated with the Last Chance Canyon area. In Last Chance Canyon, the sequences are separated by the Cherry Canyon tongue, which represents the lowstand systems tract (LST) of the upper San Andres sequence. Sarg and Lehmann also demonstrated that the upper San Andres sequence is unconformably overlain and onlapped by the Grayburg Formation (table 1).

Sequence Framework Developed by RCRL

Regional stratigraphic data collected along the Algerita Escarpment (fig. 3) have led to refinement of the Sarg and Lehmann (1986) sequence-stratigraphic framework, particularly in the upper San Andres sequence—the focus of the RCRL detailed studies (table 1). As a result of this focus, Sarg and Lehmann's upper San Andres third-order sequence is further subdivided into four fourth-order sequences, and a similar analysis in the lower to middle San Andres third-order sequence will probably also yield a further subdivision. The data for this sequence framework came from measured sections along the Algerita Escarpment in a dip-oriented cross section (figs. 3 and 4).

8

Table 1. Lithostratigraphic terminology of the San Andres Formation in the Algerita Escarpment/Last Chance Canyon area.

Boyd, 1959	Hayes, 1964	Sarg and Lehmann, 1986	This study
Grayburg	Grayburg	Grayburg	Grayburg
upper San Andres	upper San Andres	upper San Andres	u. San Andres 4 / Cherry Cnyn tongue / u. San Andres 3 / u. San Andres 2 / u. San Andres 1
	Cherry Canyon tongue	Cherry Canyon tongue	
lower San Andres	lower San Andres	middle San Andres	middle San Andres
		lower San Andres	lower San Andres
Yeso	Yeso	Yeso	Yeso

second San Andres 3rd-order sequence

first San Andres 3rd-order sequence

four 4th-order San Andres sequences

first San Andres 3rd-order seq.

QA 16369

Lower–Middle San Andres Third-Order Sequence (lmSA1)

The lower–middle San Andres sequence (lmSA1), as defined by Sarg and Lehmann (1986), and as used in this report, is 800 ft thick in Lawyer Canyon, where it is almost completely exposed (fig. 5). The lower boundary overlies Yeso tidal-flat deposits. At Lawyer Canyon, the sequence consists of an open-marine transgressive bank (lower San Andres Unit, 500 ft thick) succeeded by a prograding restricted-ramp system (middle San Andres) that includes a landward-tapering cherty mudstone tongue (<1 to 500 ft thick) that shallows upward into 280 ft of cyclic fusulinid-peloid wackestone/packstone (upper middle San Andres) (figs. 4 and 5). Middle San Andres facies on this portion of the Algerita Escarpment are entirely of outer-ramp origin (fig. 4).

The boundary between the lmSA1 sequence and the first upper San Andres sequence (uSA1) is apparently conformable as exposed on the Algerita Escarpment. It is represented by a downward shift in facies tracts that, in the Lawyer Canyon area, has placed ramp-crest ooid-peloid grainstones on top of outer ramp fusulinid packstone. This downward shift probably not only represents a minor 30- to 50-ft shift in lowering relative sea-level but also a significant lateral shift in facies tracts of several miles because of the gradual depositional slope.

The sequence consists of transgressive-systems-tract (TST) (lower San Andres) and high-stand-systems-tract (HST) (middle San Andres) units. The lowstand record for this sequence must be entirely basinally restricted and is not exposed in the Algerita Escarpment area. The TST is an open-marine ramp deposit (fig. 4) that represents one of the major marine-flooding events in the Permian Series of the Permian Basin. It places normal-marine strata and faunas atop the strongly prograded uppermost Leonardian platform and pushes the shelf edge a minimum of 20 mi landward. In the 17-mi dip transect of the Algerita Escarpment the TST forms a landward-thickening wedge from roughly 100 ft thick between the Rawhide section and the Cougar Canyon section to a maximum of 500 ft thick at the Fenceline section before leveling at 450 ft
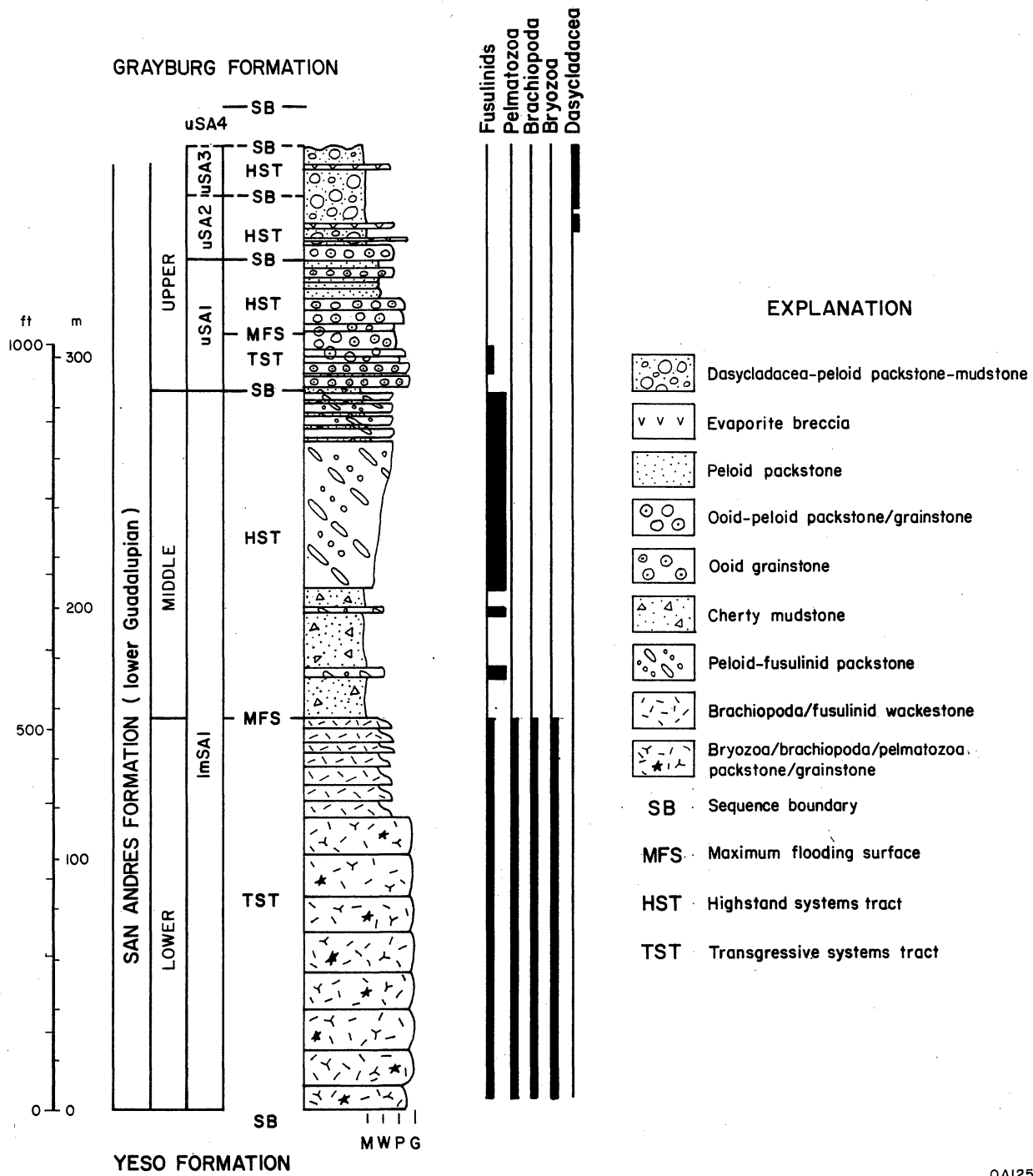
Figure 5. Measured section of the San Andres Formation at Lawyer Canyon displaying lithologic and sequence terminology.

from north of the Fenceline section to the Woods Canyon section (fig. 4). Mounding in the TST is observed downdip of this major bank (Coats Lake/Brister section, fig. 4) and may represent an oblique cut through a lobate TST bank margin or a discrete buildup similar to that forming the Seminole San Andres unit (see section on Regional Setting of the Seminole San Andres Unit).

Across most of the TST bank, sea-level rise began to outpace sediment accumulation in the upper third of the systems tract. This incipient drowning is recorded by an increase in fusulinids replacing corals and bryozoa in the upper 150 ft of the TST and the loss of high-energy cross-stratified skeletal grainstones upward. An exception occurs at the Fenceline section where thick crossbedded skeletal shoals record sedimentation within wave base for most TST deposition, resulting in local thickening of the section here (fig. 4). The thick crossbedded skeletal shoals at the Fenceline section and the thinner equivalents at the Lawyer Canyon and Algerita Canyon sections have excellent interparticle porosity and may be equivalent to Holt reservoir facies in the subsurface.

Downlap onto the TST generally cannot be readily detected using stratal geometry because the clinoform slopes of the lmSA1 HST are highly aggradational and define a low angle (<1°) relative to the TST. Distal outer-ramp clinoform toes of the HST that drape the TST are of dark cherty mudstone that has thin allodapic-fusulinid pelmatozoan-packstone beds. As the downlap surface on the maximum flooding surface is traced landward from Lawyer Canyon to Algerita Canyon, water depths at maximum flooding decrease and the cherty mudstone of the distal outer ramp facies ends. Eventually at Algerita Canyon, cyclic pelmatozoan and fusulinid wackestones of the open- to restricted-outer-ramp meld into fusulinid wackestones of the restricted outer ramp early HST without clear distinction (fig 4).

The HST of the lower–middle San Andres sequence is equivalent to the middle San Andres unit of Sarg and Lehmann (1986) and this report (fig. 5 and table 1). It consists of a lower section of dark-gray cherty spicule-bearing mudstone (<1 to 500 ft thick) and an upper section of massive to cyclic fusulinid-peloid wackestone/packstone (<1 to 400 ft thick). Cyclic sedimentation could not be discerned in the cherty mudstones, but shallow-water equivalents

of the mudstone facies farther landward (Woods Canyon section) display well-developed cyclicity from fusulinid wackestone to fusulinid-pelmatozoan wackestone/packstone. The fusulinid-peloid wackestone/packstone facies that composes the upper half of the HST at Lawyer Canyon is made up of poorly defined 20- to 30-ft-thick cherty fusulinid wackestone to fusulinid-pelmatozoan-peloid packstone parasequences at the base, which pass upward into well-defined 10- to 20-ft parasequences of mudstone to fusulinid wackestone to fusulinid-pelmatozoan-peloid packstone to grainstone in the upper 100 ft. Seaward of Lawyer Canyon, parasequences become increasingly mud-rich, and lower parasequences pass into cherty mudstone. However, nowhere on the Algerita Escarpment can it be demonstrated that the entire highstand passes into distal outer-ramp mudstones.

First Upper San Andres Fourth-Order Sequence (uSA1)

Subdivision of the upper San Andres third-order sequence of Sarg and Lehmann (1986) into four fourth-order sequences derives from detailed parasequence-scale mapping between Lawyer Canyon and north Sixshooter Canyon (table 1, fig. 4). The first upper San Andres sequence is best exposed at Lawyer Canyon where it is made up of nine parasequences totaling 140 to 180 ft. Because a more detailed discussion of facies at Lawyer Canyon follows, only the major sequence-defining characteristics are outlined here.

The first upper San Andres fourth-order sequence boundary (uSA1-SB) appears conformable with the lmSA1 sequence in the study area as described previously. Ooid-peloid packstone/grainstone dominates the facies composition of uSA1 parasequences at Lawyer Canyon, suggesting a ramp-crest position for this sequence. An ideal parasequence in the ramp-crest area would be basal flooded shelf mudstone followed by shallow-water shelf peloid-wackestone/packstone, bar-flank ooid-peloid packstone/grainstone, and bar-crest peloid-ooid grainstone in an upward-shallowing succession. Parasequences 1 through 6 of uSA1 are aggradational to slightly backstepping, with successively higher parasequences containing less

shallow-water high-energy facies. Parasequence 7 of the first upper San Andres sequence (ps7/uSA1) is a 35-ft-thick unit representing maximum flooding within uSA1. Indicators of maximum flooding during ps7 are its anomalous thickness (suggesting greater accommodation space), the thick basal flooded shelf mudstone, and fusulinid-peloid packstone near the base of the unit marking the updip maximum transgression of outer ramp facies in the upper San Andres. The maximum flooding surface for the uSA1 sequence is thus placed inside ps7 within the fusulinid packstone tongue.

The remaining upward-shallowing portion of ps7 and ps8 through 9b represent the highstand part of this sequence (60 to 90 ft thick). The upper sequence boundary of uSA1 is a karst surface containing pockets of solution-collapse breccia and 1 to 2 ft deep solution dolines. This karsted bar-top surface displays a minimum of 35 ft of depositional relief that was subaerially exposed and onlapped by uSA2 parasequences. At least 20 ft of this onlap is visible in the detailed study area of the Lawyer Canyon uSA1 parasequence window (see section on Lawyer Canyon uSA1 Ramp-Crest Window).

Updip from Lawyer Canyon the uSA1 sequence passes into peloid packstones and wackestones of a lower-energy lagoonal facies tract. Downdip of Lawyer Canyon the mudstone to grainstone upward-shoaling parasequences are replaced by mudstone/fusulinid wackestone to fusulinid wackestone/packstone parasequences of the outer ramp. Differentiation of the uSA1 and uSA2 sequences becomes difficult downdip of Lawyer Canyon because the sequence boundary passes into a paraconformable contact between outer ramp parasequences of uSA1 and uSA2 (fig. 4).

Second Upper San Andres Fourth-Order Sequence (uSA2)

The uSA2 sequence is recognized across the length of the Algerita study area and is best exposed in its ramp-crest position in the Rawhide to Cougar Canyon area. Here it is 120 ft thick and consists of nine to ten fusulinid-peloid packstone parasequences and five peloid grainstone

parasequences. The uSA1/uSA2 sequence boundary is a microkarst surface recognizable from Lawyer Canyon to halfway between the Lawyer Canyon and Fenceline sections. In the Fenceline section a basal set of grainstone-dominated parasequences onlap the basal uSA1/uSA2 sequence boundary in the direction of Lawyer Canyon and pass downdip in the Cougar Canyon area into fusulinid-peloid packstone parasequences. These basal parasequences represent the TST of uSA2.

Above the TST grainstone parasequences at the Fenceline section and northward are dasyclad-peloid mudstone/wackestone/packstone parasequences deposited in an inner ramp lagoon behind an extensive grainstone complex in the Cougar Canyon-Irabarne Tank area. The grainstone complex contains at least four stacked grainstone parasequences that are either mudstone-based or amalgamated grainstone on grainstone. In the latter case parasequences are separated by microkarst surfaces. The dip width of the ramp-crest facies tract of the uSA2 HST is estimated to be 5 mi.

The uSA2/uSA3 sequence boundary is the most traceable karst surface on the Algerita Escarpment. The karst profile is best developed in the Cougar Canyon area where as much as 20 ft of collapse breccia containing minor quartz silt is preserved. Elsewhere the surface is represented by a more subtle, scalloped erosion surface having 0.5 to 2 ft of relief atop the thick (20 to 40 ft) grainstone complex.

Third Upper San Andres Fourth-Order Sequence (uSA3)

The uSA3 sequence is bounded below by the regionally mappable karst surface described in uSA2 and is capped by a ledge-forming amalgamated tidal-flat complex that is readily mapped on air photos and in the field from Coats Lake to Irabarne Tank. Updip of Coats Lake this tidal-flat complex changes facies to lagoonal mudstone, but the surface corresponds closely to the onset of siliciclastic sedimentation (Lovington sandstones and associated thin siltstone beds) and is thus carried at the base of these sandstones from Coats Lake north. The uSA3 thickens

markedly on the Algerita Escarpment from 20 ft in the Fenceline area to 115 ft at the Irabarne Tank 10 mi downdip (fig. 5). Approximately 5 transgressive parasequences and 10 highstand parasequences are recognized in the Irabarne area, with transgressive parasequences containing fusulinid wackestone/packstone marking significant flooding over the previously subaerially exposed uSA2 sequence boundary. Highstand parasequences are dominated by peloid packstone/grainstone and dasycladacean-peloid packstone of largely inner-ramp origin. Ramp-crest grainstones of the highstand tract are restricted to downdip of Irabarne Tank in the North Sixshooter and North Shattuck sections and define a 4-mi-wide belt.

Fourth Upper San Andres Fourth-Order Sequence (uSA4)

Sequence uSA4 is bounded below by the regionally mappable tidal-flat complex (Coats Lake to Irabarne Tank sections) and the Lovington sandstones (Cougar Canyon to Lawyer Canyon sections) and above by a variably developed karst surface that separates the San Andres and Grayburg Formations. This upper sequence boundary is exposed on the Algerita Escarpment from Cougar Canyon in the north to North Shattuck in the south (fig. 5) and is correlative to the karst event separating the San Andres and Grayburg Formations in the subsurface, such as the one found at Yates and Taylor Link fields in the southern Central Basin Platform (Craig, 1988).

The uSA4 sequence is 115 ft thick in the area between the Brister and Irabarne Tank sections, where it is best exposed. A thin transgressive system tract includes two fusulinid-peloid-packstone-bearing parasequences immediately above the uSA3 sequence boundary. The siliciclastic-sand-based parasequences (Lovington Sandstones and two to four other locally occurring sands) are also interpreted as transgressive units, with sand being preserved on the shelf rather than bypassed because of overall high accommodation during TST deposition. Highstand deposits in the Fenceline to Irabarne Tank sections include some 10 to 12 thin (5 to 15 ft thick) mudstone to dasycladacean-peloid wackestone/packstone parasequences that have

locally developed tidal-flat caps. In the North Sixshooter and North Shattuck sections, massive amalgamated ramp-crest peloid-ooid grainstone parasequences make up much of the HST, with thin mudstone-based, fenestral/tepee-capped parasequences forming the final four to five parasequences. The ramp-crest facies tract of the HST in uSA4 is at least 3.5 mi in dip dimension.

PARASEQUENCE WINDOW STUDY AREAS FOR INTERWELL MODELING

The priority of the outcrop part of the RCRL program was to develop deterministic images of geologic facies architecture and corresponding porosity-permeability structure at a scale ranging from 1 ft to tens of feet vertically and inches to hundreds of feet laterally (interwell scale). Several areas along the Algerita Escarpment were selected for detailed study on the interwell scale and are referred to in this report as *window study areas*. The three windows are located on figure 4. The images are useful for constraining both qualitative and quantitative interpretations of equivalent reservoir strata. The sequence analysis was conducted to provide a framework within which the detailed data could be collected and more meaningfully applied to the San Andres in other parts of the Permian Basin, and to similar carbonate-ramp systems worldwide.

The ramp-crest grainstone complex of the uSA1 sequence located at Lawyer Canyon was selected as the first detailed parasequence window study area. This area was given high priority because a series of recent reservoir-characterization studies of San Andres and Grayburg reservoirs (Longacre, 1980; Harris and others, 1984; Bebout and others, 1987; Ruppel and Cander, 1988) demonstrated that this facies tract displayed the greatest inherent geologic heterogeneity and hence could benefit most from facies-variability data provided by continuous outcrops. Other areas selected for detailed study, areas currently being analyzed geologically and petrophysically, are the Lawyer Canyon lmSA1 and the Irabarne Tank uSA2 outer-ramp windows (fig. 4).

Parasequence Framework for Reservoir-Scale Mapping

Parasequences are the most significant stratigraphic elements in the San Andres Formation at the reservoir scale both in outcrop and in reservoirs. A parasequence is defined as "relatively conformable succession of genetically related beds or bedsets bounded by marine flooding surfaces and their correlative surfaces" (Van Wagoner and others, 1988, their p. 39). These units are defined in a one-dimensional sense by the classic upward-shallowing cycles of Wilson (1975) and James (1977) that produce an ideal upward-coarsening profile of mudstone to wackestone/packstone to grainstone (with or without tidal-flat cap). However, the parasequence is a three-dimensional, time-bounded entity that is only partly described by the one-dimensional upward-shallowing profile. The two-dimensional parasequence windows described herein are a way of capturing the lateral variability within parasequences.

The parasequence concept has direct applications for reservoir characterization and flow-modeling studies in carbonate reservoir strata. First, the flooding surfaces and, locally, the tidal-flat caps that bound parasequences often commonly define low-permeability layers (mudstones, wackestones, and sulfate-cemented tidal-flat facies) that serve to vertically stratify the reservoir. Second, the systematic upward and lateral change in rock fabrics within a parasequence provides a fundamental basis for converting the parasequence framework into petrophysical parameters. Third, dividing the reservoir interval into smaller time-bounded units promotes accurate depositional and diagenetic facies measurement which can form the basis of stochastic reservoir models.

Petrophysical Rock-Fabric Approach for Quantification of Geologic Framework

The goal of reservoir description is to describe the spatial distribution of petrophysical parameters such as porosity, permeability, and saturation. Engineering measurements from wireline logs, core analysis, production history, pressure analysis, and tracer tests provide quantitative measurements of the petrophysical parameters in the vicinity of the wellbore.

This wellbore data must be integrated with the geologic framework to describe the three-dimensional distribution of petrophysical properties. Rock-fabric studies that relate rock texture to pore-size distribution, and thus to petrophysical properties, are the key elements necessary to convert the geologic framework into engineering measurements for input into computer simulators. This approach has been used in the study of the San Andres outcrop and Seminole San Andres Unit reservoir.

Classification of Carbonate Porosity By Rock-Fabric Method

Pore space in carbonate rocks can be divided into interparticle and vuggy pores on the basis of the particular nature of the carbonate rocks (Lucia, 1983). The pore-size distribution of interparticle porosity is controlled by particle size, sorting, and volume of interparticle porosity. Two classes of particle size and sorting are recognized: (1) mud-dominated, where the interparticle space is filled with lime mud and (2) grain-dominated, where the interparticle space is partially filled or free of lime mud (fig. 6). To relate this to Dunham's (1962) classification, the packstone category must be split into grain- and mud-dominated packstones.

Dolomitization may increase the particle size and thus the interparticle pore sizes. Mud-dominated fabrics with dolomite crystal sizes larger than 20 μm are grouped into two classes: medium crystal size (20 to 100 μm) and large crystal size (>100 μm) (fig. 7). Dolomite crystal size has little effect on the pore size of grainstone fabrics. However, the pore size of grain-dominated packstones will increase when replaced by dolomite crystals >100 μm in diameter.

Three petrophysical classes are recognized (fig. 7). The most favorable petrophysical characteristics are in a class composed of grainstones, dolograinstones with any size of dolomite crystals, and mud-dominated dolomites with large crystal sizes (>100 μm). The least favorable petrophysical characteristics are in a class composed of mud-dominated limestones and dolomites with fine crystal sizes (<20 μm). A class with intermediate petrophysical
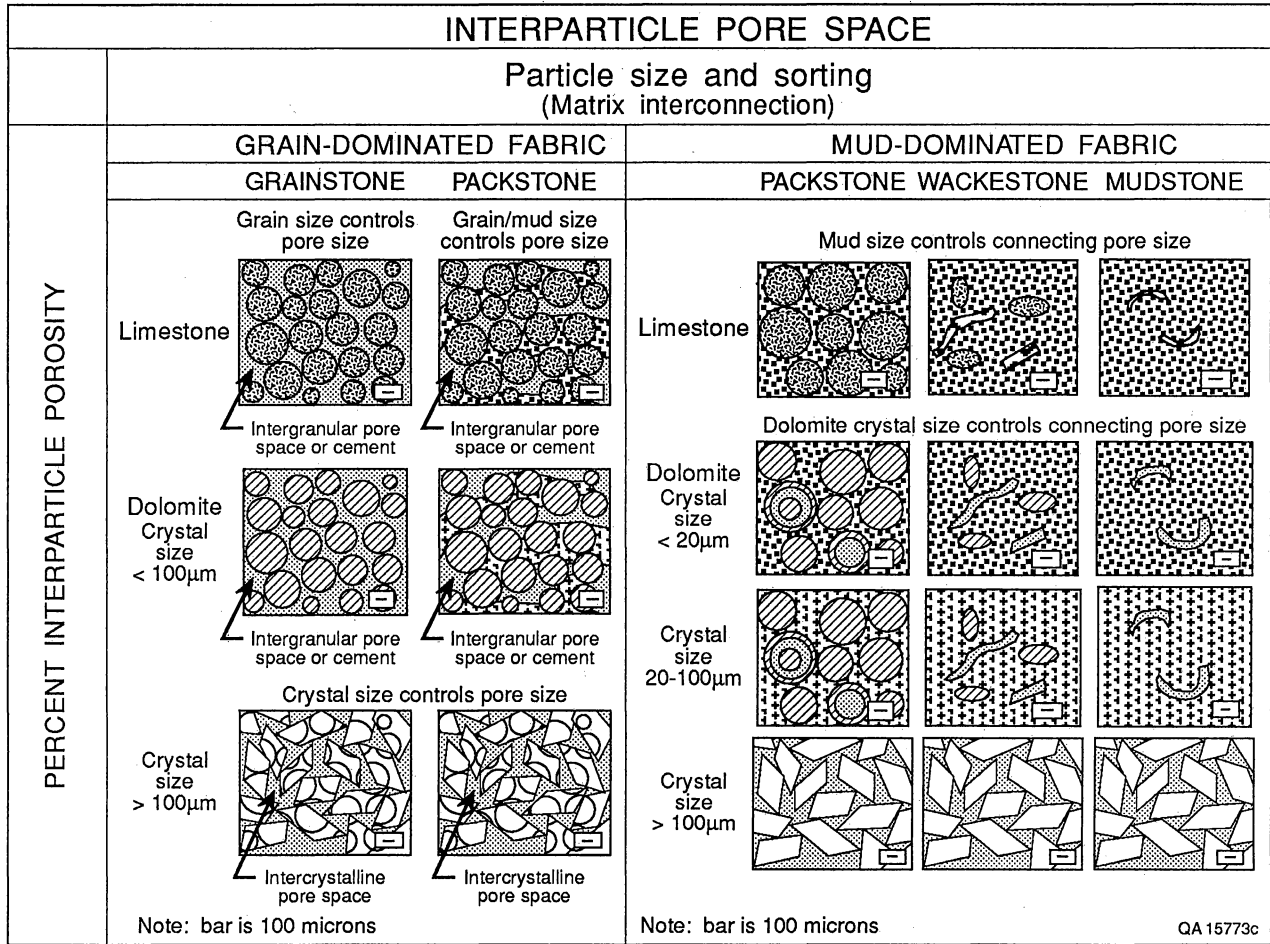
Figure 6. Classification of interparticle pore space.

PETROPHYSICAL CLASSES

GRAIN-DOMINATED FABRIC

GRAINSTONE   PACKSTONE

MUD-DOMINATED FABRIC

PACKSTONE WACKESTONE MUDSTONE

Note: bar is 100 microns

Class 3

Class 2

Class 1

Limestone

Dolomite
Crystal size
< 20µm

Limestone

Crystal
size
20-100µm

Dolomite
Crystal
size
< 100µm

Crystal
size
> 100µm

Crystal
size
> 100µm

QA 15772c
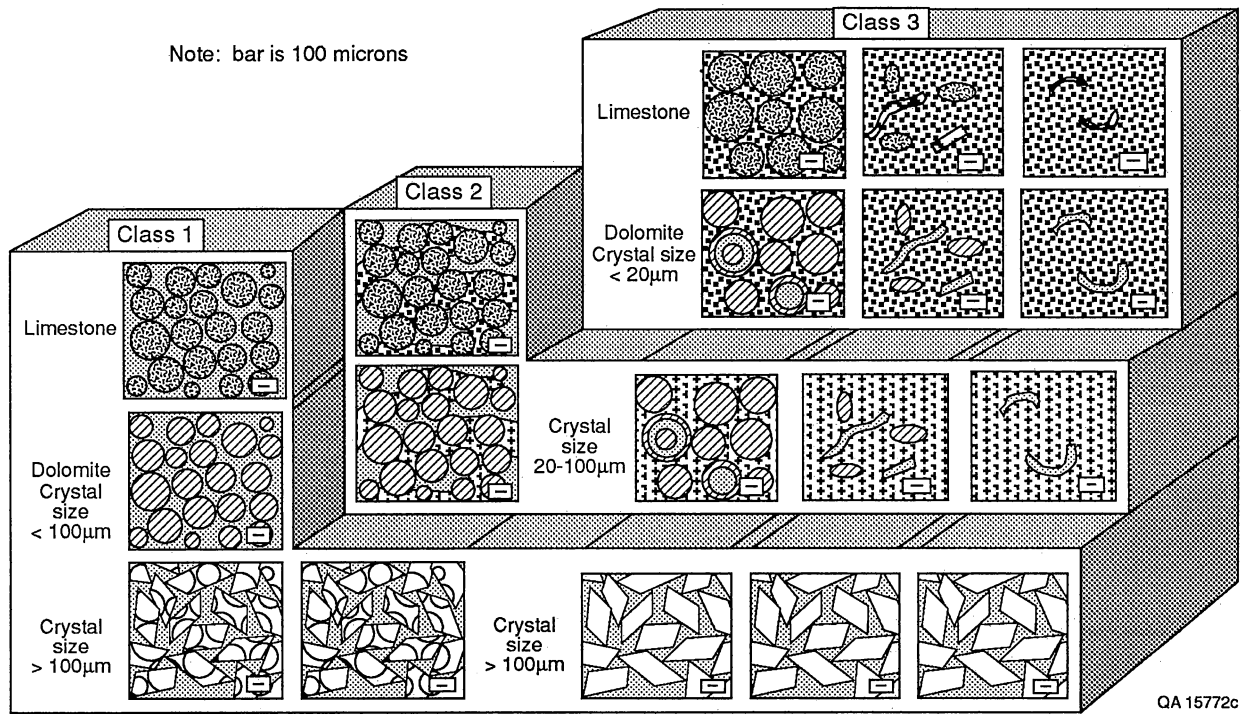
Figure 7. Petrophysical rock-fabric classes.

characteristics is composed of grain-dominated packstones, both limestones and dolomites with crystal sizes <100 µm, and medium crystal mud-dominated dolomites.

The three petrophysical classes can be expressed in permeability as shown in figure 8. Generic porosity-permeability transforms for the three classes are given below in the following equations:

Grainstones and
dolograinstones

$$k = (66.07 \times 10^8)(\phi_p^{8.65}) \tag{1}$$

Grain-dominated packstones,
fine to medium dolograin-
dominated packstones,
and medium crystalline
mud-dominated dolomite
fabrics

$$k = (2.04 \times 10^6)(\phi_p^{6.38}) \tag{2}$$

Mud-dominated and fine
crystalline dolomud-
dominated fabrics.

$$k = (1.047 \times 10^4)(\phi_p^{4.82}) \tag{3}$$

The three petrophysical classes can also be expressed in saturation as shown in figure 9. The relationships between particle size and sorting, interparticle porosity, and water saturation were derived using mercury capillary pressure curves from samples of the same petrophysical class. The equations expressing the relationships are given in the following equations:

Grainstones and
dolograinstones

$$S_w = .02219 \times H^{-0.316} \times \phi^{-1.745} \tag{4}$$

Grain-dominated packstones,
fine to medium dolograin-
dominated packstones,
and medium crystalline
mud-dominated dolomite
fabrics

$$S_w = 0.1403 \times H^{-0.407} \times \phi^{-1.440} \tag{5}$$

Mud-dominated and fine
crystal dolomud-
dominated fabrics

$$S_w = 0.6110 \times H^{-0.505} \times \phi^{-1.210} \tag{6}$$

where H is the height above the free water level in feet and ϕ is the fractional porosity.

Vuggy pore spaces are divided into separate vugs and touching vugs on the basis of the types of interconnections (fig. 10). Separate vugs are connected only through interparticle
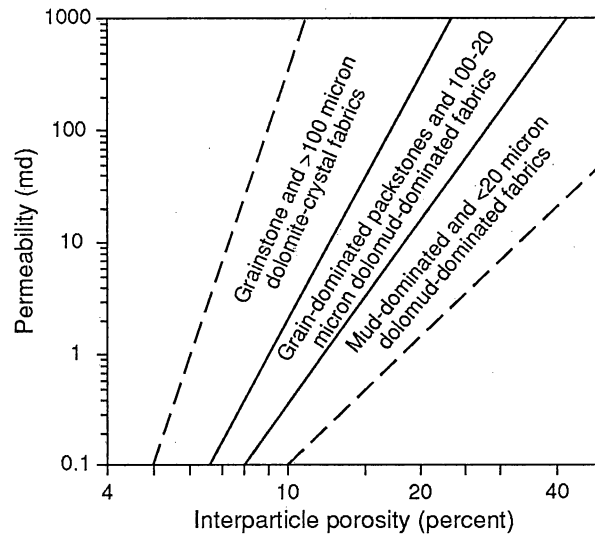
Figure 8. Porosity-permeability relationships of various rock-fabric fields in nonvuggy carbonate rocks.
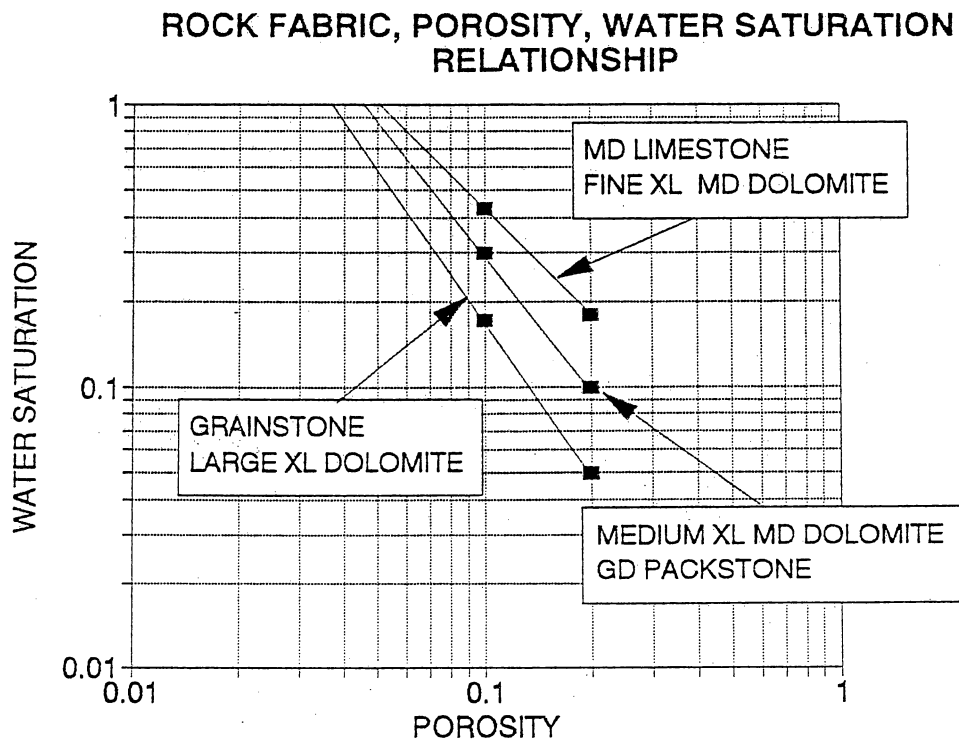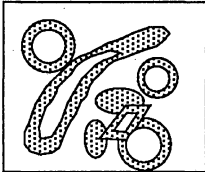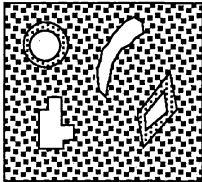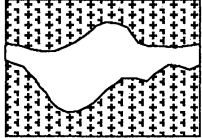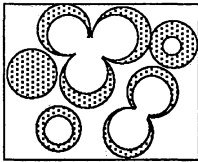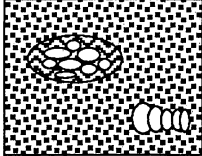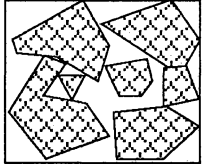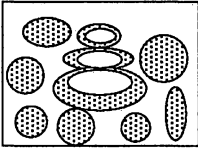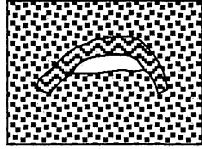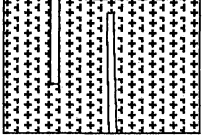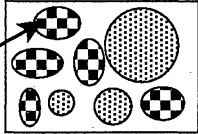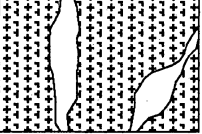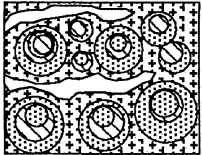
Figure 9. Rock-fabric, porosity, and water saturation relationships from capillary pressure curves.

23

VUGGY PORE SPACE		
SEPARATE-VUG PORES (VUG-TO-MATRIX-TO-VUG CONNECTION)		TOUCHING-VUG PORES (VUG-TO-VUG CONNECTION)
GRAIN-DOMINATED FABRIC	MUD-DOMINATED FABRIC	GRAIN- AND MUD-DOMINATED FABRICS
EXAMPLE TYPES	EXAMPLE TYPES	EXAMPLE TYPES
Moldic pores	Moldic pores	Cavernous
Composite moldic pores	Intrafossil pores	Breccia
Intrafossil pores	Shelter pores	Fractures
Intragranular microporosity		Solution enlarged fractures
		Fenestral

PERCENT SEPARATE-VUG POROSITY

QA 15762c

Figure 10. Classification of vuggy pore space.

24

pore space. Moldic pores, composite moldic pores, intrafossil pores, microporosity in grainstones, and shelter pores in mud-dominated carbonates are types of separate-vug pores. Touching vugs form a connecting pore network on the interwell scale. Cavernous, fracture, and breccia porosities are examples.

Separate-vug pore space reduces permeability from what would be expected if the porosity were all interparticle. Permeability is higher than expected from interparticle porosity in the presence of a touching-vug pore system. With the exception of intraparticle microporosity, vuggy pore space is large enough to be considered filled with hydrocarbon. Intraparticle microporosity is often filled with capillary-trapped water.

Lawyer Canyon uSA1 Ramp-Crest Window

Geologic Framework

The Lawyer Canyon uSA1 ramp-crest parasequence window contains a grid of 50- to 300-ft laterally spaced measured sections, each covering 120 to 180 ft of vertical section. The lateral dimension of this geologic grid is 2,600 ft, covering an area equivalent to several well spacings in a typical San Andres or Grayburg reservoir (figs. 11 and 12).

This window contains nine parasequences, each displaying variable development of the ideal upward-shallowing, -coarsening rock-fabric succession (figs. 13 and 14). Parasequences average 15 ft in thickness and are continuous on the scale of the 2,600-ft cross section, but component rock-fabric facies are not. Grainstone facies range from 5 to 38 ft in maximum thickness (average of 16 ft) and from <100 to >2,600 ft in dip length (fig. 13). Wackestone/packstone facies are thinner and more continuous than the grainstone part of the parasequences. Mudstones range from <1 to 5 ft in thickness and from tens of feet to several mi in width (beyond the scope of the detailed study area) in dip dimension.

By examining a single parasequence for internal architecture (figs. 15 and 16) sedimentation can be seen to have been initiated by mudstone deposition interpreted to

EXPLANATION

● Algerita boreholes
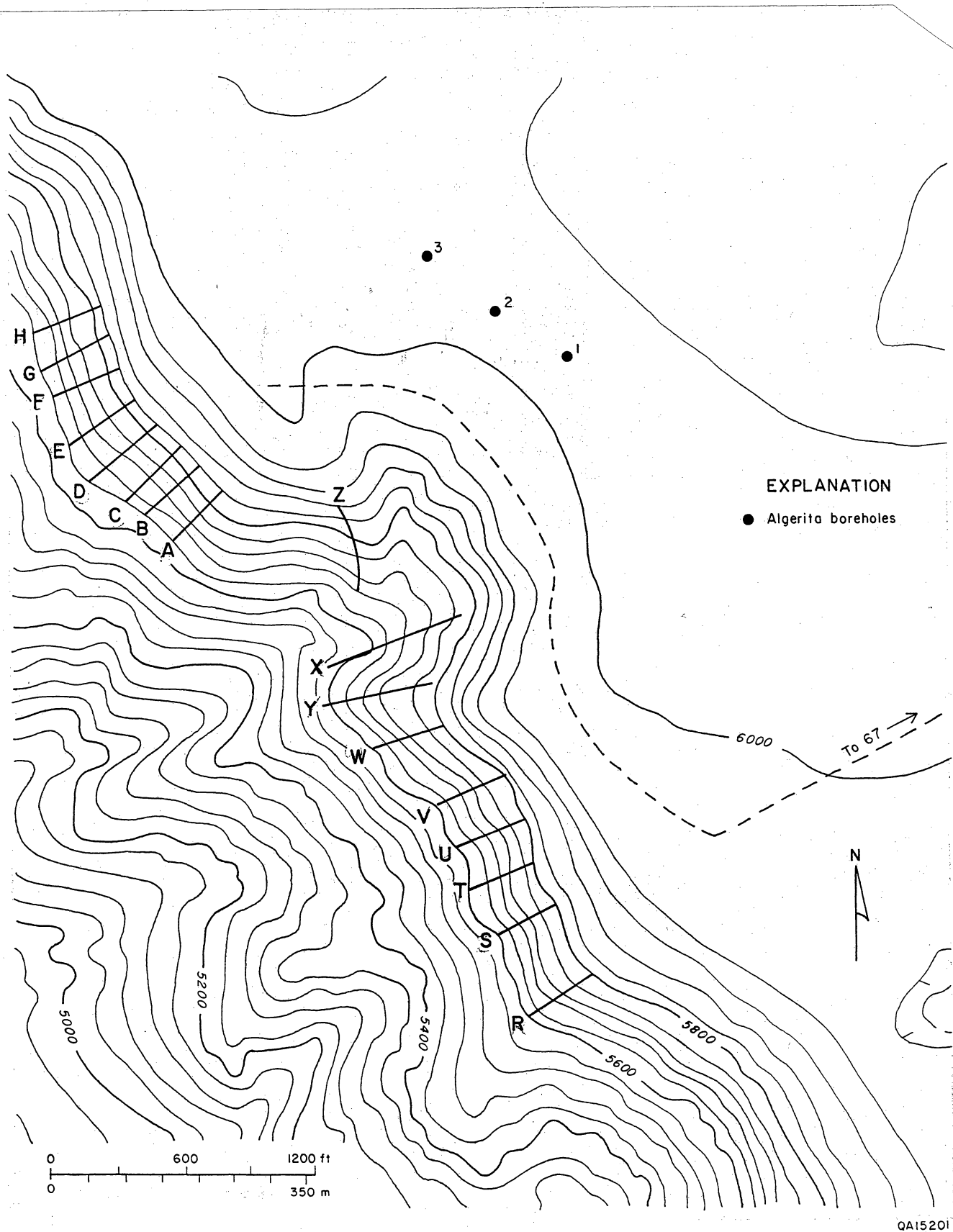
Figure 11. Topographic map of the Lawyer Canyon area showing location of detailed measured sections and three boreholes. Contour interval is 200 ft.

26
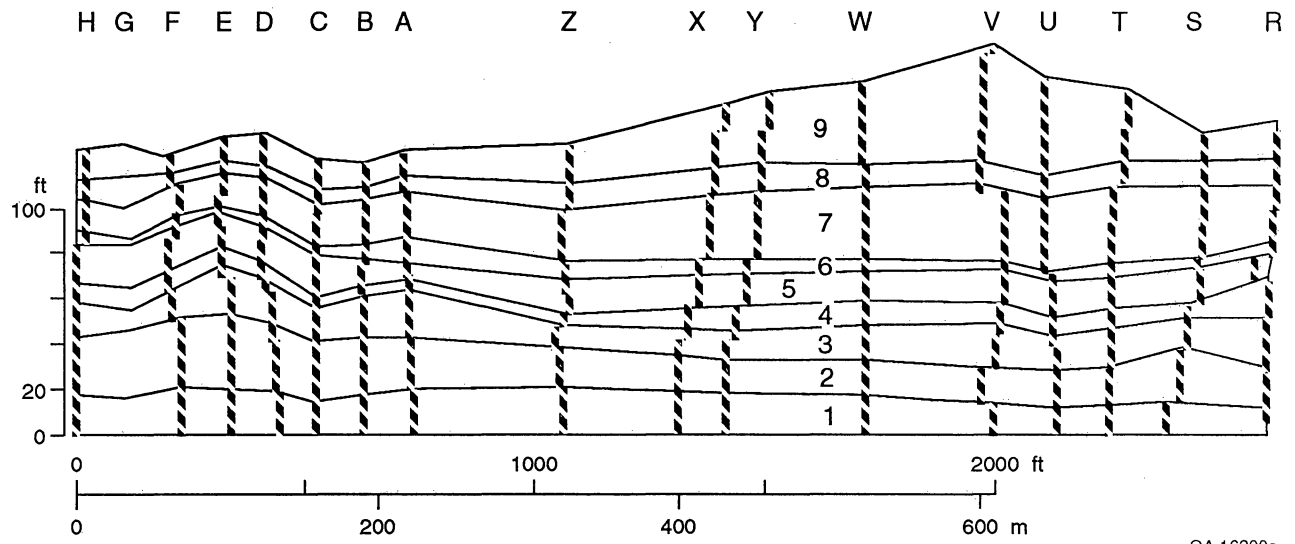
Figure 12. Cross section showing distribution of geologic measured sections in the Lawyer Canyon uSA1 ramp-crest parasequence window and parasequence outlines.
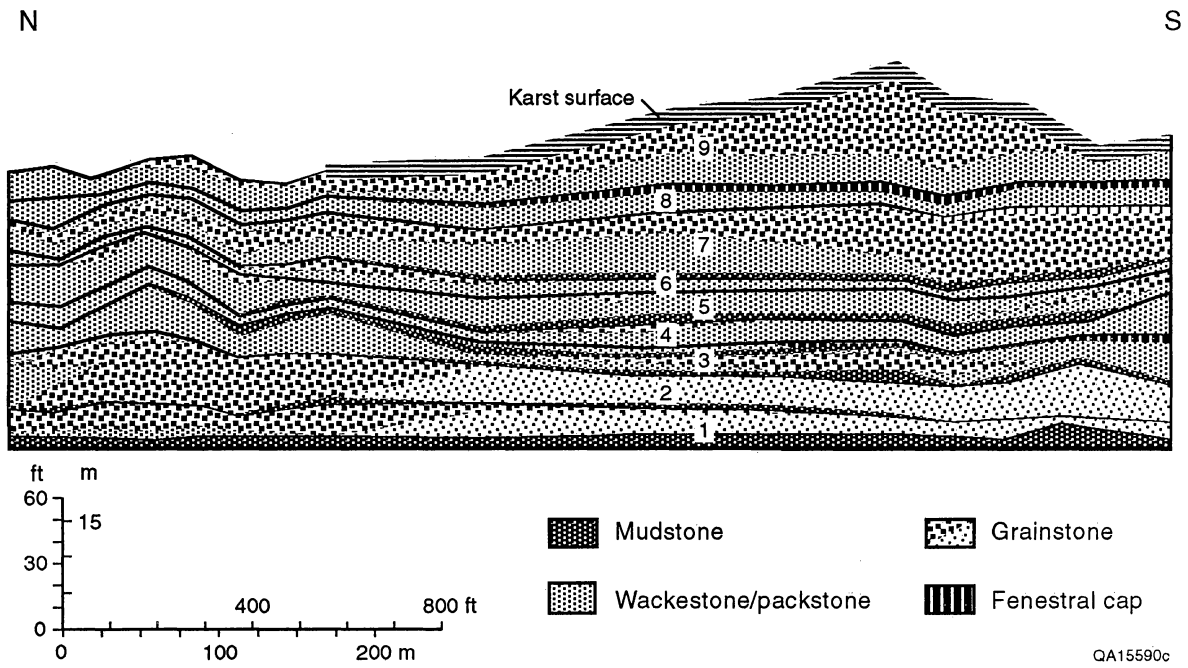
Figure 13. Simplified depositional facies version of the Lawyer Canyon uSA1 ramp-crest parasequence window.
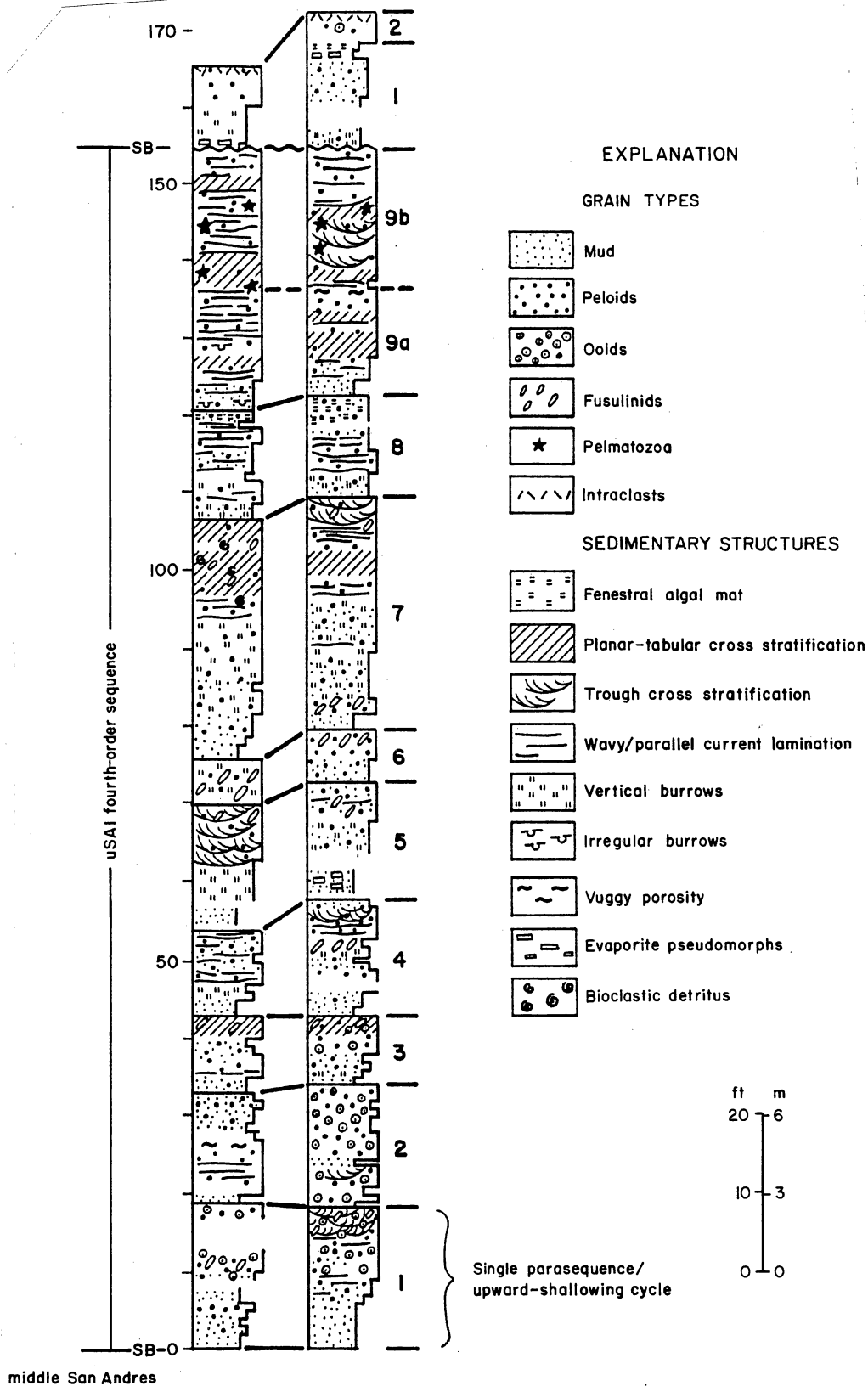
Figure 14. Detailed vertical sections showing the depositional cyclicity of the ramp-crest parasequences, Lawyer Canyon uSA1 ramp-crest parasequence window.

29

Figure 15. Lateral facies variations within parasequence 1 (ps1), Lawyer Canyon uSA1 ramp-crest parasequence window. The basal flooded-shelf mudstone is continuous for the 2,500 ft extent of the cross section but the bar-crest facies passes basinward into bar-flank facies and finally wedges out into wackestones and mudstones.
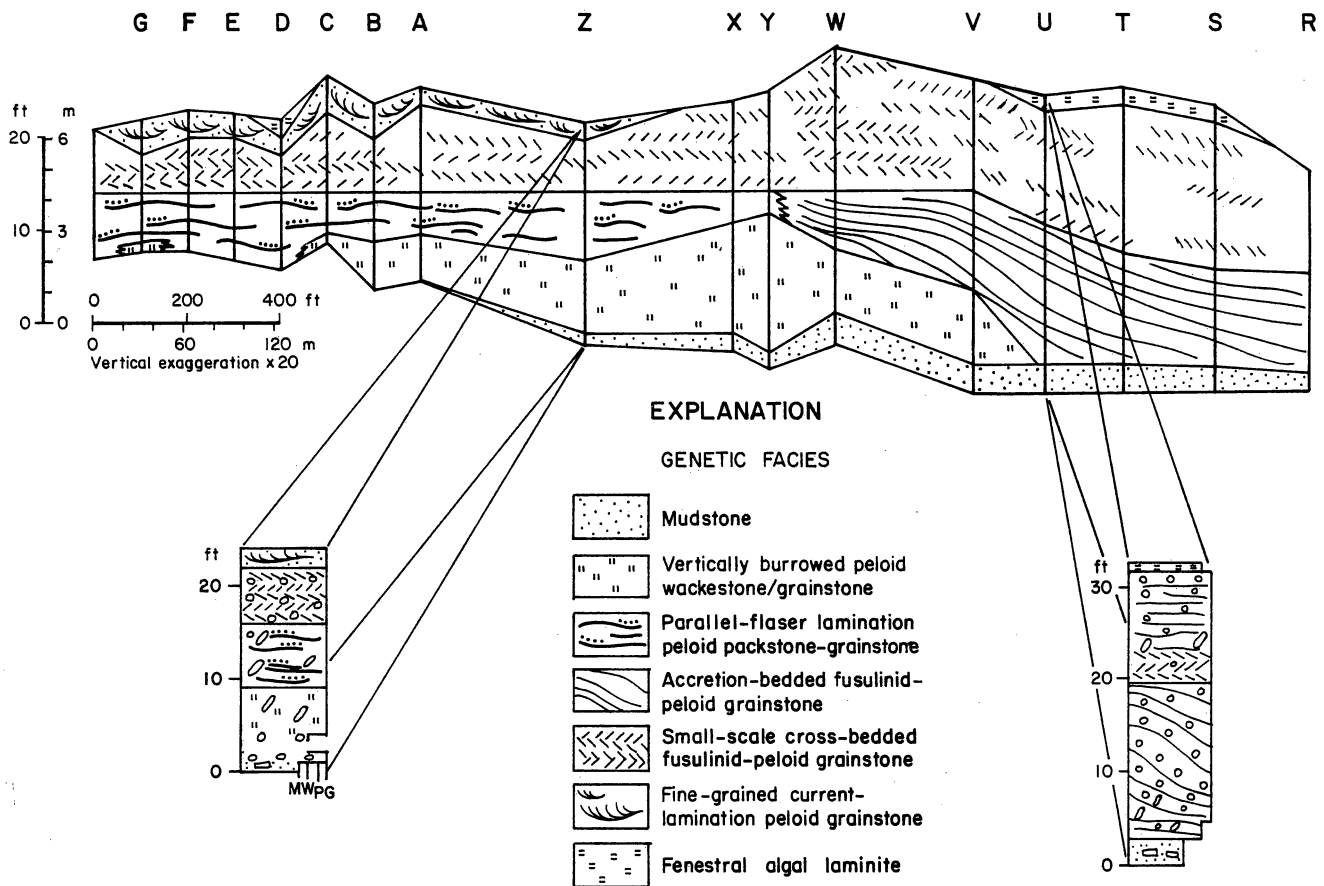
Figure 16. Lateral facies variations within parasequence 7 (ps7), Lawyer Canyon uSA1 ramp-crest parasequence window showing development of channel-filling(?) accretion stratification in addition to small-scale cross-stratified bar-crest deposits and a thin, locally developed tidal flat atop the bar-crest grainstones.

31

represent slow sedimentation after a rapid sea-level rise (flooded-shelf mudstone facies). After this transgressive event, the carbonate system established itself and built to sea level, first by deposition of open-shelf, vertically burrowed to flaser-lenticular-bedded wackestones and packstones, and finally by deposition of bar-crest and -flank grainstones and packstones were established. Bar-crest grainstones exhibit abundant small-scale trough and planar-tabular cross-stratification, indicating active reworking within the zone of normal wave base and tidal influence. Bar-flank deposits contain parallel-laminated grainstones intercalated with thin wackestone/packstone layers that represent storm-dominated shelf sedimentation. Such sedimentation transports grainstones from the active bar-crest to the bar-flank, where they are intercalated with lower energy shelf sediments.

Facies development within a parasequence is potentially highly variable. Note that in ps9 (fig. 13), grainstones reach a thickness of 38 ft but quickly thin laterally. In ps3, a 1,000-ft-wide grainstone unit is flanked by wackestones and packstones while in ps2 the grainstone is continuous across the cross section (2,600 ft). Generally, in the ramp-crest facies tract, the thicker the parasequence the more laterally variable the resultant facies mosaic, largely because the greater accommodation space allows a fuller range of depositional environments to develop.

Application of Petrophysical Rock-Fabric Approach to Lawyer Canyon Outcrop

Outcrop effects

One of the major concerns at the outset of the study was the comparison of outcrop and subsurface petrophysical data, although Hinricks and others (1987) showed that the porosity and permeability values compared well with values from the Wasson San Andres field. Features recognized in the outcrop that affect petrophysical properties and that can be directly related to uplift and exposure of the San Andres outcrop are fracturing, cave development, travertine precipitation, and dissolution of gypsum and anhydrite to form vugs and breccias. Every effort

was made to avoid these features when taking samples for petrophysical analysis. Microscopic examination of thin sections, however, shows that some samples contain a gravity oriented fibrous calcite cement similar to travertine, which is believed to be a product of uplift and subaereal exposure. These samples were discarded from the data set.

Calcium sulfate is a major component of San Andres reservoir rocks but is not present in the outcrop study area. The past presence of anhydrite is indicated by anhydrite inclusions in diagenetic quartz crystals and by sparry calcite blebs that have straight sides and rectangular reentrants suggesting they are pseudomorphic after poikilotopic anhydrite crystals.

Sparry calcite was present in many samples and is believed to be a by-product of sulfate dissolution. Although the outline of most of the sparry calcite found in outcrop San Andres samples does not indicate a sulfate precursor, this occurrence of calcite is often interpreted to originate from the replacement of anhydrite. Calcite replacement of anhydrite in the Tansill Formation of the Guadalupe Mountains has been suggested by Lucia (1961) and Back and others (1983) conclude that calcite in the Mississippian of the Black Hills area, South Dakota and Wyoming, is related to dissolution of gypsum and dolomite.

Although as much as 40 percent sparry calcite is present in one sample, there is no relationship between calcite volume and porosity (fig. 17). This observation is similar to the relationship between poikilotopic anhydrite and porosity in San Andres reservoirs. Therefore, although the sparry calcite may not have replaced sulfate on a one-to-one basis, it affects the petrophysical properties of the samples in a manner comparable to that caused by anhydrite in San Andres reservoirs.

Rock fabrics

Rock samples from the upper San Andres outcrop at Lawyer Canyon are composed of dolomite, sparry calcite, and minor amounts of replacement quartz and authigenic clay. The

PARASEQUENCE 1 - LAWYER CANYON
CALCITE VS TOTAL POROSITY
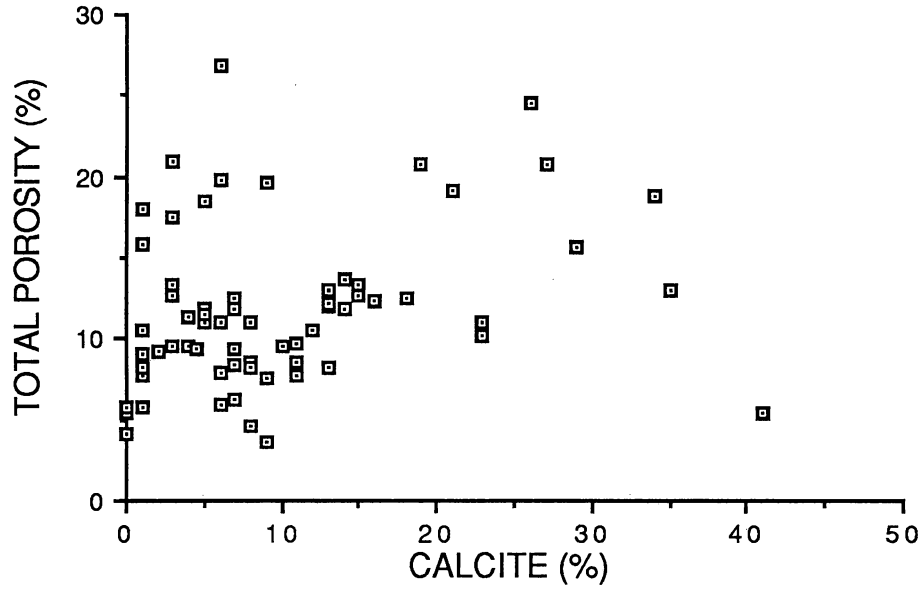
Figure 17. Cross-plot of porosity versus percent calcite in samples from parasequence 1 showing no relationship between these two fabric elements. This is similar to the relationship between porosity and percent calcite shown in figure 71.

crystal size of the dolomite averages about 15 µm, except for the grainstones in the upper part of ps9, where the dolomite crystal size averages about 100 µm.

Rock fabrics recognized in the Lawyer Canyon Window are grainstones, moldic grainstones, grain-dominated packstones, mud-dominated packstones, wackestones, mudstones, and fenestral. All three nonvuggy petrophysical/rock fabric classes are present, and average porosity and geometric-mean permeability values of these classes are given in table 2 based on core plugs. Two classes of moldic grainstones have been defined; highly moldic grainstones with >10 percent moldic porosity and moldic grainstones with between 5 and 10 percent moldic porosity.

The data in table 2 show that the average porosity of the nonvuggy productive fabrics does not vary significantly, but the average permeability varies by an order of magnitude between each rock-fabric class. The porosity in the vuggy grainstone fabrics is high, but the permeability is lower than would be expected for a nonvuggy grainstone. The dolomite crystal size is typically about 15 µm, but the dolomite crystal size in the grainstone fabric varies from 15 to >100 µm. Despite this variation in crystal size, figure 18 shows that all grainstones group in class 1, indicating that the dolomite crystal size is of little importance in describing the flow characteristics of grainstones. The porosity-permeability transform for the grainstone fabrics is given below.

$$k = (22.90 \times 10^{-8}) (\phi_p{}^{8.33}) \tag{7}$$

Types of separate-vug porosity observed are moldic, intrafossil, and intraparticle microporosity. Grainstones in ps1 contain small amounts of intraparticle microporosity, but the microporosity does not increase the permeability (fig. 19). Parasequence 7 contains as much as 30 percent moldic porosity. In the highly moldic fabrics (moldic porosity greater than 10 percent) the porosity averages 22 percent and the permeability varies from 0.5 to 20 md with decreasing amounts of moldic porosity (fig. 20). The moldic grainstone of ps7 has an average

Table 2. Average porosity and geometric-mean permeability of petrophysical rock-fabric classes based on core plug data.

Petrophysical classes	Porosity (%)	Permeability (geometric average, md)
Nonvuggy		
Dolograinstones	11.7	10.7
Fine dolograin-dominated packstones	12.9	1.9
Fine crystalline dolomud-dominated fabrics	10.5	0.3
Vuggy		
Highly moldic grainstones	23.0	2.5
Moldic grainstones	15.9	2.2
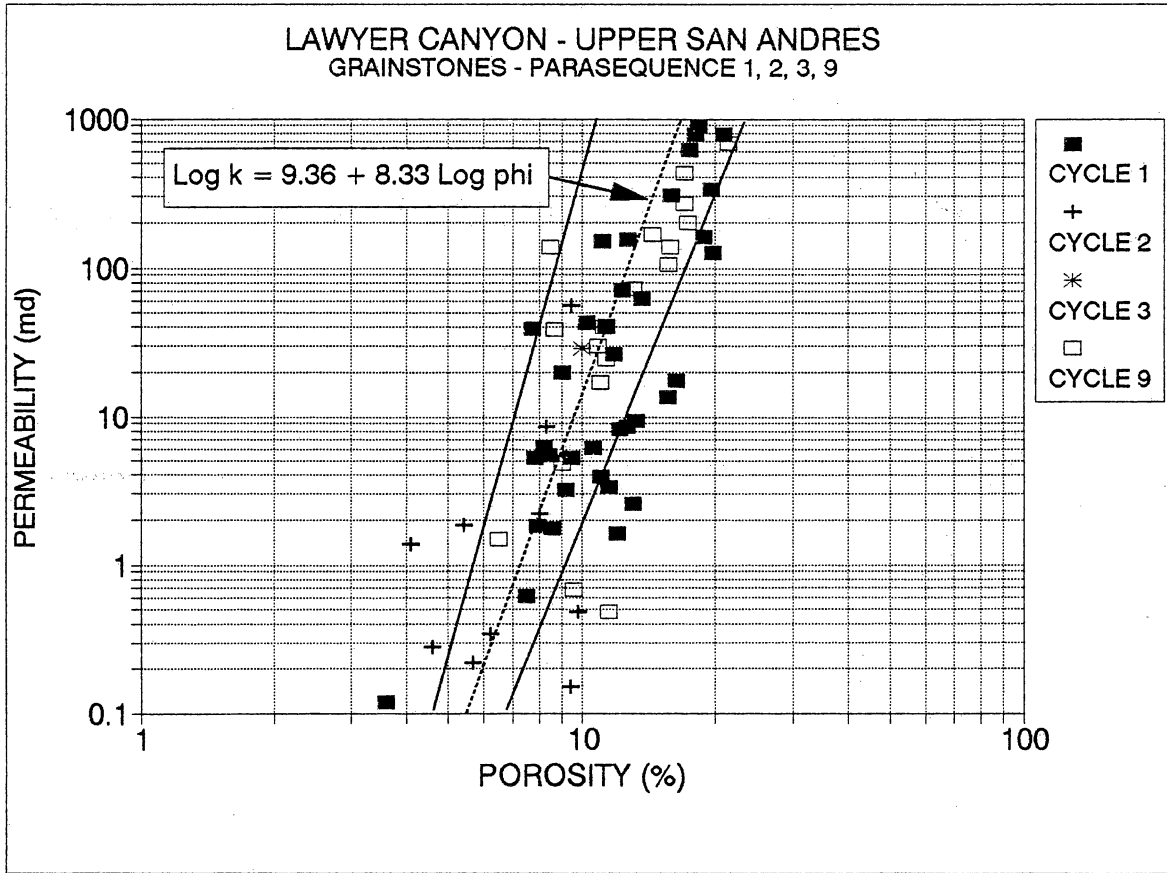
Figure 18. Porosity-permeability cross plot for grainstones of parasequences 1, 2, 3, and 9 (ps1, 2, 3, and 9) compared with class 1, grainstone petrophysical/rock-fabric field.
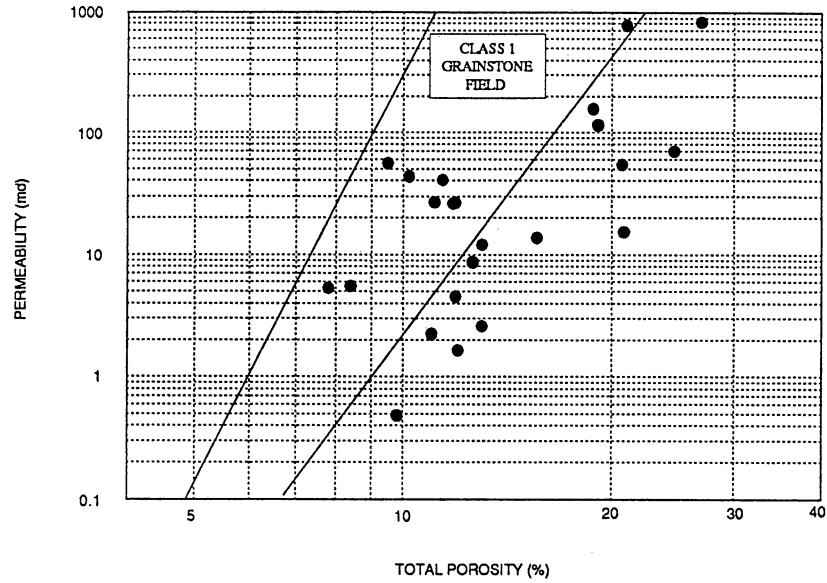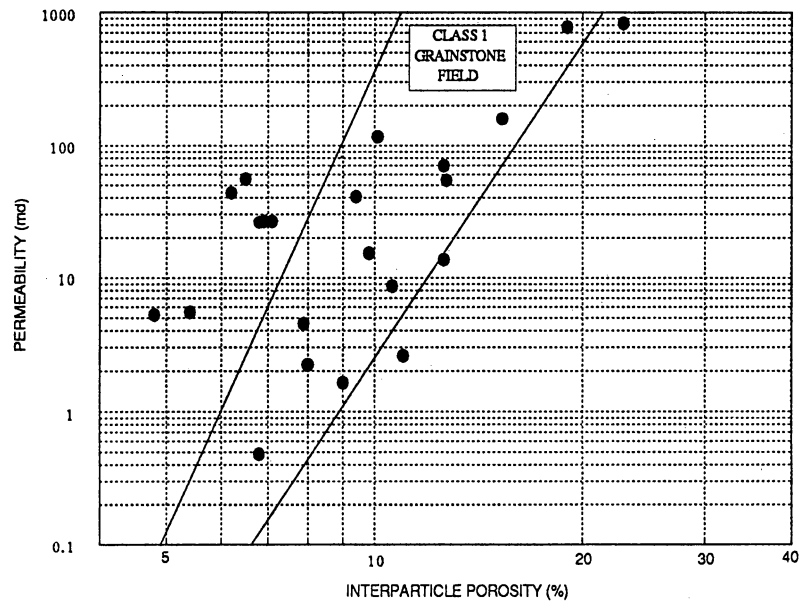
Figure 19. Effect of intragranular microporosity on permeability. (a) Total porosity versus permeability cross plot for parasequence 1 (ps1) grainstones showing that most of the data plots right of the grainstone field. Total porosity includes intragranular microporosity and intergranular porosity. (b) Same as (a) except that intragranular microporosity has been subtracted from total porosity showing that when interparticle porosity is plotted against permeability most of the data falls in the grainstone field.

LAWYER CANYON - UPPER SAN ANDRES
HIGHLY MOLDIC GRAINSTONE - PARASEQ. 7
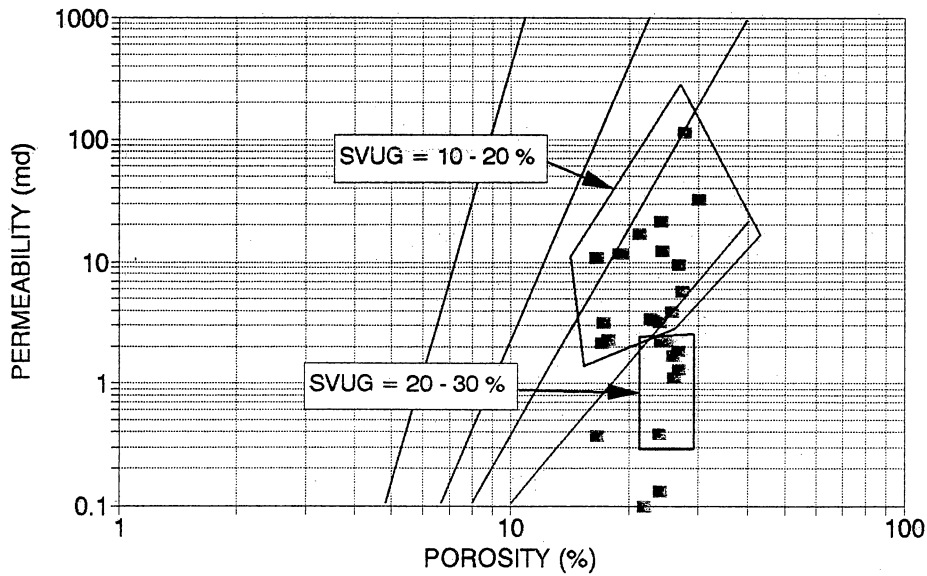
Figure 20. Porosity-permeability cross plot for the highly moldic grainstone facies of parasequence 7 (ps7) illustrating that permeability is function of separate-vug porosity, not total porosity. The three petrophysical fields are presented to illustrate that the data points fall well to the right of the grainstone field.

LAWYER CANYON - UPPER SAN ANDRES
MOLDIC GRAINSTONE - PARASEQUENCE 7
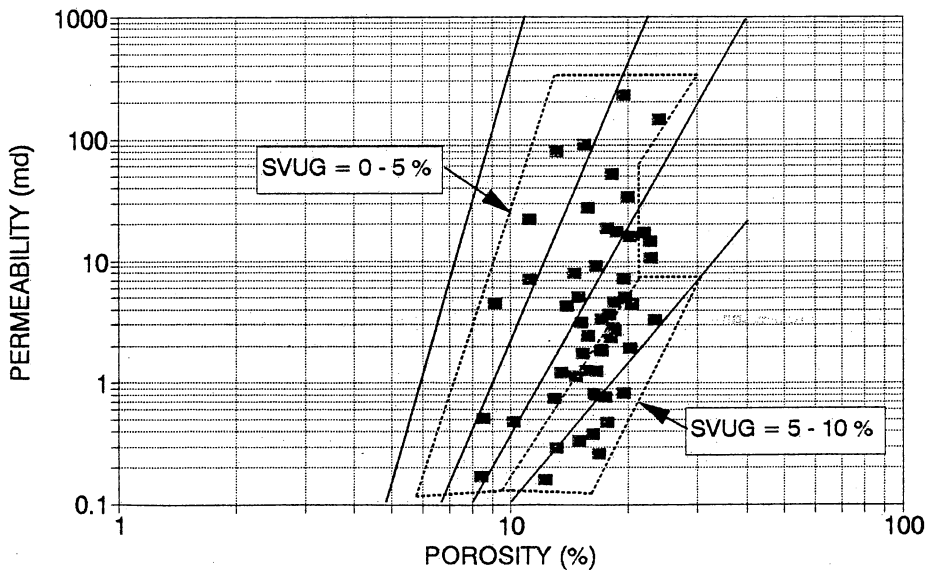
Figure 21. Porosity-permeability cross plot of the moldic grainstone facies of parasequence 7 (ps7) illustrating that permeability is a function of separate-vug porosity. Note that as separate-vug porosity approaches zero the data plots closer to the grainstone petrophysical rock-fabric field.

porosity of 15 percent, and again, the permeability increases as the separate-vug porosity decreases (fig. 21).

Statistical analysis of permeability by facies and textures

A statistical analysis was made using outcrop description of facies and textures and outcrop permeability measurements. The histogram of permeabilities using core (fig. 22) shows a roughly lognormal distribution. Mechanical field permeameter (MFP) measurements show a truncated distribution because of the 1-md detection limit of the MFP data.

Textures are based on outcrop descriptions and do not include a distinction between grain- and mud-dominated packstones. However, even when using the simplified field classification, the textures exhibit significant differences in mean permeability (fig. 23), with mudstone having the lowest permeability and grainstone having the highest permeability. Most of the facies are also characterized by significantly different mean permeabilities (fig. 24). Generally, shelf facies exhibit significantly lower mean permeabilities than bar facies, with the bar-crest and bar-accretion-set facies having the highest mean permeability of log k = 1.1 md. The facies characteristic (fig. 24) is consistent with the rock-fabric characteristic (fig. 23) because the bar facies consist mostly of high-permeability grainstones and the shelf facies consist mostly of low-permeability, mud-dominated packstones and wackestones, and the flooded shelf facies is mudstone.

Stacking of Rock Fabrics within a Parasequence

The tie between depositional facies and rock fabric (texture) is of paramount importance to quantification of the geologic framework. Here we have an excellent tie so that rock fabrics can be used to quantify the facies patterns in terms of porosity, permeability, and saturation.

Parasequence 1 shows a typical vertical and lateral stacking of rock-fabric facies for an upward-shoaling parasequence (fig. 25). The vertical sequence is from tight, mud-dominated

40
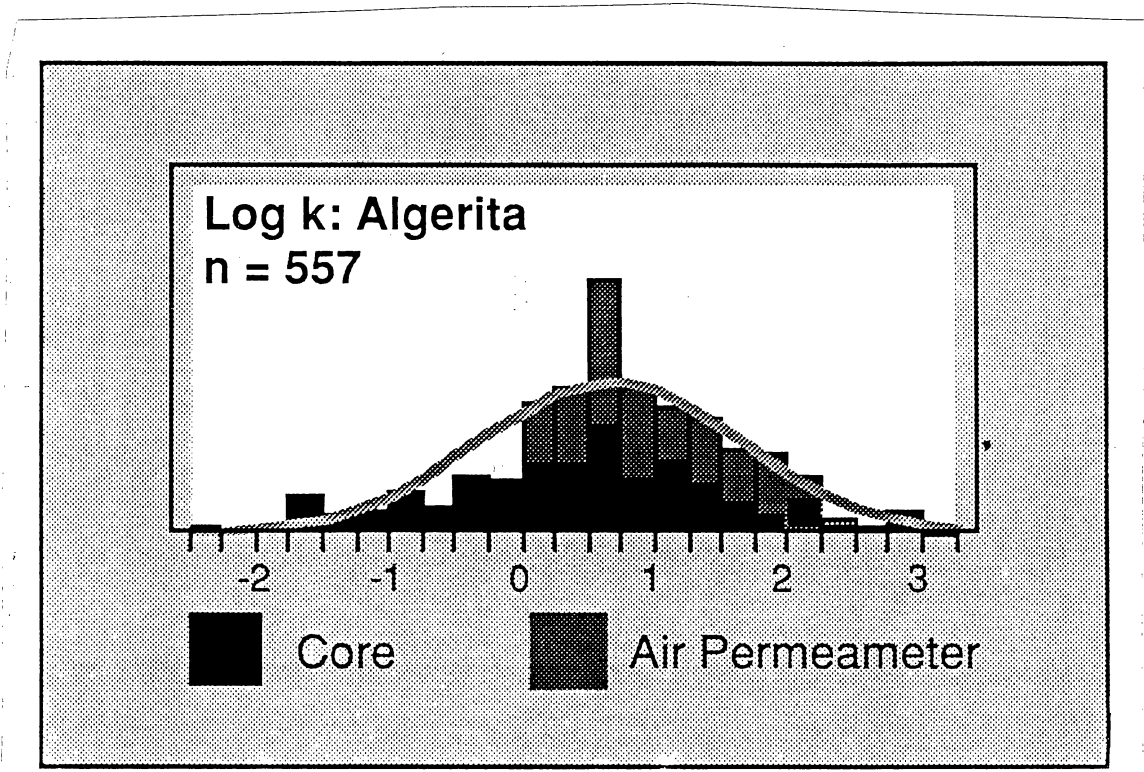
Figure 22. Histogram of permeabilities obtained along the geologically measured sections.

TEXTURE: Comparison of mean k's

Log k axis: 3, 2, 1, 0, -1, -2

Mudstone, Wackestone, Packstone, Grainstone

EXPLANATION

Mean — 95% Confidence interval for the mean

Width of diamond is proportional to number of data points.

Comparison circles

When ∠ > 90°, means **not** significantly different

When ∠ < 90°, means **are** significantly different
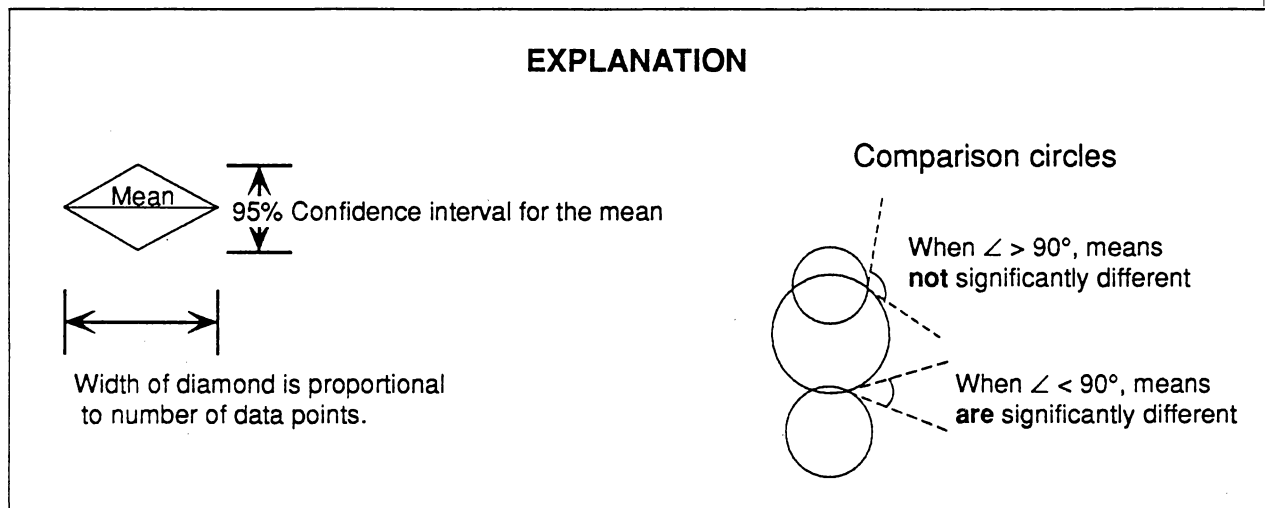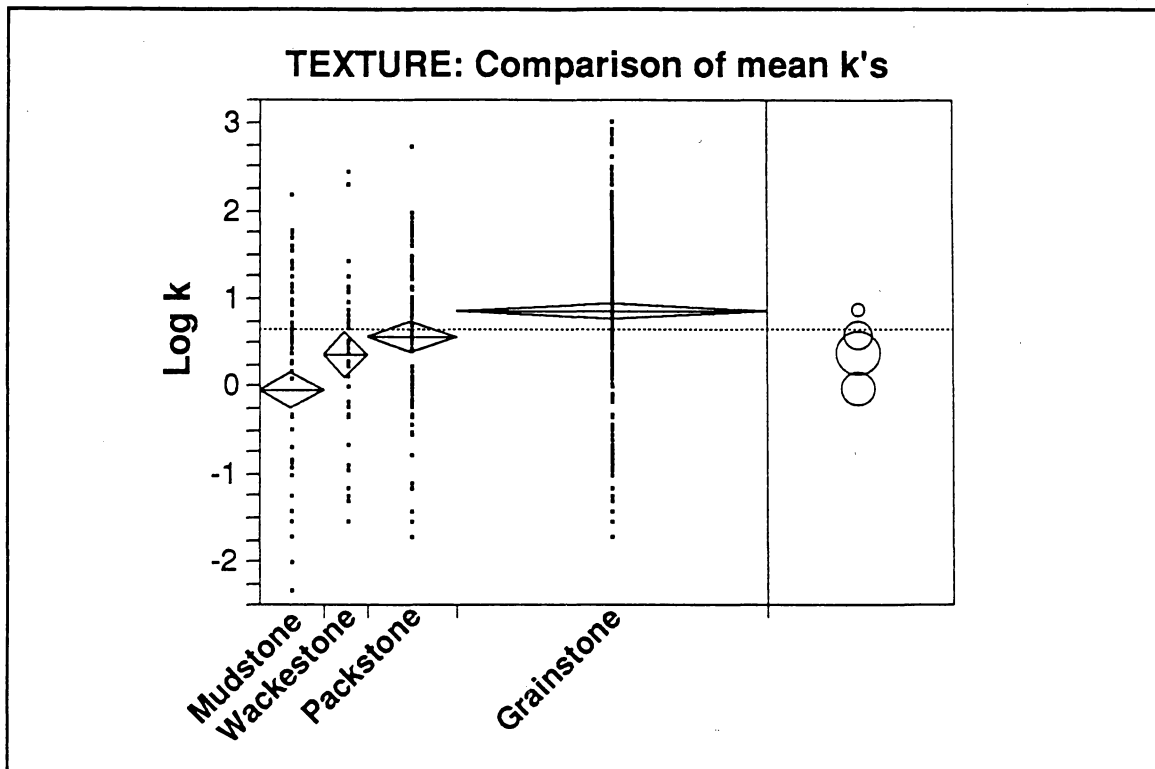
Figure 23. Statistical comparison of means of permeability for different textures. Comparison circles correspond to the 95 percent confidence intervals for the means.

42

Facies: Comparison of Means
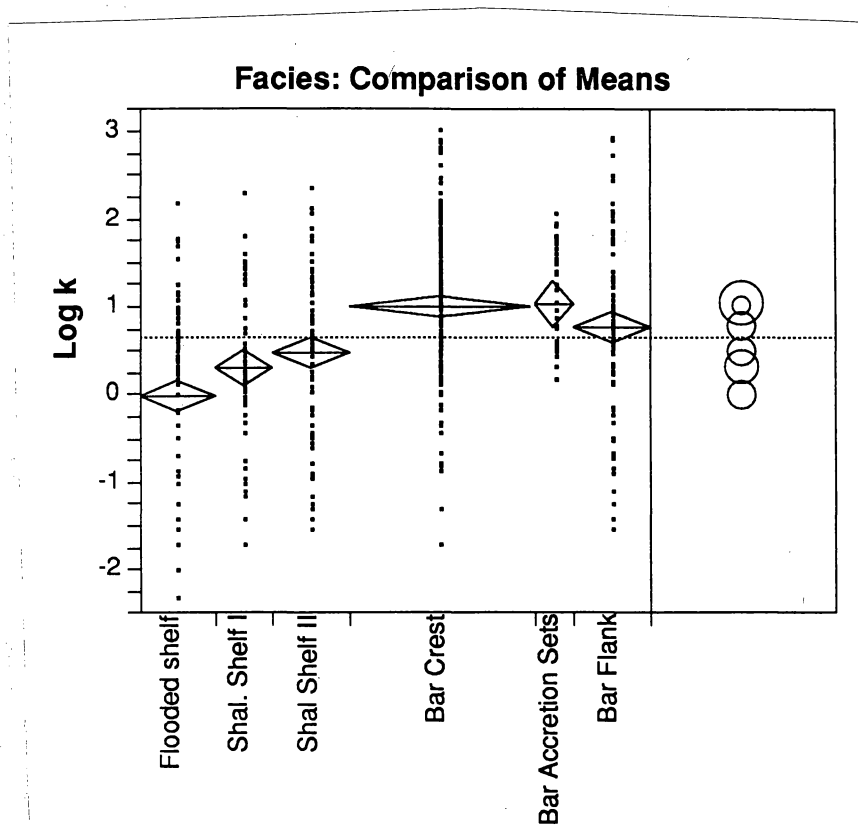
Mean Estimates

Facies	N	Mean	Std Error
Flooded shelf	82	-0.01	0.10
Shallow shelf I	48	0.25	0.13
Shallow shelf II	73	0.51	0.11
Bar crest	158	1.07	0.07
Bar top	6	0.10	0.37
Tidal flat	2	0.37	0.65
Bar accretion sets	18	1.11	0.22
Bar flank	82	0.76	0.10
Shallow shelf I (moldic)	16	0.45	0.23
Shallow shelf II (moldic)	9	0.26	0.30
Bar crest (moldic)	39	0.73	0.15
Bar accretion sets (moldic)	24	0.98	0.19

Figure 24. Statistical comparison of means of permeability for different facies. Standard error values refer to the estimated means.
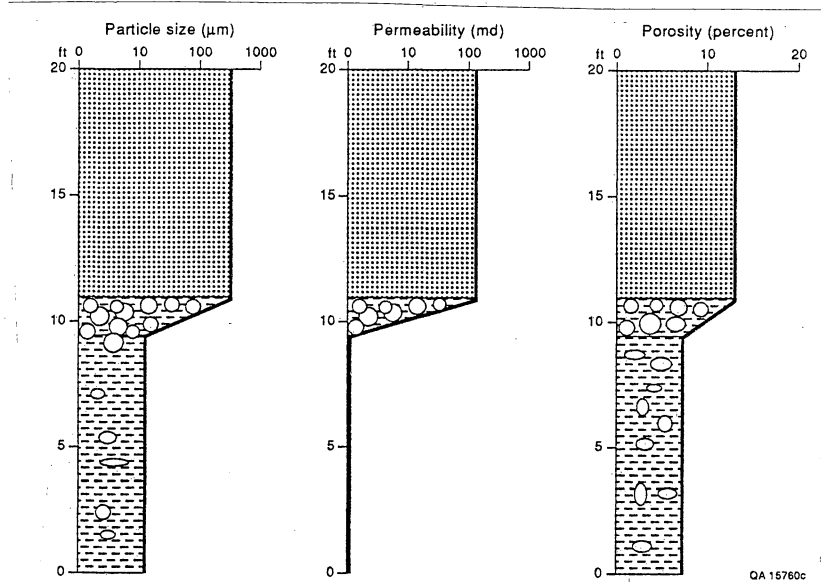
Figure 25. Vertical sequence of particle size, permeability, and porosity in parasequence 1 (ps1).

Grainstone (10 – 100 md)

Separate-vug grainstone (1 – 10 md)

Grain-dominated packstone (1 – 10 md)

Mud-dominated pack/wackestone (< 1.0 md)

Tight mudstone, fenestral caps (< 0.1 md)

☐1 Parasequence number
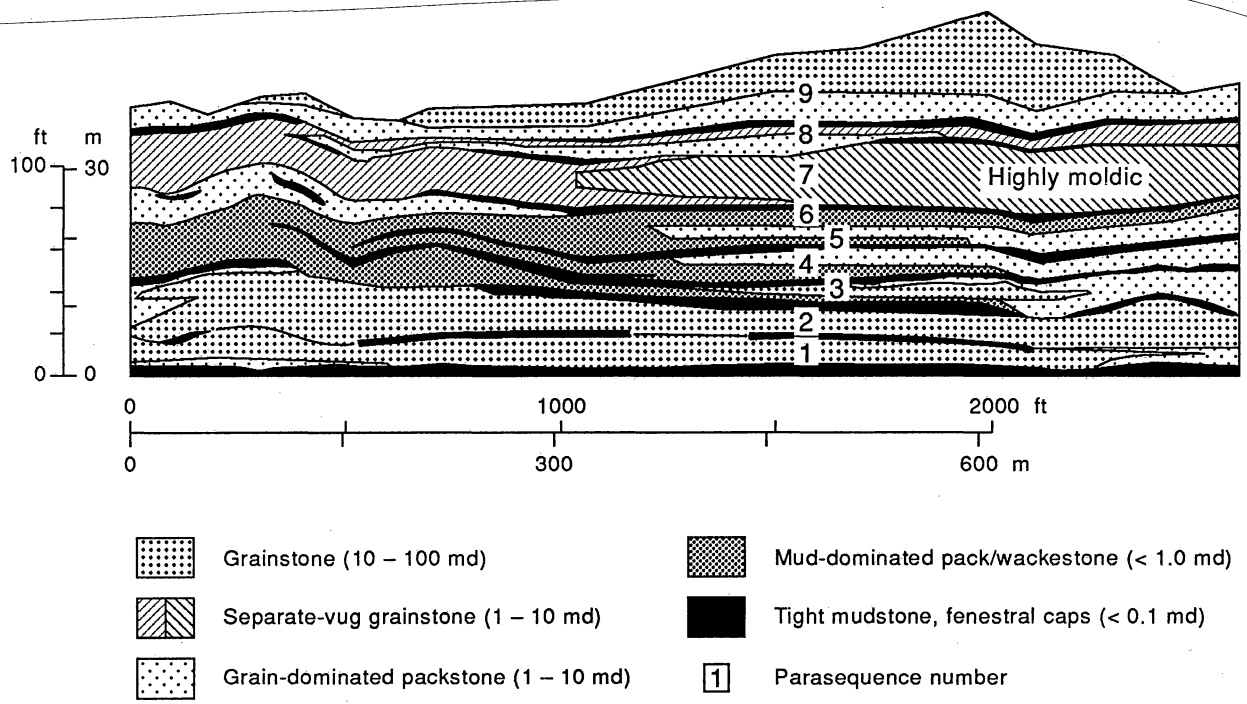
QA 15761c

Figure 26. Generalized distribution of petrophysical rock-fabric in Lawyer Canyon uSA1 parasequence window showing permeability ranges.

44

fabrics through slightly permeable grain-dominated packstone to permeable grainstones. The grainstone rock-fabric unit is continuous across most of the Lawyer Canyon Window but changes to grain-dominated packstone and mud-dominated fabrics at the southern end of the window (fig. 26). Parasequence 2 is similar to ps1 whereas the rock fabrics in ps3 through 6 change laterally from mud- to grain-dominated across the window. A laterally discontinuous grainstone is mapped in ps3 with mud-dominated fabrics shelfward (north) and grain-dominated packstones mapped basinward (south). The grainstone unit in ps9 varies in thickness and terminated abruptly basinward (south).

Permeability Characterization

Permeability measurements

In addition to core plug measurements, permeability was measured with an MFP which gauges gas-flow rates and pressure drop by pressing an injection tip against the rock surface. These data are used to calculate permeability values on the basis of a modified form of Darcy's law that incorporates effects of gas slippage at high velocity (Goggin and others, 1988). Core plug and MFP permeability measurements compared reasonably well for permeabilities >1 md, which is approximately the detection limit of MFP measurements (Goggin and others, 1988).

The distribution of permeability measurements taken from the upper San Andres at Lawyer Canyon is shown in figure 27. Sampling focused on ps1 and 7. Permeability distributions were measured at scales ranging from grids of 1-inch spacing to vertical transects that were spaced laterally between 5 and 100 ft and that contained permeability measurements at 1-ft vertical intervals.

The total number of MFP measurements at the Lawyer Canyon parasequence window was 1,584. Removing the outer weathering surface of the rock by chipping away an area of about 1 inch^2 gave the best representation of permeability. Preparing the sampling surface with a grinder produced permeabilities that were lower overall than those measured on chipped
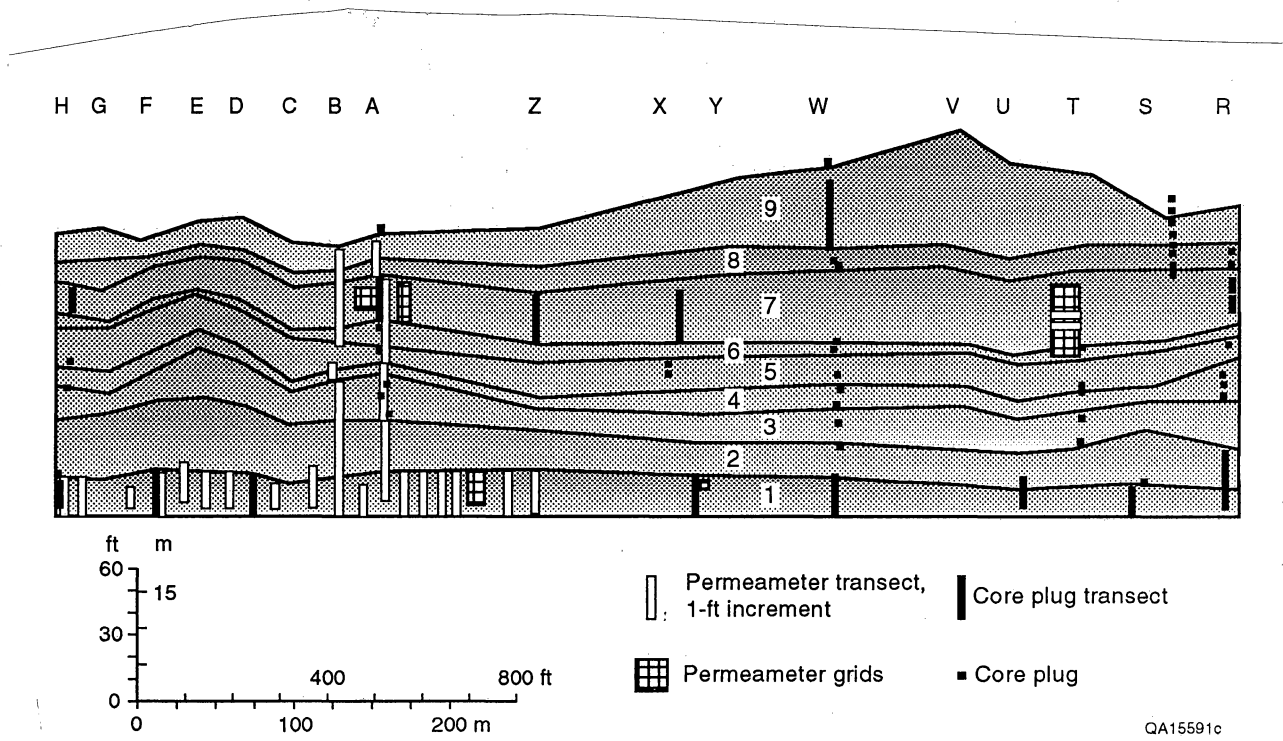
Figure 27. Location of sampling grids and transects of MFP measurements and core plugs.

surfaces, due to the plugging of pore space by fines (Kittridge and others, 1990). Typically, within each chipped area, several measurements were made and averaged. Depending on measurement discrepancies, as many as six different MFP readings were taken at various locations within the chipped area.

Spatial permeability patterns and variography

Spatial patterns in permeability were characterized and mapped in three steps. First, the data were contoured with an inverse-distance-squared algorithm to depict any trends or anisotropies in the data. Second, variograms were computed for different lag spacings and directions that were consistent with the data spacings and inverse-distance maps. Third, variogram models were fit to the variograms and were used to create point-kriged maps of spatial permeability patterns.

Standard contouring (inverse-distance-squared) of the detailed permeability transects spaced between 25 and 100 ft in parasequence 1 (fig. 27), using the CPS-1 contouring package, shows extreme heterogeneity (fig. 28) within the bar-crest facies, bar-flank facies, and shallow-shelf facies, which are collectively referred to as the grainstone facies of ps1. Permeability is controlled by total porosity, and separate-vug porosity (intragranular microporosity) has a second-order effect.

To evaluate heterogeneity at different scales, permeability measurements from the different measurement grids were analyzed using variography. Within the bar-crest facies of parasequence 1, permeability transects were typically spaced 25 ft apart. Between transects A and Z (fig. 27), vertical transects were spaced 5 ft apart. Horizontal and vertical variograms of the permeability data indicate a short-range correlation range of about 3 ft in the vertical direction and a possible correlation range of about 30 ft in the horizontal direction (fig. 29). In both cases, however, the spherical variogram indicates nugget constants of $\sigma_0 = 0.15$ md^2 and $\sigma_0 = 0.35$ md^2, which is as large as the sill. This relatively large nugget indicates small-scale

47

LOG PERMEABILITY (md)

☐	< -1.0	▤	0.5 – 1.0
▦	-1.0 – -0.5	▨	1.0 – 1.5
▧	-0.5 – 0	▥	1.5 – 2.0
▦	0 – 0.5	■	> 2.0
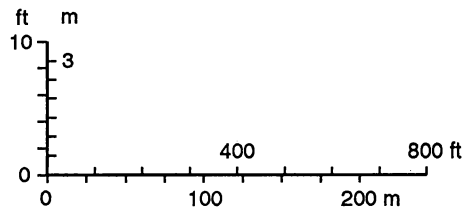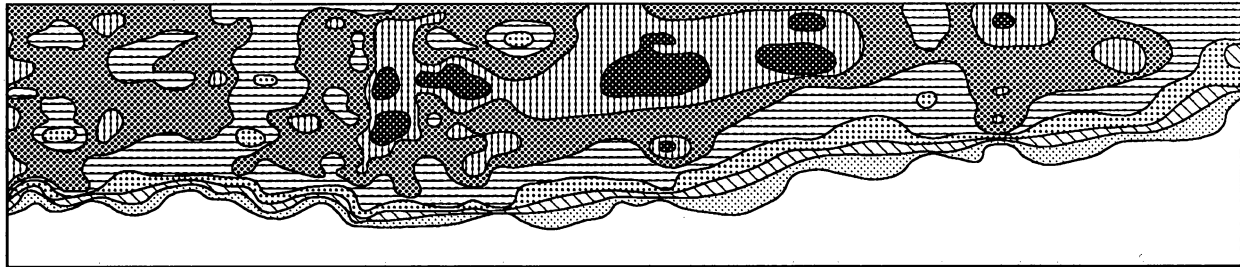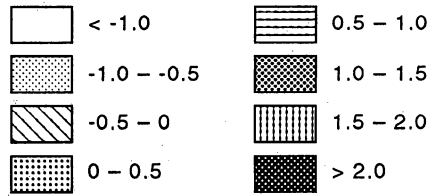
QA15989c

Figure 28. Permeability distribution for normalized parasequence 1 based on inverse-distance-squared contouring algorithm using CPS-1.
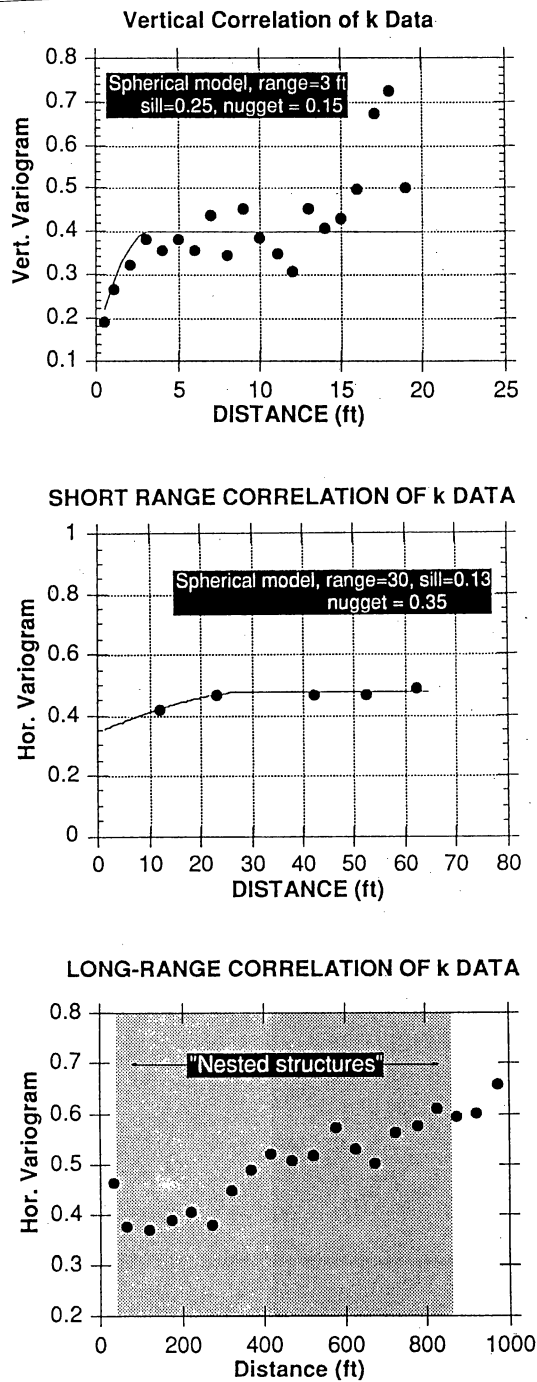
Figure 29. Sample variograms for the permeability transects from the grainstone facies in parasequence 1 (ps1): (a) vertical variogram based on all transects, (b) short-range horizontal variogram, based on the 5-ft grid between sections A and Z, and (c) long-range horizontal variogram, based on all transects spaced 25 and 100 ft.

random variability of permeability. The small-scale random permeability variation is apparent in permeability patterns of the smaller scale grids, which were measured at regular 1-ft (fig. 30) and 1-inch spacings (not shown here). Variogram analysis of these small-scale permeability grids did not indicate a noticeable permeability correlation but showed a large variability in permeability. Measurement accuracy of the minipermeameter typically decreased toward the lower detection limit of 1 md and may have accentuated some of the observed noise in the permeability data. Extending the log spacing of the variogram (fig. 29c) show the large-scale permeability pattern, characterized by nested structures. The range of these nested structures of about 400 ft is reflected in the overall permeability pattern shown in figure 28.

Using the fitted variogram models (fig. 29), a kriged permeability map was constructed for the northern half of parasequence 1, consisting predominantly of bar-crest facies. Note that the kriged permeability map (fig. 31), based on the vertical permeability transects spaced 25 ft apart, shows a much smoother distribution than does the kriged permeability map based on the 1-ft grid (fig. 30).

Conditional simulation realizations of permeability

Even though kriging can incorporate permeability correlation structures, it tends to average permeability over larger areas, ignoring small-scale heterogeneity. On the basis of the short-range correlation of permeability data (fig. 29), a series of stochastic permeability realizations were produced for the grainstone facies in ps1. The model extends laterally from 0 to 1,050 ft and is 17 ft thick, with block sizes of 1 by 5 ft. The simulations, conditioned to permeabilities measured along vertical transects spaced approximately 25 ft apart (fig. 27), incorporate the correlation structure from the variograms.

Two permeability distributions out of 200 stochastic permeability realizations were selected for flow simulations, representing maximum and minimum lateral continuity ($\bar{C}_h$) of domains having permeability values greater than 50 md (table 1). Comparison of the two
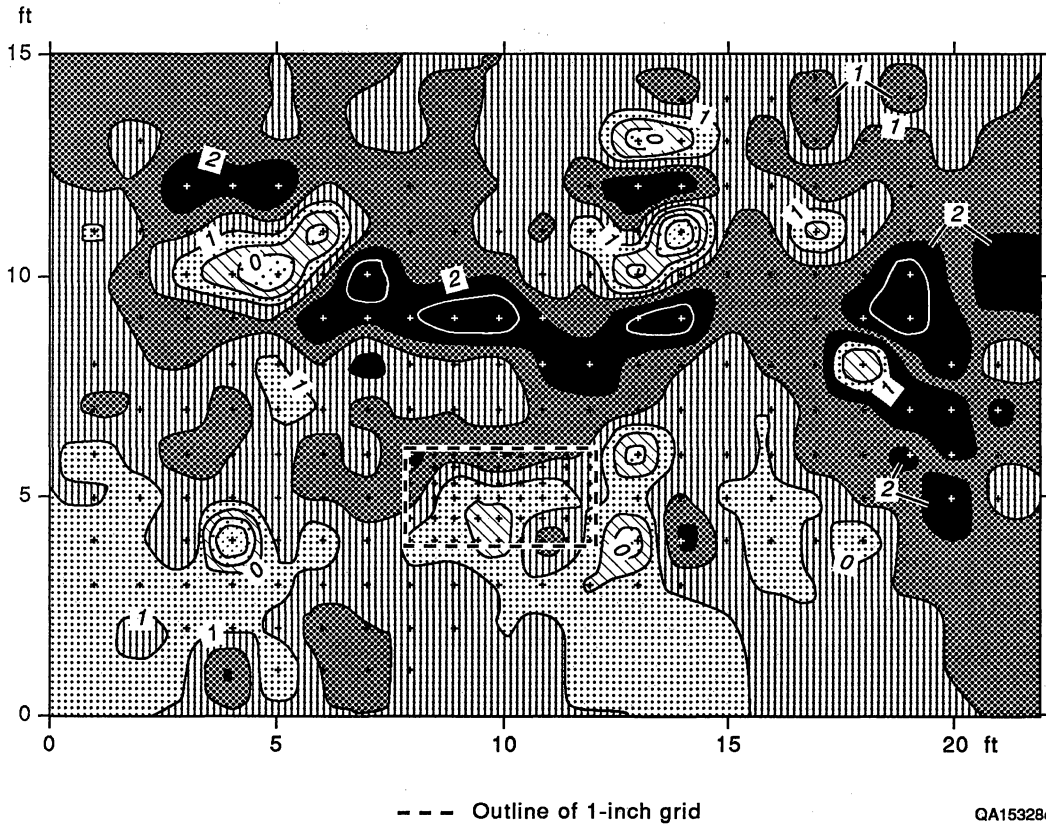
Figure 30. One-foot sampling grid in parasequence 1 (ps1) with kriged permeability contours.

- - - Outline of 1-inch grid

QA15328c
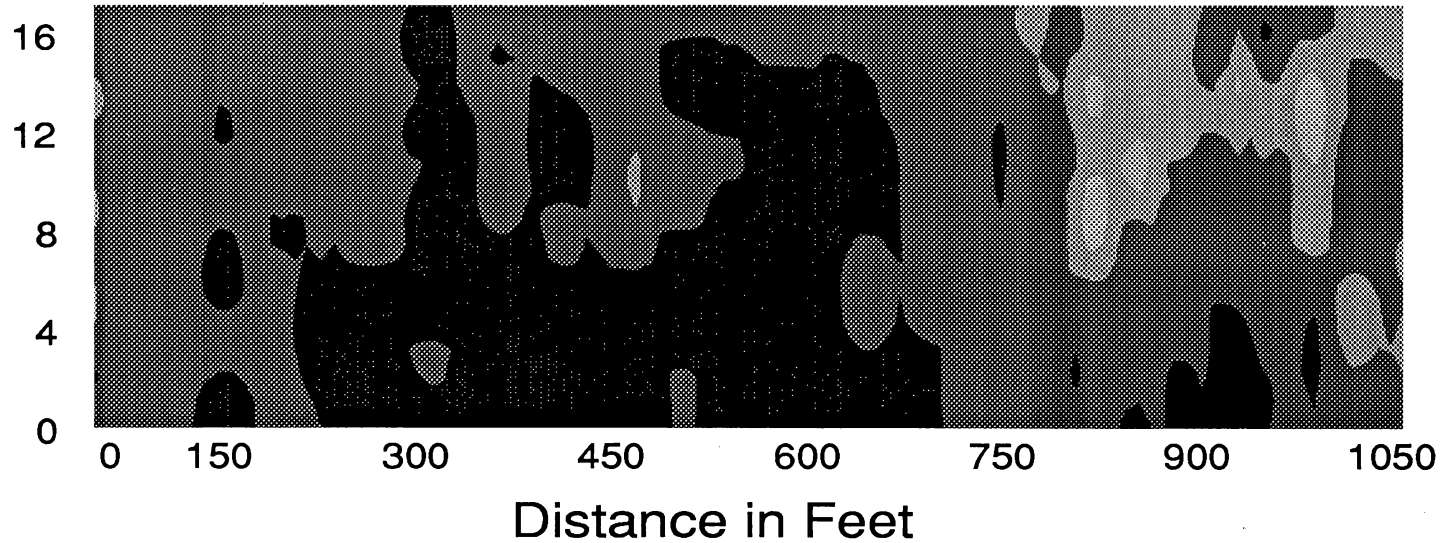
Figure 31. Kriged permeability distribution of the left part of parasequence 1 (ps1), representing the bar-crest facies.

permeability realizations (fig. 32a, b) does not show a noticeable difference. The ranges of 3 ft (vertical) and 30 ft (horizontal) (fig. 29a, b) are not immediately apparent in these realizations (fig. 32); the permeability patterns appear spatially uncorrelated because of the relatively large nugget, which is of the same magnitude as the sill (fig. 29). These conditional simulated realizations, however, preserve the spatial variability exhibited in the variograms, whereas the kriged permeability map (fig. 31) averages out much of this variability.

As mentioned above, measurement uncertainty of the minipermeameter may have accentuated some of the observed noise in the permeability data, which is reflected in the relatively large nugget of the variograms (fig. 29). For comparison, unconditional permeability realizations were produced that incorporate the mean, variance, and variogram range but have a zero nugget and a sill of 0.4 md^2 and are not conditioned to the actual permeability values. All of these unconditional permeability realizations have mean continuity values that are higher than those of the conditional permeability realizations based on a 0.2-md^2 nugget (table 1). Unconditional realization 45 (fig. 33), which was selected on the basis of low continuity of relatively permeable zones, shows a smoother permeability pattern than that of a conditional permeability realization having a relatively high nugget (fig. 32). For comparison of waterflooding results, the different permeability realizations were corrected to the same mean permeability, which was equivalent to the data mean of log k = 1.219 md (table 1).

Waterflood Simulation of Parasequence 1

Waterflooding of the hypothetical two-dimensional reservoir was simulated by injecting water along the right boundary and producing along the left boundary. Injection and production were controlled by prescribed pressure conditions of 2,450 and 750 psi, respectively. A series of numerical simulations was performed to evaluate different effects associated with the observed heterogeneity on production characteristics (table 3). Flow simulations incorporating the observed heterogeneity were compared with those using a mean

53

(a)

LOG PERMEABILITY [md]
COND.SIMULATION:REALIZATION No.7

Distance in Feet

> 3   1 - 1.5

2 - 3   0 - 1

1.5 - 2   < 0
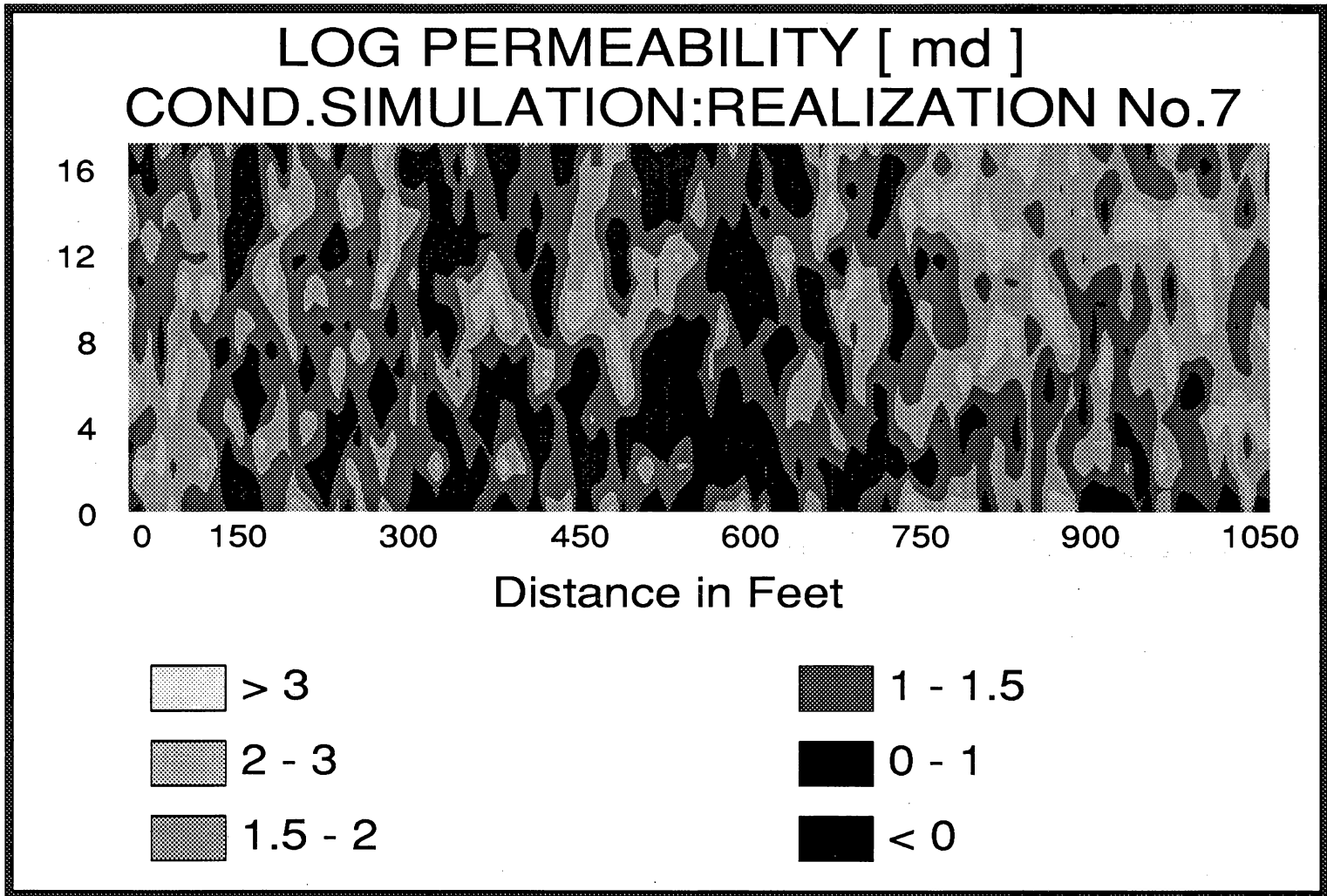
Figure 32. Conditional permeability distributions of (a) realization 7, representing lower continuity, and (b) realization 11, representing higher continuity of high-permeability zones.

(b)

LOG PERMEABILITY[md]
COND.SIMULATION:REALIZATION No.11

Distance in Feet

Legend:
- > 3
- 2 - 3
- 1.5 - 2
- 1 - 1.5
- 0 - 1
- < 0
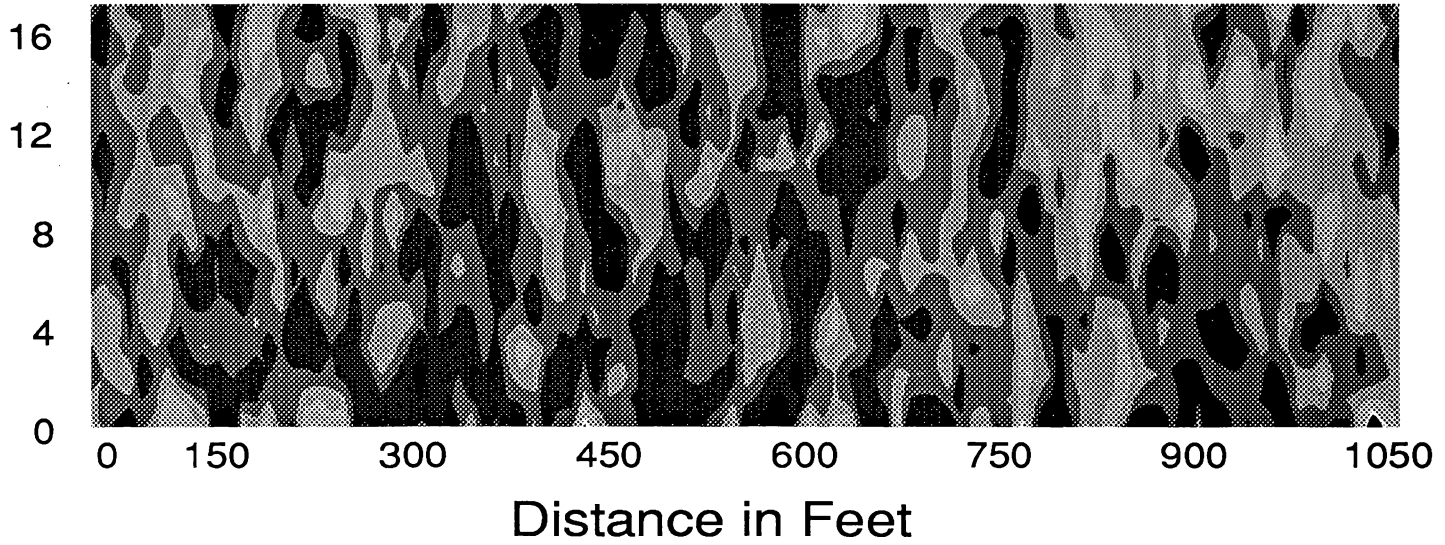
Figure 32. Continued.

**LOG PERMEABILITY [md]
UNCOND.SIMULATION No.45(Co=0.)**

Distance in Feet

> 3

2 - 3
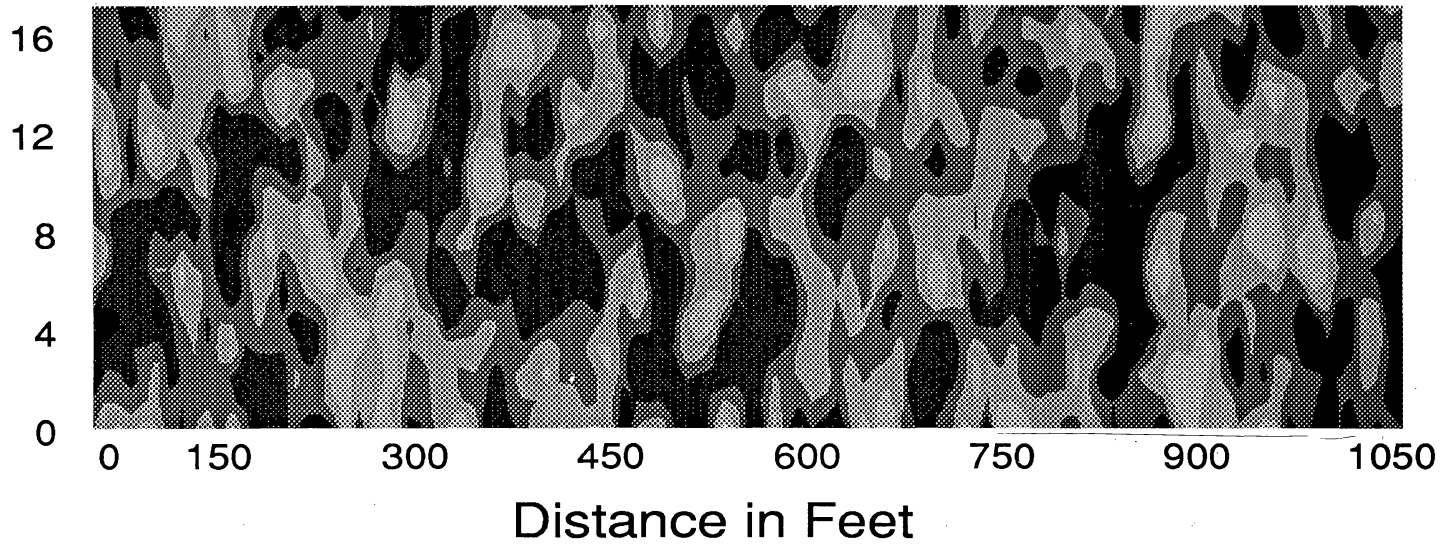
1.5 - 2

1 - 1.5

0 - 1

< 0

Figure 33. Unconditional permeability distribution of realization 45, representing higher continuity of high permeability zones.

Table 3. Input parameters for waterflood simulations of grainstone facies in parasequence 1 (ps1).

No.	Permeability realization	Mean log-k (md)	Statistics Variance log-k (md^2)	Nugget (md^2)	Sill (md^2)	Mean horizontal continuity ($\overline{C}_h$) (ft)
1*	7	1.219	0.42	0.2	0.2	7.53
2	7	1.219	0.42	0.2	0.2	7.53
3	11	1.219	0.45	0.2	0.2	8.82
4	45	1.219	0.38	0.0	0.4	11.95
5	kriged	1.219	0.46	0.2	0.2	N/A
6*	facies-averaged	1.219	N/A	N/A	N/A	N/A

*Single relative-permeability and capillary-pressure curves.

Fluid properties:
    Oil viscosity   1.000 cP
    Oil density   55 lb/ft^3
    Water density   64 lb/ft^3

T3

permeability to evaluate whether the observed permeability heterogeneity could be represented by a geometric-mean permeability and to determine the possible impact of short-range permeability correlation on production characteristics.

Development of parasequence flow model

Input data for the simulator included the stochastic permeability distributions, porosities, and relative-permeability and capillary-pressure curves. Porosity-permeability relationships established on the basis of core-plug analyses for grainstones in ps1 were used to calculate porosity distributions from the stochastic permeability realizations (fig. 32). The empirical porosity-permeability relation used in this analysis is equation (7). Similarly equation (4), an empirical relationship between water saturation, intergranular porosity, and capillary pressure established for grainstones, was used to calculate capillary pressure as a function of water saturation and porosity of the grainstone facies in ps1. Residual oil saturation was assumed to be uniform at 25 percent.

The relative-permeability functions for oil and water were determined from the following equations (Honarpour and others, 1986):

$$k_{rw} = k_{rw}{}^0 \; \frac{(S_w - S_{wr})^{N_w}}{(1 - S_{or} - S_{wr})} \tag{8}$$

$$k_{ro} = k_{ro}{}^0 \; \frac{(1 - S_w - S_{wr})^{N_o}}{(1 - S_{or} - S_{wr})} \tag{9}$$

where S_{or} and S_{wr} are the residual oil saturation and the residual water saturation, respectively. The exponents N_w and N_o were derived from fitting relative permeability data obtained from grainstone fabric of two Dune field cores. Both exponents were approximately 3 and were determined from the slope of the regression line representing the log of relative permeability versus the log of the normalized saturations in equations (8) and (9). Similarly, the relative-permeability end points $k_{rOAL(w,}{}^0{}_)$ and $k_{rOAL(w,}{}^0{}_)$ were derived from the intercepts of the log-log plots of the measured relative-permeability data versus saturation, which were 0.266 and 0.484,

respectively, and correspond to residual oil saturation S_{or} = 0.25 and residual water saturation S_{wr} = 0.1, respectively.

Porosities derived from the different permeability realizations through the permeability-porosity transform in equation (1) typically range between 5 and 25 percent. Four relative-permeability and capillary-pressure curves representative of four porosity intervals were used: 5 to 10 percent, 10 to 15 percent, 15 to 20 percent, and 20 to 25 percent. For these porosity intervals, residual water saturations calculated from equation (2) were used to compute the relative-permeability curves according to equation (3). For simulations 1 and 4, only one relative-permeability curve and one capillary-pressure curve were used, based on the arithmetic average of porosity of realization 7. The relative-permeability and capillary-pressure curves used in the different flow simulations are shown in figures 34 and 35, respectively.

Simulation: runs and results

Six numerical simulations were run (table 3), including (1) conditional permeability realization 7 (fig. 32a), representing low continuity of permeable zones and using a single relative-permeability and a single capillary-pressure curve based on the arithmetic mean of porosity; (2) conditional permeability realization 7, incorporating four porosity-dependent relative-permeability and capillary-pressure curves; (3) conditional permeability realization 11 (fig. 32b), representing low continuity of permeable zones; (4) unconditional permeability realization 45 (fig. 33), representing low continuity of permeable zones assuming zero nugget; (5) kriged permeability distribution (fig. 31), incorporating porosity-dependent relative-permeability and capillary-pressure relationships; and (6) uniform permeability distribution, based on the geometric mean of measured permeability.

Computed water saturations of all simulations exhibited relatively sharp and vertical injection fronts despite the large variations in permeability, initial saturations, and capillary pressures in some simulations (table 3).

RELATIVE-PERMEABILITY CURVES
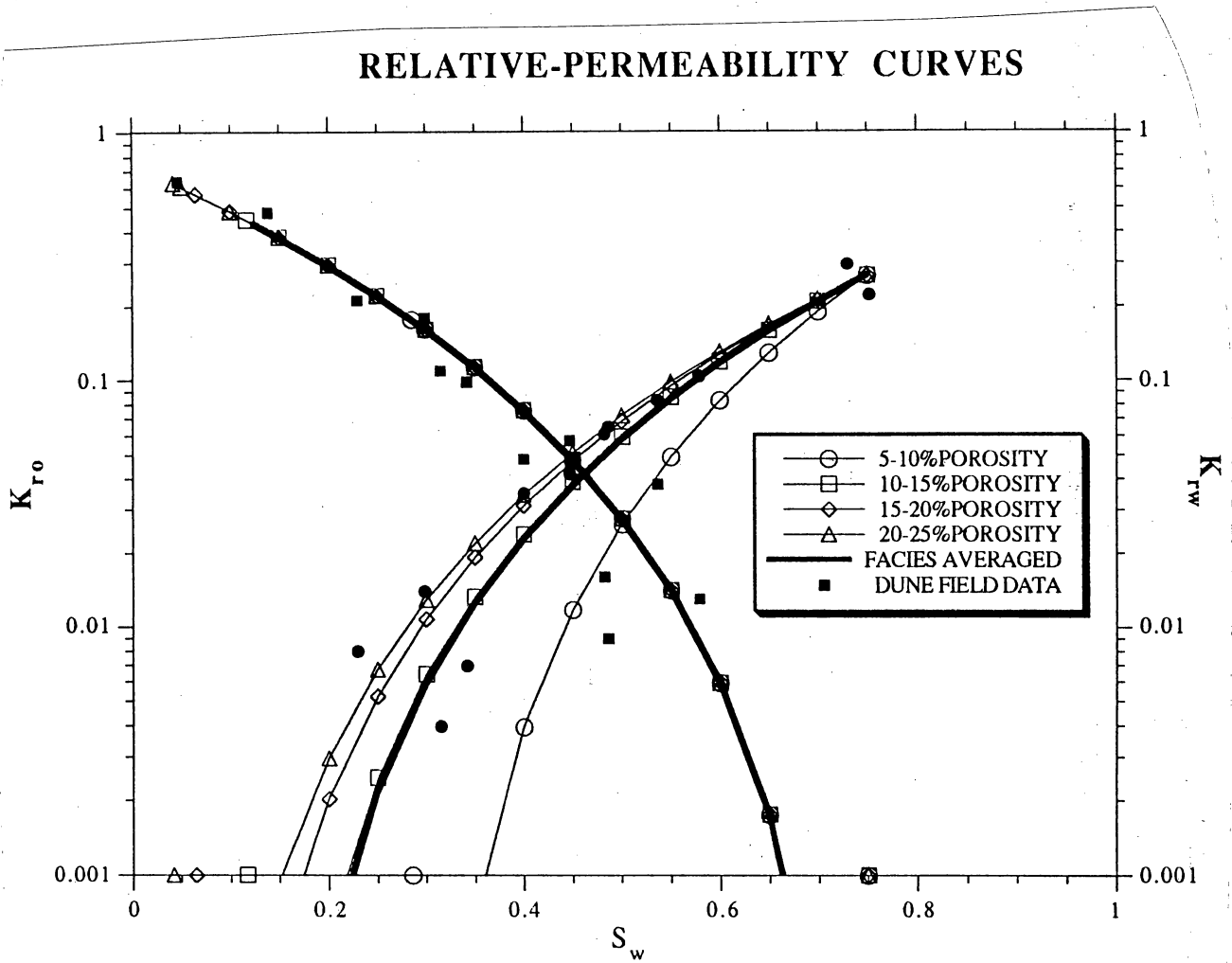
Figure 34. Relative-permeability curves used for the different waterflood simulations in parasequence 1 (ps1).

CAPILLARY-PRESSURE CURVES
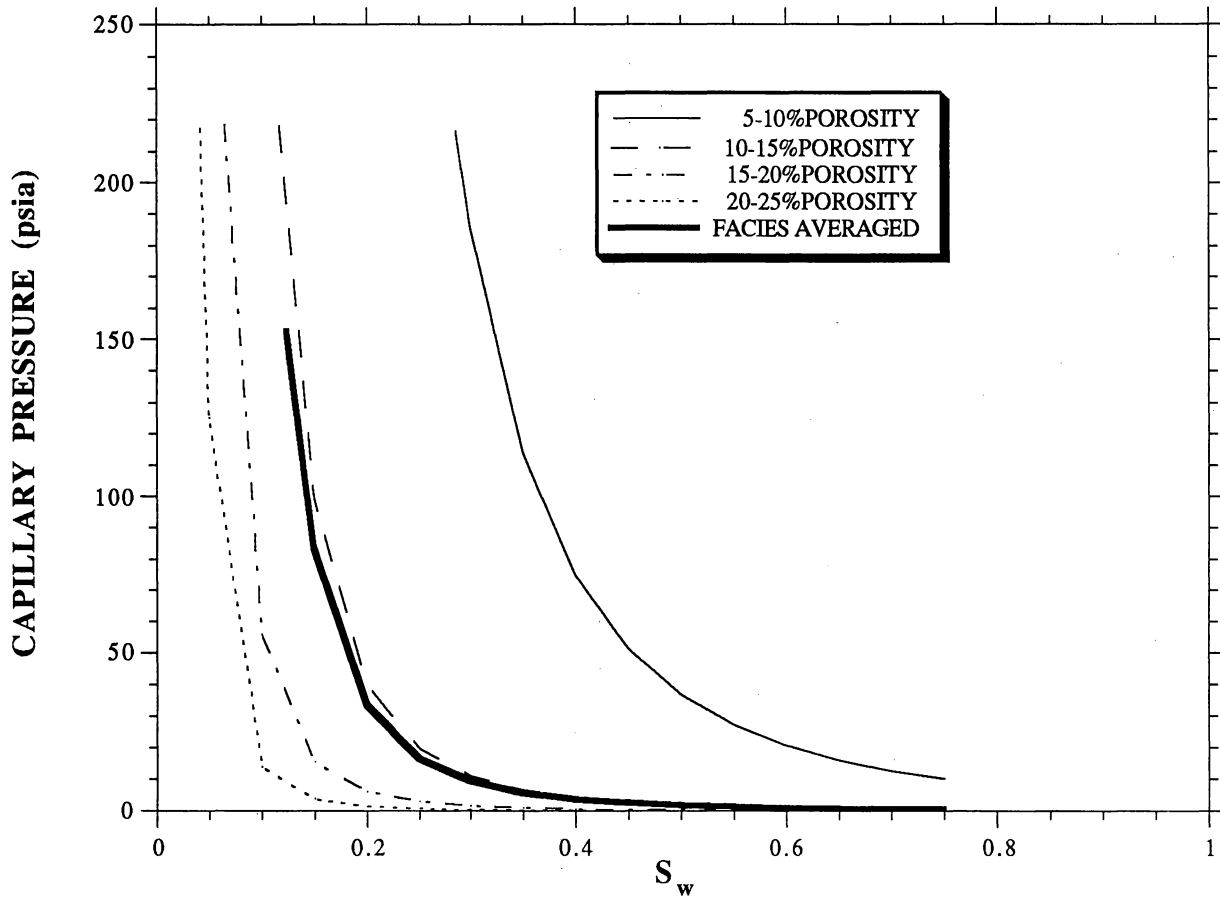
Figure 35. Capillary-pressure curves used for the different waterflood simulations in parasequence 1 (ps1).

Initial water saturation in simulation 1 (fig. 36) is uniformly calculated from equation (2), using the arithmetic mean of porosity and assuming a reservoir height above the free-water level of 500 ft. Initial water saturation in simulation 2 is also calculated from equation (2), but by using variable porosity values. This results in the uneven initial saturation distribution to the left of the water-injection front (fig. 37). Water saturations in the flooded zones are dependent upon capillary pressure as well as relative and absolute permeability. In simulation 1 (fig. 36) a single capillary-pressure curve and a single relative-permeability curve (figs. 34 and 35) were used, resulting in a much smoother saturation distribution than those in simulation 2 (fig. 37). Despite the relatively heterogeneous permeability distribution, the water-injection front in both simulations is relatively sharp and approximately vertical.

Production characteristics of all six simulations are shown in figures 38 through 40. Each production curve for the different permeability realizations is characterized by an initial peak, followed by a gentle decline and then a rapid decline. The rapid decline represents the relatively sharp breakthrough of the water-injection front (fig. 38). Water breakthrough is dependent on the mean continuity of permeable zones in the stochastic permeability realizations. Water breakthrough in realization 11, representing high continuity of permeable zones, occurs earlier than that in realization 7, representing low continuity of permeable zones. Although unconditional realization 45 represents low continuity of permeable zones, its mean horizontal continuity of 11.95 ft based on a zero nugget is higher than that in realization 11, which represents high continuity of permeable zones but has a nugget of 0.2 md^2 (table 3). Higher continuity of relatively permeable zones results in higher interconnection of these zones and thus produces higher effective permeability than do permeability realizations characterized by low continuity (Fogg, 1989). As a result, unconditional permeability realization 45 shows the earliest water breakthrough because of the overall higher effective permeability. Also, the production curve of unconditional permeability realization 45 illustrates the highest initial production rate but a subsequently steeper decline than production curves from the conditional permeability realizations (fig. 38). As with the water breakthrough, the

62
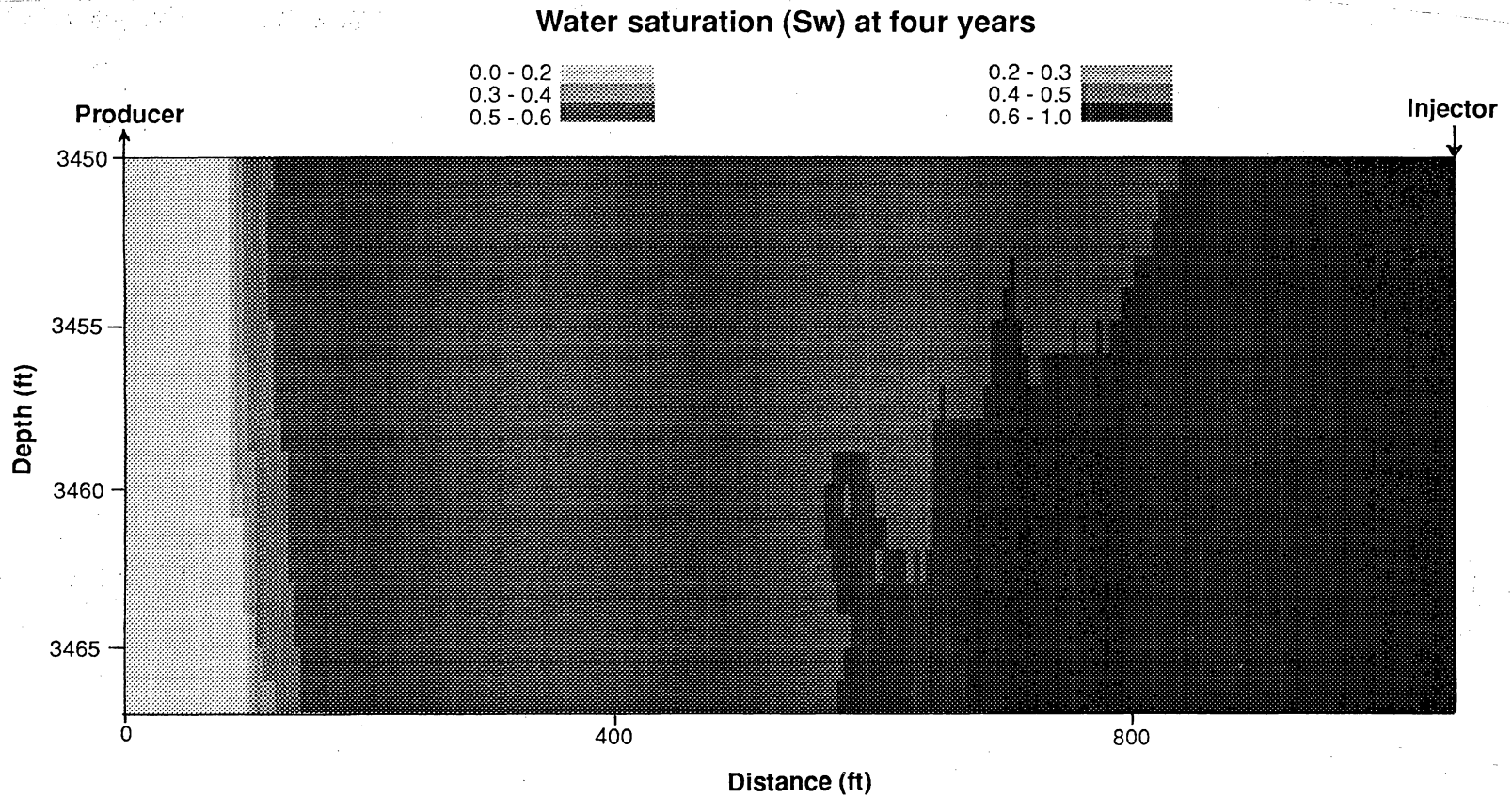
Figure 36. Computed water saturations for simulation 1 after injecting water for 4 yr, incorporating the permeability realization 7 assuming uniform initial saturation and single relative-permeability and capillary-pressure curves based on arithmetic-mean porosity.

Water saturation (Sw) at four years

0.0 - 0.2		0.2 - 0.3
0.3 - 0.4		0.4 - 0.5
0.5 - 0.6		0.6 - 1.0

Producer

Injector

Depth (ft)

3450

3455

3460

3465

0

400

800

Distance (ft)
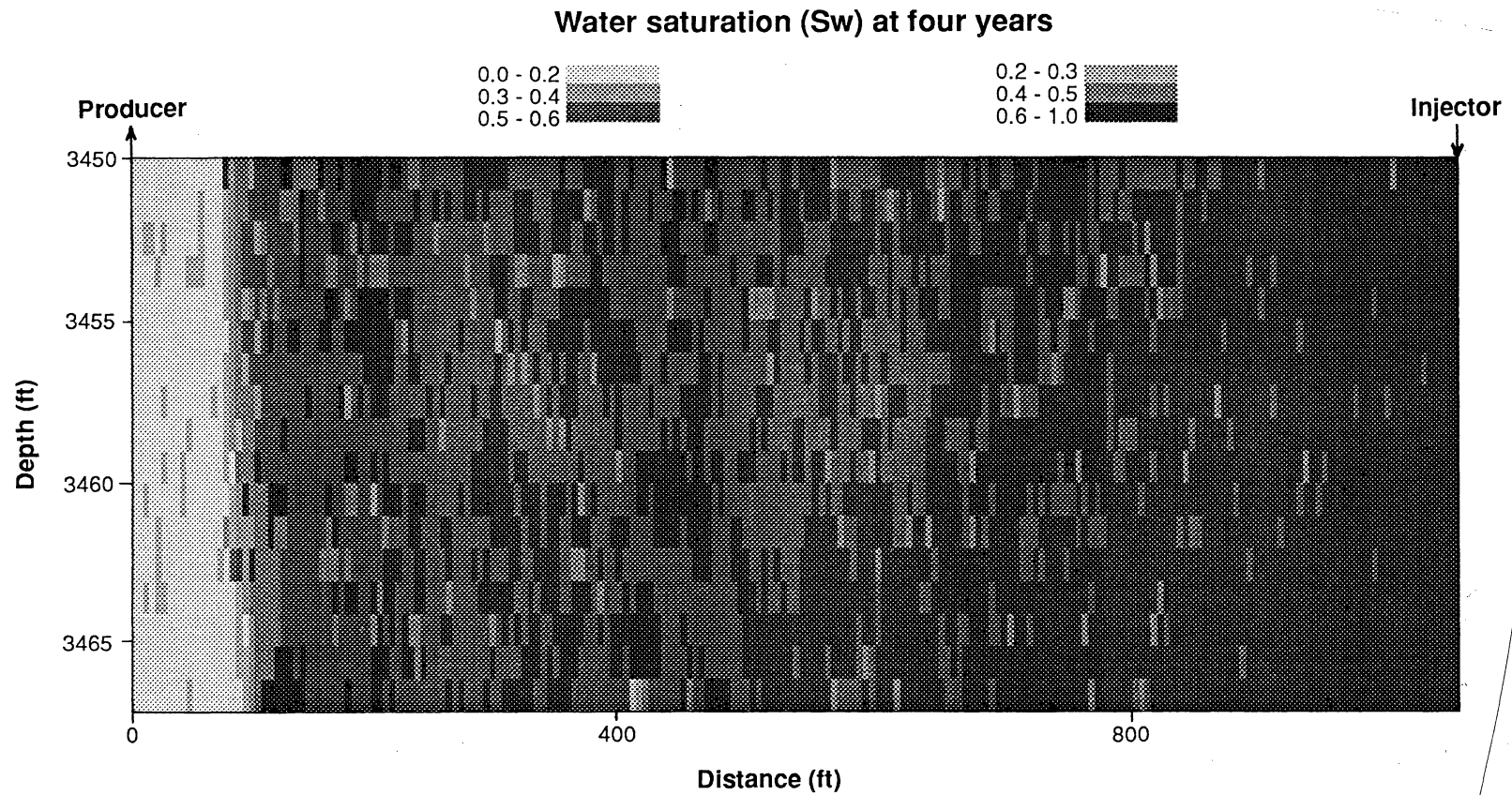
Figure 37. Computed water saturations for simulation 2 after injecting water for 4 yr, incorporating the permeability realization 7 (assuming relative-permeability curves and capillary-pressure curves dependent on porosity range).
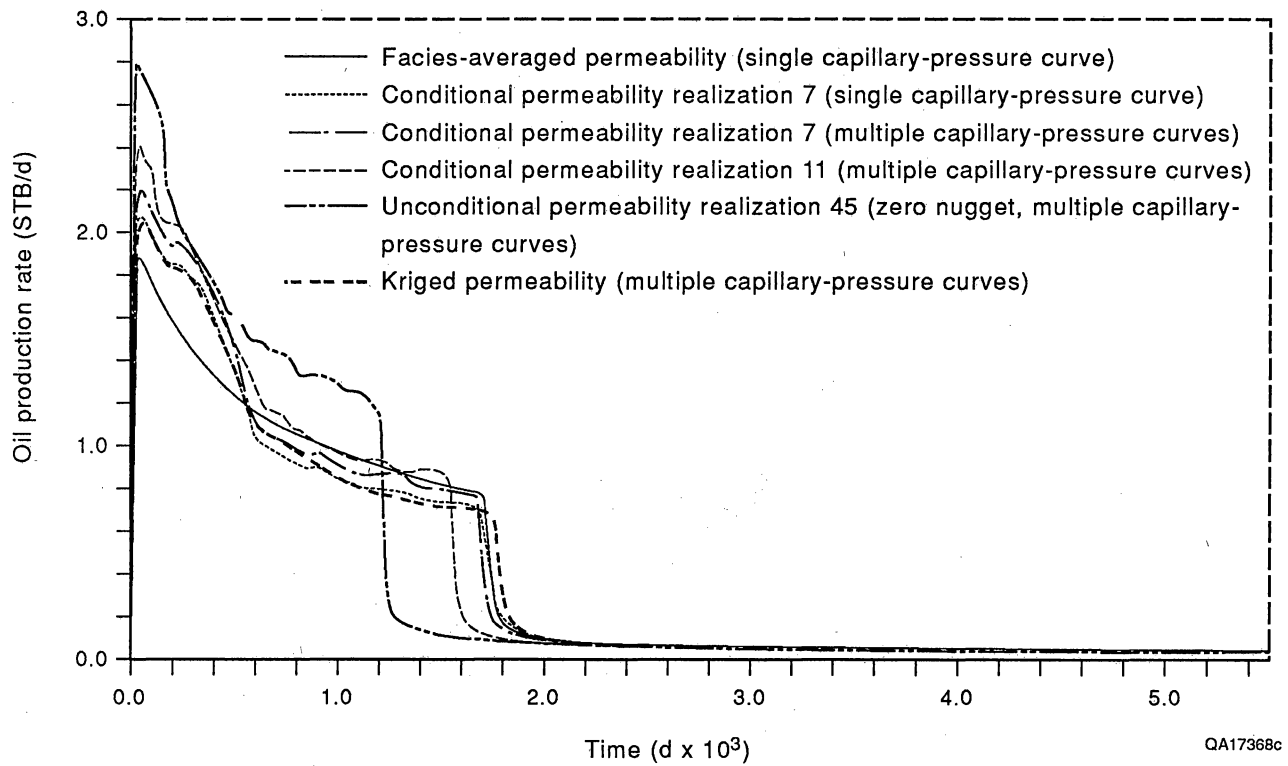
Figure 38. Oil-production rate versus time for waterflood simulations in parasequence 1 (ps1).
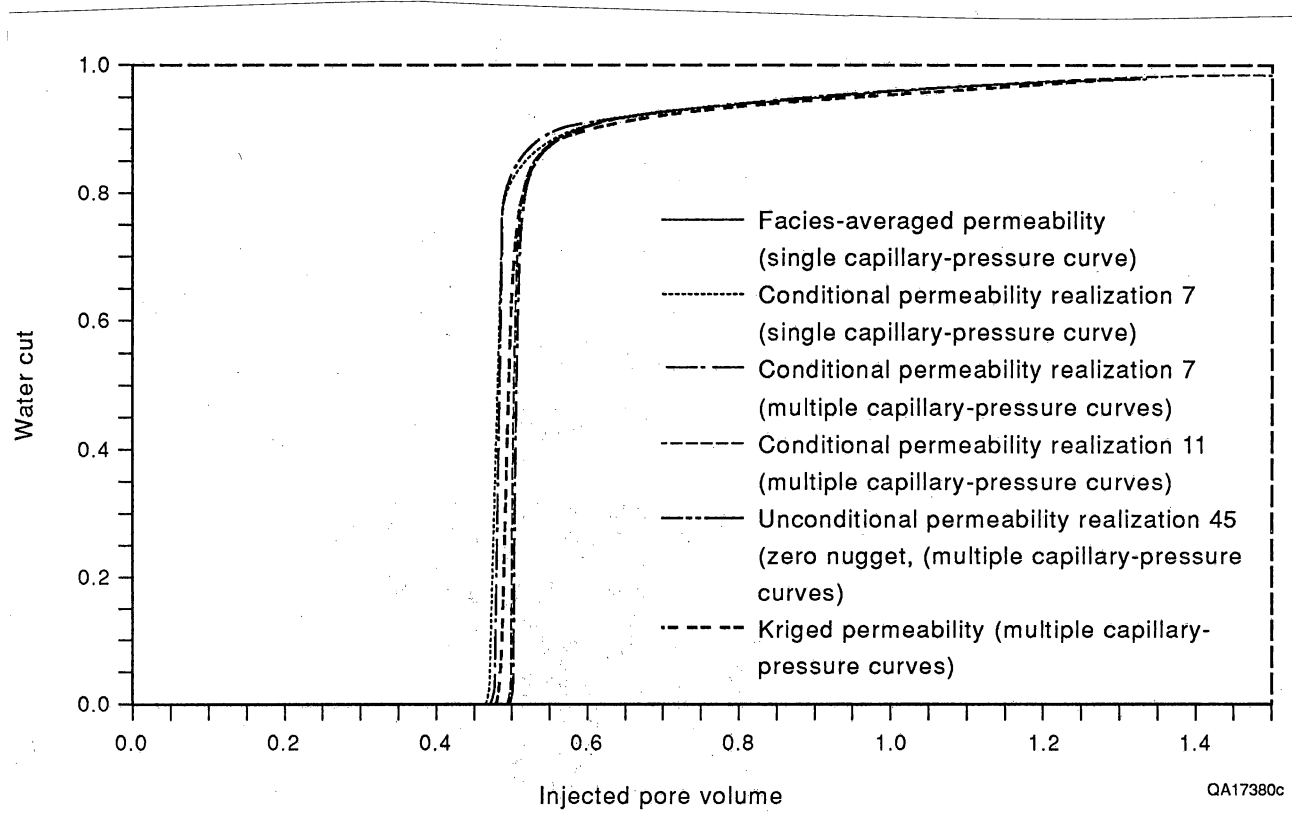
Figure 39. Water-oil ratio versus injected pore volumes for waterflood simulations in parasequence 1 (ps1).
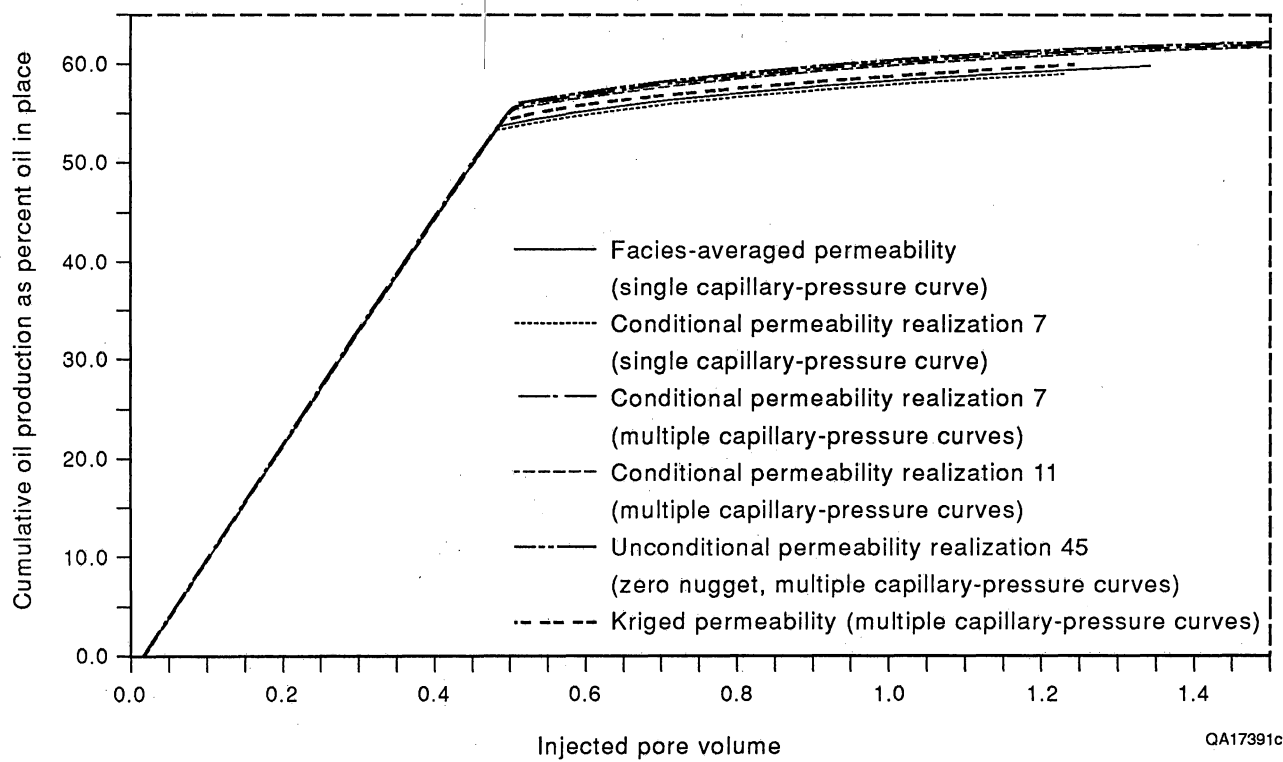
Figure 40. Cumulative oil production as percentage of original oil in place for waterflood simulations in parasequence 1 (ps1).

initial production peaks of the stochastic permeability realizations are also dependent on the mean horizontal continuity.

The kriged permeability distribution shows a production curve similar to that of the conditional permeability realizations. This suggests that the larger scale permeability variation (fig. 31) controls the overall production characteristics and that the small-scale permeability variations incorporated into the stochastic permeability realizations have little importance (figs. 32 and 33). In comparison, the facies-averaged permeability distribution, which has no spatial permeability variation, indicates a smooth, approximately exponential production decline before the water breakthrough, which occurs at approximately the same time as that in the kriged and conditional permeability realizations.

Water cut plotted against injected pore volume shows nearly identical curves for the stochastic permeability realizations, incorporating porosity-dependent capillary-pressure curves (fig. 39). Simulation 1 with permeability realization 7, incorporating a single capillary-pressure curve based on an arithmetic mean porosity and simulation 6 with the facies-averaged permeability distribution, incorporating a single capillary-pressure curve, show earlier water-breakthrough curves than those of the stochastic permeability realizations, incorporating porosity-dependent capillary-pressure curves (fig. 39). In comparison, the kriged permeability distribution falls between the two groups (fig. 39).

The sweep efficiency is improved using porosity-dependent capillary pressures, as indicated by the cumulative oil production as percent total oil in place (fig. 40). The waterflood simulations incorporating multiple capillary-pressure and relative-permeability curves (simulations 2 through 5) indicate higher sweep efficiency than those with single capillary-pressure and relative-permeability curves (simulations 1 and 6). Note that the sweep efficiency in simulation 5, representing the kriged permeability distribution, is slightly lower than the stochastic permeability realizations (simulations 2 through 4), indicating that the small-scale heterogeneity causes an increase in sweep efficiency.

68

Development of the outcrop window flow model

A flow model was developed by integrating the rock-fabric descriptions, parasequence framework, and average petrophysical properties (fig. 26). The reservoir flow model distinguishes 11 flow units that have different average permeability, porosity, initial water saturation, and residual oil saturation (table 4). Thin, dense, and tight mudstone beds form discontinuous flow barriers at the bases of the parasequences. Fenestral caps, found at the top of some parasequences, are considered to be dense and tight compared with those found in San Andres reservoirs.

Porosity and permeability values are based on averages from core plug and MFP measurements. Nonvuggy grainstones with permeabilities typically ranging from 10 to 50 md are found in ps1, 2, 3, and 9. Grain-dominated packstones with permeabilities ranging from 1 to 10 md and mud-dominated packstones and wackestones with permeabilities ranging from 0.1 to 1 md dominate ps3 through 6 and ps8. Separate-vug porosity is concentrated in ps7, and the permeability ranges from 1 to 10 md.

In ps7, the highly moldic fabric (>10 percent separate vugs) changes laterally to the moldic fabric with no change in average permeability, although the average porosity changes from 22 percent in the highly moldic to 15 percent in the moldic.

Initial water saturations for the different flow units were calculated using the porosity/water-saturation transforms for the three rock-fabric classes (fig. 9) and average porosities. It was assumed that the grainstones in ps7, characterized by variable amounts of separate-vug porosity, have the same porosity-saturation relationship as the nonvuggy grainstones in ps1, 2, 3, and 9. The effect of vuggy porosity was accounted for by assigning a higher residual oil saturation to the grainstones in ps7.

Table 4. Properties of rock-fabric flow units for Lawyer Canyon outcrop reservoir model.

Flow units	Rock fabric	Depositional facies	Porosity (arithm. average)	Permeability (geometric average, md)	Initial water saturation	Residual oil saturation
1	Mudstone	Flooded shelf tidal flat	0.04	0.01	0.9	0.01
2	Wackestone	Shallow shelf I	0.105	0.30	0.405	0.4
3	Grain-domin. packstone	Shallow shelf I	0.085	4.50	0.214	0.35
4	Grain-domin. packstone	Shallow shelf II bar top	0.129	1.80	0.40	0.35
5	Grain-domin. packstone	Shallow shelf II	0.118	5.30	0.243	0.35
6	Grainstone (moldic)	Shallow shelf II	0.145	0.7	0.091	0.40
7	Grainstone (moldic)	Shallow shelf I shallow shelf II bar crest bar top	0.159	2.2	0.077	0.40
8	Grainstone (highly moldic)	Shallow shelf II bar crest bar-accretion sets	0.23	2.5	0.041	0.40
9	Grainstone	Bar flank	0.095	9.5	0.189	0.35
10	Grainstone	Bar crest bar-accretion sets	0.11	21.3	0.147	0.25
11	Grainstone	Bar crest	0.135	44.0	0.103	0.25

Fluid properties:
  Oil viscosity   1.000 cP
  Water viscosity 0.804 cP
  Oil density   55 lb/ft^3
  Water density   64 lb/ft^3

70

Relative permeabilities for the different flow units are based on the shapes of relative-permeability curves derived from fitting relative-permeability data obtained from cores in the Dune field, West Texas. Similar to the relative-permeability curves in figure 34, the fitted curves were adjusted to the computed initial water saturations and to the residual oil saturations of the different flow units (table 4). Although the shape of the relative-permeability curves was obtained by fitting relative-permeability measurements from grainstone cores from the Dune field reservoir, West Texas (fig. 34), the same curve shapes were used in this study not only for the grainstone rock fabrics, but also for the grain-dominated packstone and mudstone-wackestone rock fabrics. Only the relative-permeability endpoints were adjusted according to the computed initial water saturations and assumed residual oil saturations.

Capillary-pressure curves were calculated on the basis of average porosities and rock-fabric classifications of the different flow units. The porosity-dependent saturation-capillary-pressure relationship for the rock-fabric classes are give in equations (4), (5), and (6).

The flow model is discretized in 4,089 irregularly shaped grid blocks, representing the spatial distribution and petrophysical properties of the different rock fabrics and depositional facies (table 4). Reservoir block sizes are 100 ft in the horizontal direction and have variable thicknesses in the vertical direction, ranging from <0.5 ft to several feet. The constructed reservoir model incorporates the general geometry and the spatial distribution of the different facies mapped in the outcrop, as shown by the distribution of initial water saturation of the discretized flow units (fig. 41).

Simulation: runs and results

In a series of waterflood simulations, various factors affecting reservoir-flow behavior were examined (table 5) using the ECLIPSE reservoir simulator. Simulation EC-A represents the base scenario, which is used to describe waterflooding in this hypothetical reservoir. Production characteristics of simulation EC-A were compared with those from other simulations to evaluate

71
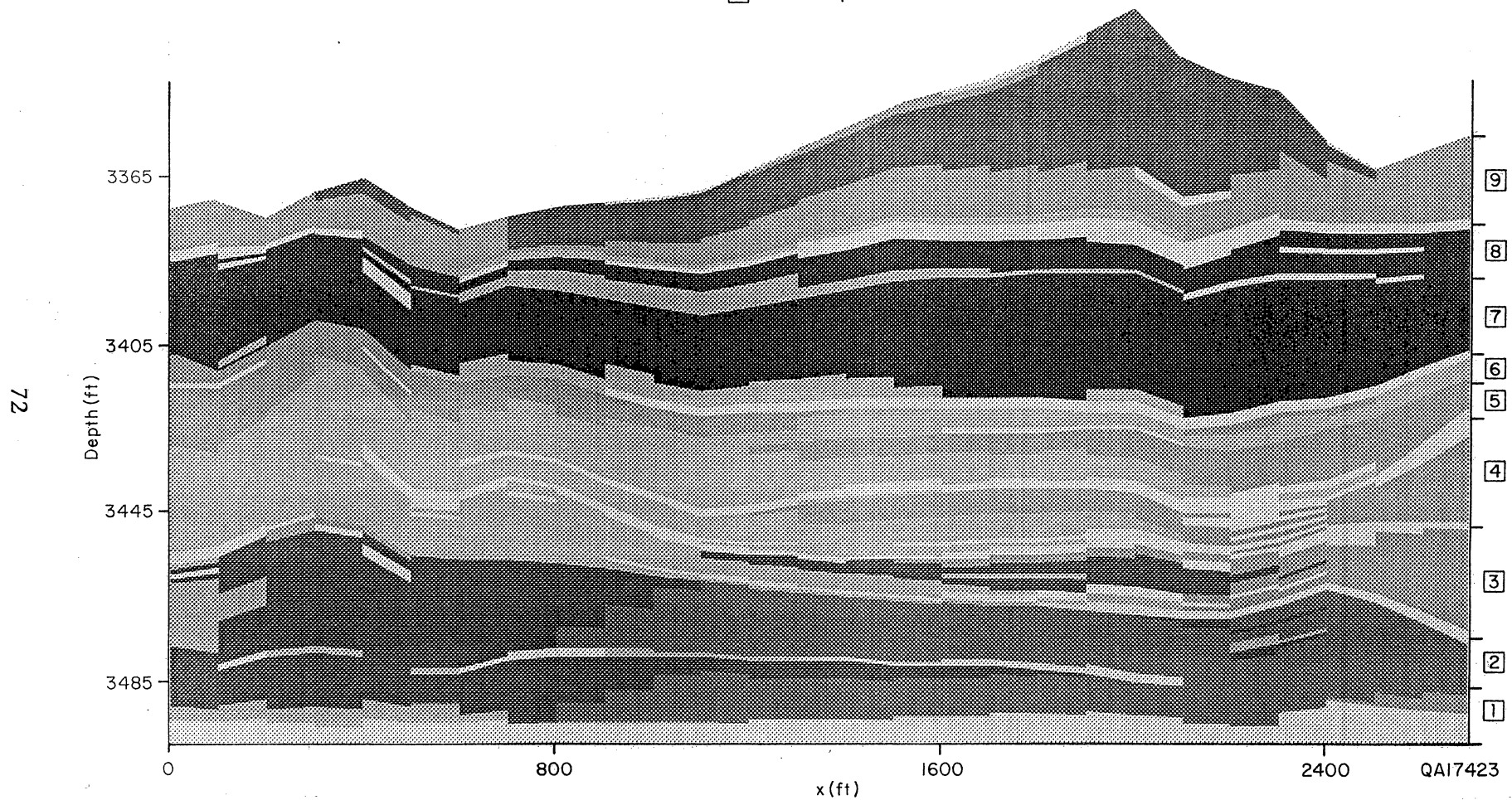
Figure 41. Initial water saturation of the flow units of the outcrop model.

Table 5. Waterflood simulations of the Lawyer Canyon outcrop model.

| Sim. no. | Grid | Model scenario | | |
		Production well location	Capillary pressure	Permeability data
EC-A	irregular	right	yes	facies-averaged
EC-B	irregular	right	no	facies-averaged
EC-N	normalized	right	yes	facies-averaged
EC-DP	normalized	right	single	linear interpol. between wells
EC-R	irregular	left	yes	facies-averaged
EC-F	irregular	middle	yes	facies-averaged

effects of capillary pressures (simulation EC-B), model conceptualization (simulations EC-N and EC-DP), and different injection practices (simulations EC-R and EC-F).

Waterflooding of the hypothetical Lawyer Canyon outcrop reservoir was simulated by injecting water through a fully penetrating well along the right side of the model and by producing from a well at the left side (fig. 41). The injection and production rates were controlled by prescribed pressures of 4,350 and 750 psi, respectively.

The change in computed water saturation for simulation EC-A after water injection of 20 yr (fig. 42a), 40 yr (fig. 42b), and 60 yr (fig. 42c) demonstrates that the high-permeability grainstone rock-fabric units in ps1, 2, and 9 are preferentially flooded. Furthermore, flooding is controlled by the relatively tight mudstone units separating most of the parasequences. The grainstone facies in ps7 and 8 are characterized by somewhat lower permeabilities and higher porosities than those in ps1, 2, and 9, due to vuggy pore structure (table 4); consequently, the water-injection front does not advance as far as that in ps9 (fig. 42). However, the water-injection front in ps3 through 6 appears to have advanced farther than that in ps7 and 8, although the permeability of the predominantly wackestone rock fabrics in ps3 through 6 is lower than that of the moldic grainstone rock fabrics in ps7.

In the upper left of the model, the change in computed water saturation after 40 and 60 yr indicates cross flow of water from ps9 into ps7, thereby bypassing the injection front within ps7 and 8. As a result, an area of unswept mobile oil develops in the right part of the model, as shown by the computed water saturation distribution after 60 yr of waterflooding (fig. 43). Although the mudstone layers, representing the parasequence boundaries, are continuous in this area and permeability at 0.01 md is assumed to be very low, cross flow occurs (fig. 42).

The production characteristics of simulation EC-A and the other simulations (table 5) are shown in figure 44 (production rate), figure 45 (water cut), and figure 46 (cumulative production as percent of oil in place). Comparison of the production characteristics of the different simulations were used to evaluate various factors affecting reservoir-flow behavior.
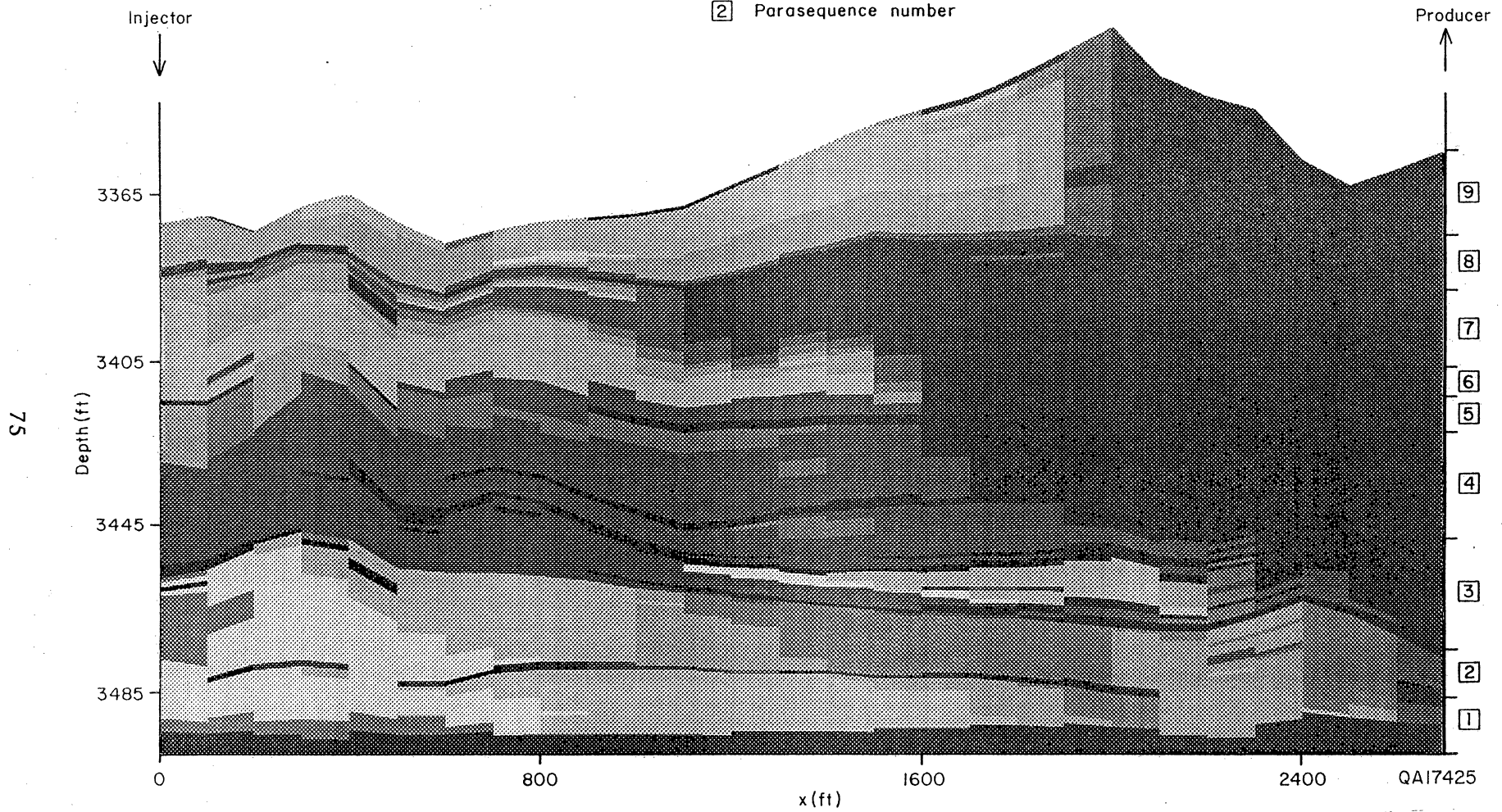
Figure 42. Computed changes in water saturation for simulation EC-A after waterflooding of (a) 20 yr, (b) 40 yr, and (c) 60 yr.

(b)

Change in water saturation (dS$_W$) at 40 years

0.0 - 0.1		0.1 - 0.2
0.2 - 0.3		0.3 - 0.4
0.4 - 0.5		0.5 - 0.61

2 Parasequence number
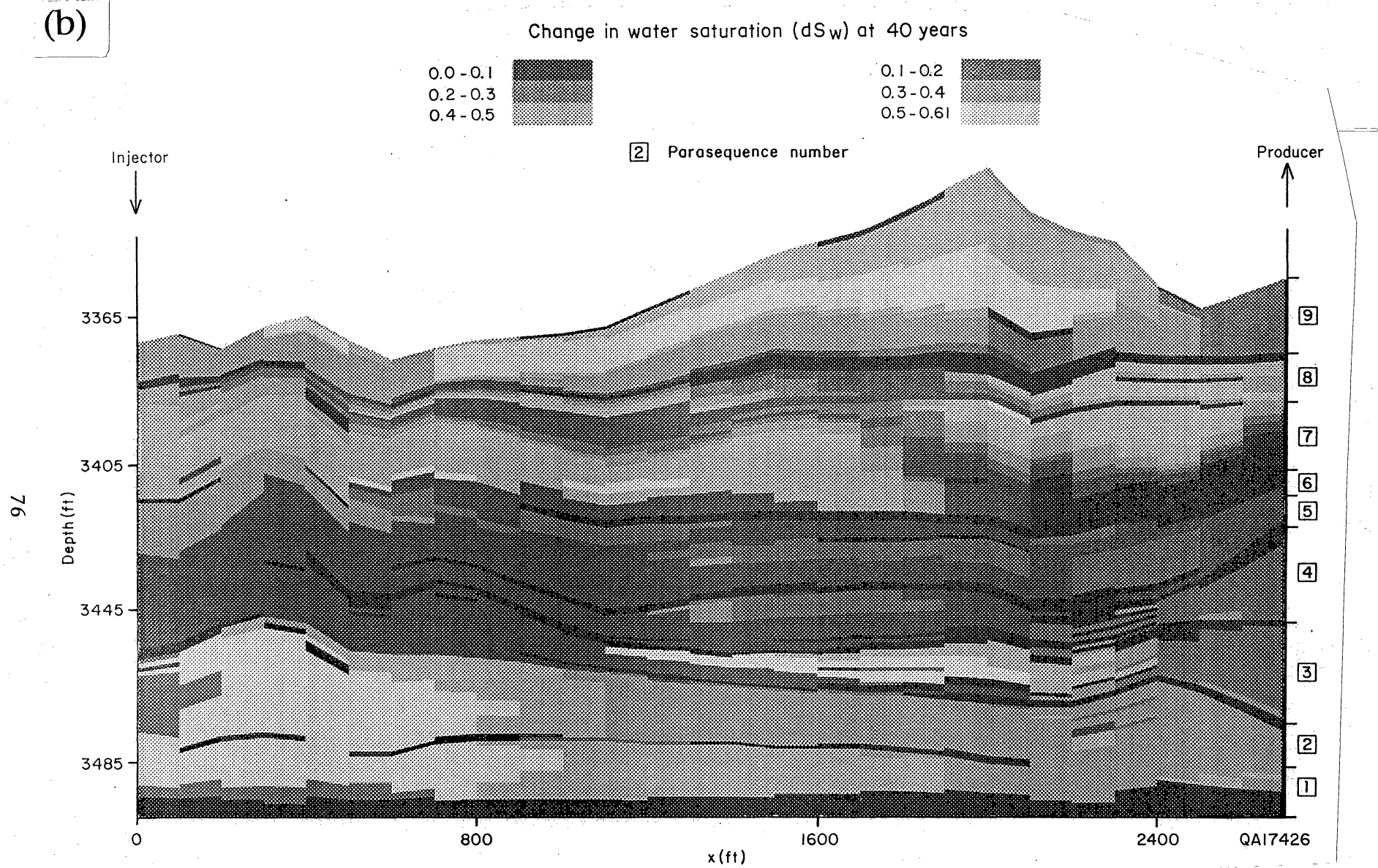
Figure 42. (cont.)

(c)

Change in water saturation (dS_W) at 60 years

0.0 - 0.1		0.1 - 0.2	
0.2 - 0.3		0.3 - 0.4	
0.4 - 0.5		0.5 - 0.63	

[2] Parasequence number
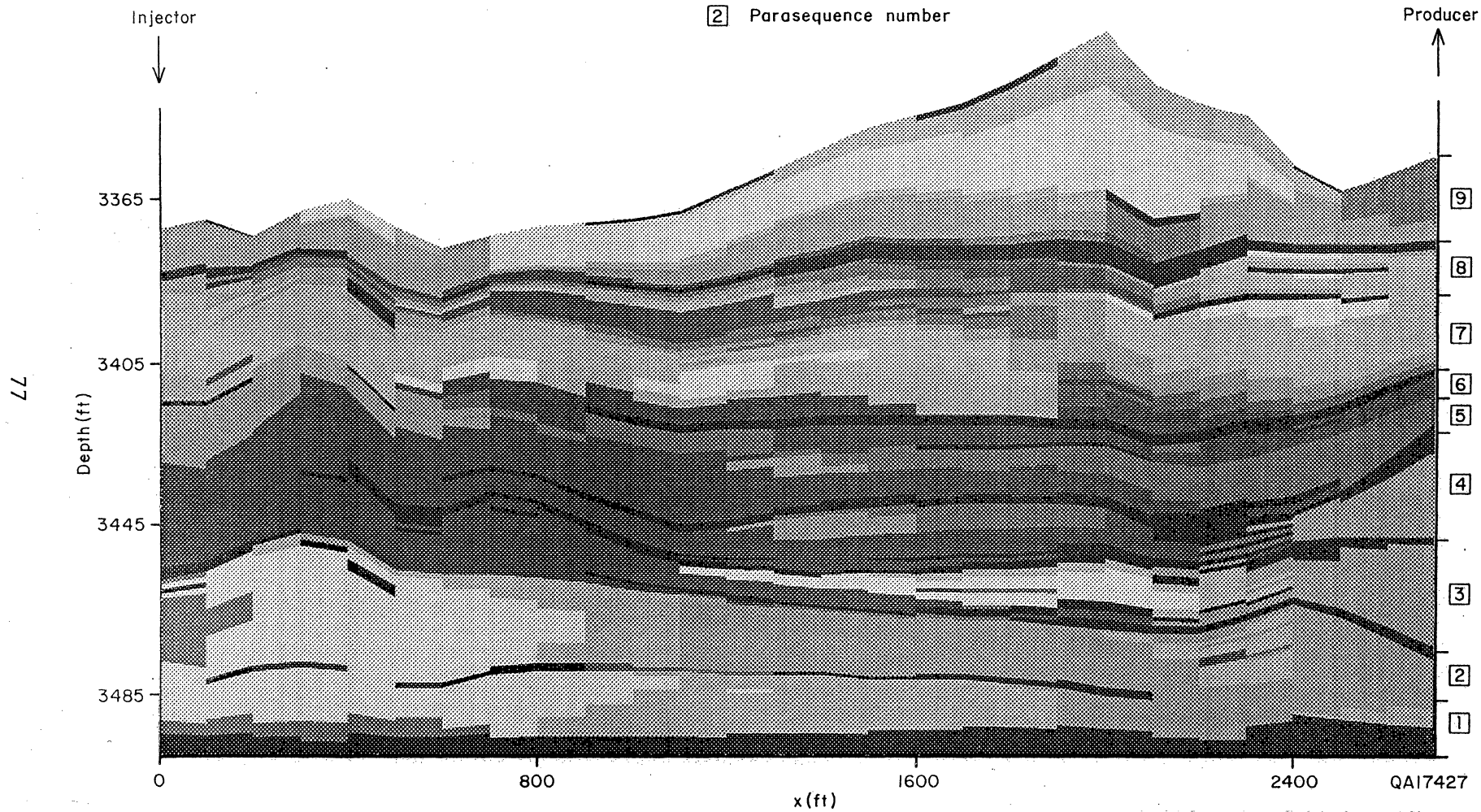
Figure 42. (cont.)
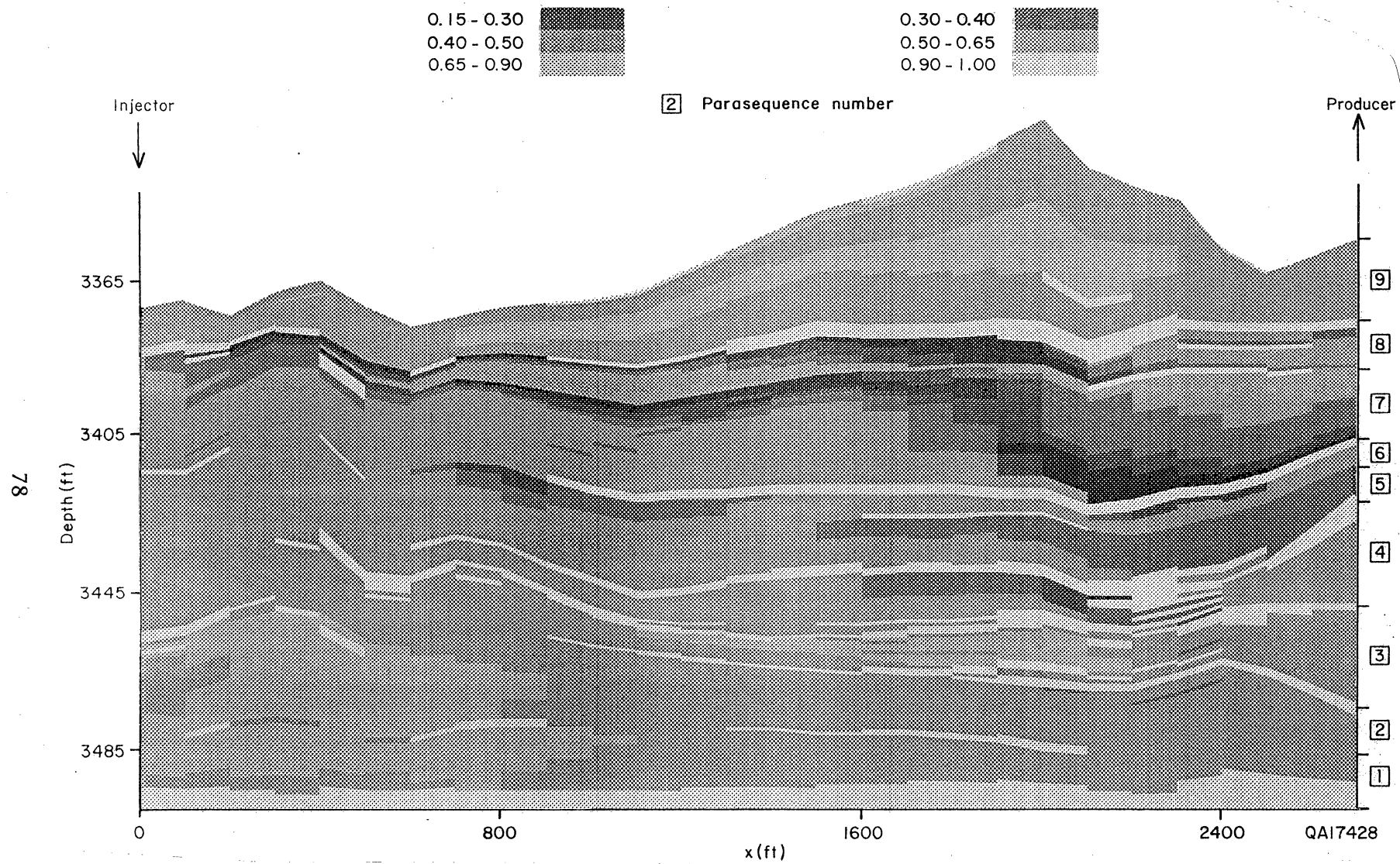
Figure 43. Computed water saturation for simulation EC-A after water injection of 60 yr.
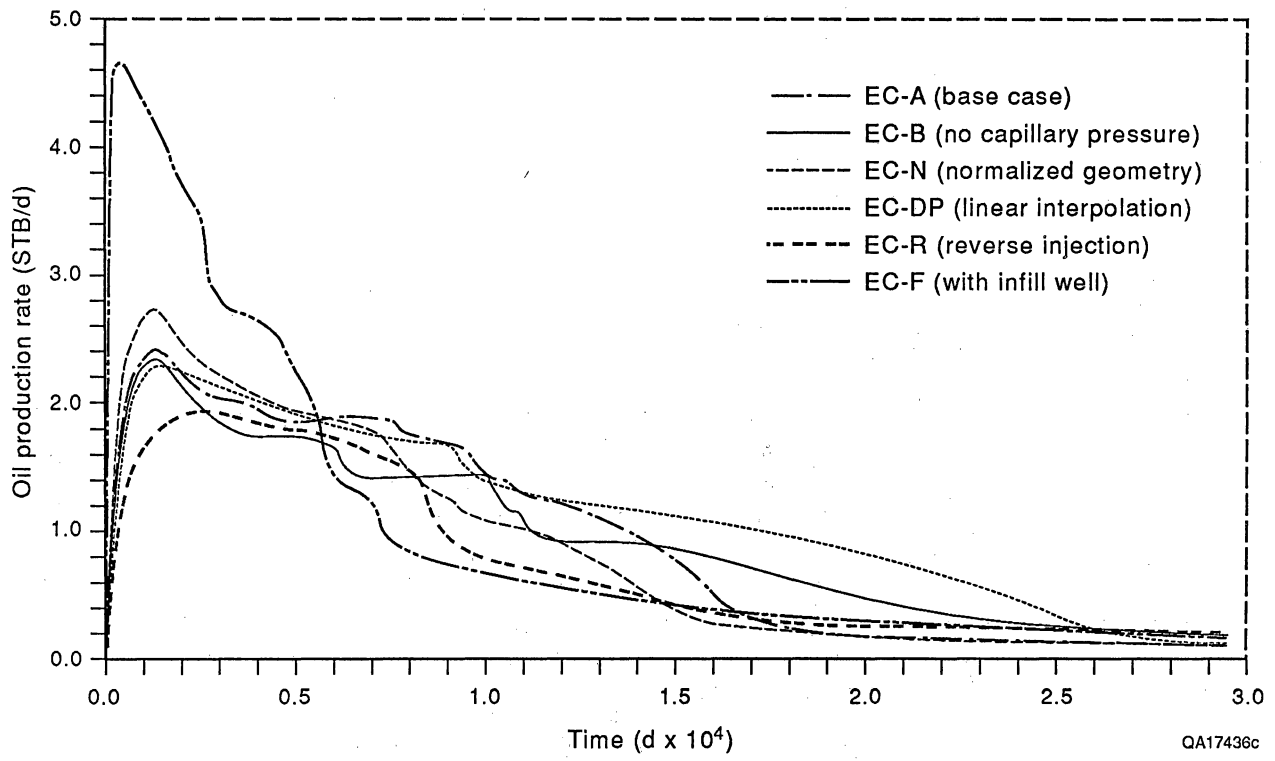
Figure 44. Oil-production rate versus time for simulations of the Lawyer Canyon outcrop model.
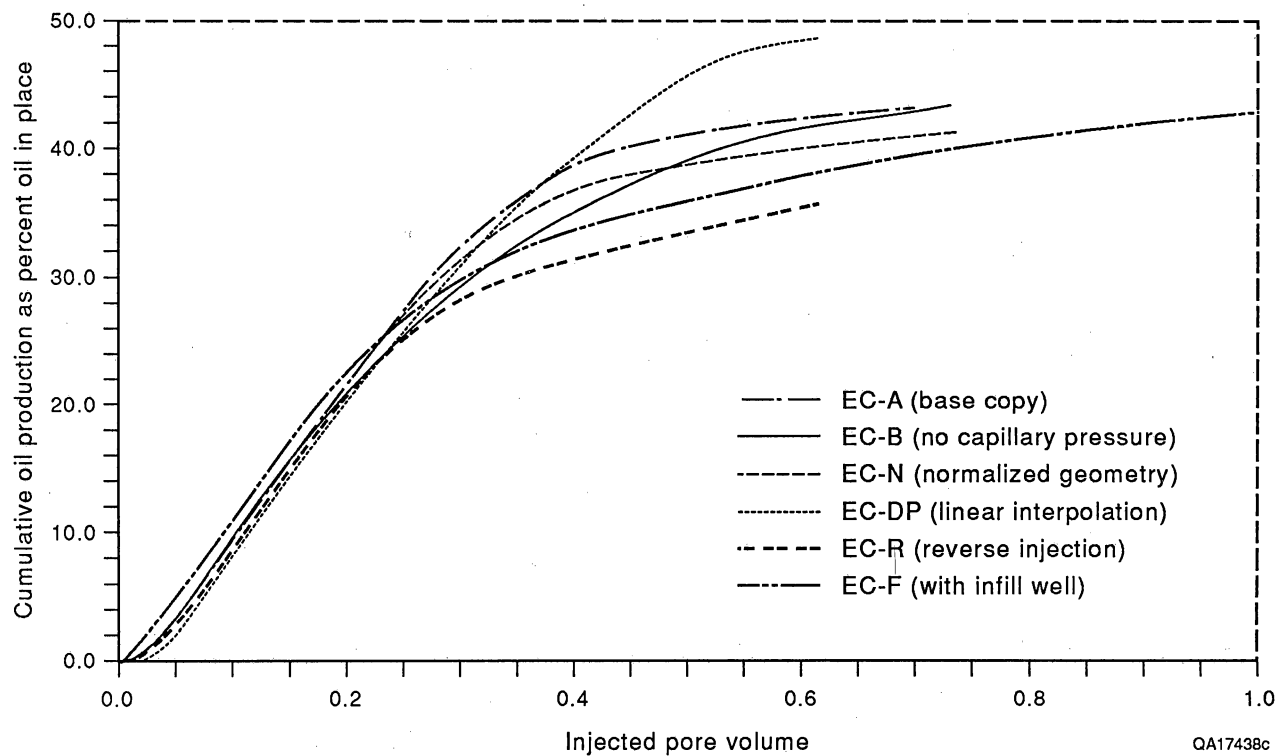
Figure 45. Water-oil ratio versus injected pore volume for simulations of the Lawyer Canyon outcrop model.
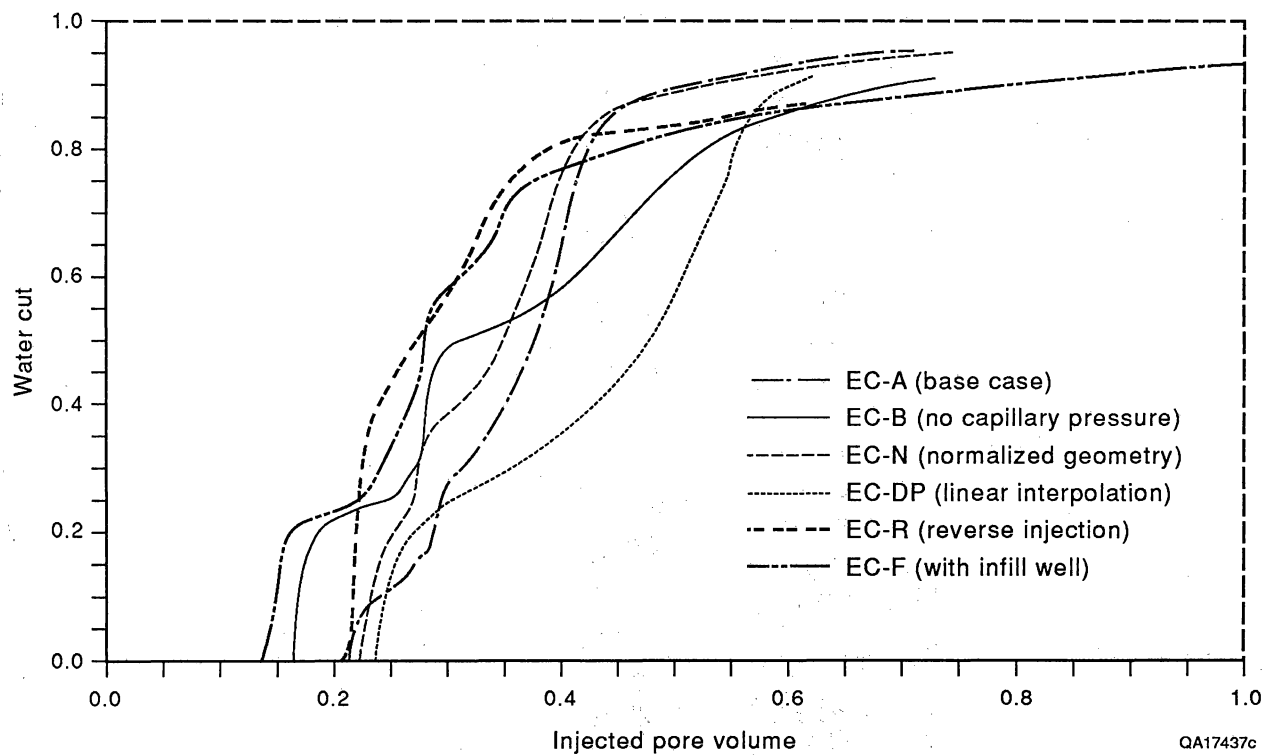
Figure 46. Cumulative oil production as percentage of original oil in place for simulations of the Lawyer Canyon outcrop model.

Effect of capillary pressure—In the first test, effects of capillary pressure were studied. Simulation EC-B does not incorporate capillary pressures (table 5). Production rates in simulation EC-B show a more stepwise decline with time, reflecting the flooding of the grainstone-dominated parasequences (fig. 44). Production rates are initially lower than those in simulation EC-A, which incorporates capillarity, but simulation EC-B maintains higher rates after 16,000 days. The stepwise decline in production rate is also reflected in the stepwise increase in water cut (fig. 45). Neglecting capillary pressures results in a lower sweep efficiency, as shown by the cumulative production curve (fig. 46). In simulation EC-A, capillary pressure improves sweep of the less permeable zones in ps3 through 6, whereas in simulation EC-B, waterflooding is restricted to the more permeable grainstone facies in ps1, 2, 7, and 9. Ultimate oil recovery of the two simulations, however, is the same (fig. 46).

Effect of model conceptualization—The effect of irregular formation geometry as compared with that of normalized formation geometry was evaluated in simulations EC-N and EC-DP (table 5). In simulation EC-N, the nine parasequences were normalized to a constant thickness, approximating the spatial distribution of the mapped facies (fig. 26). Production rates are initially higher than those in simulation EC-A, but they drop off more rapidly (fig. 44). The water-breakthrough curve for the normalized reservoir model (simulation EC-N) is steeper than that in simulation EC-A (fig. 45) and shows a lower recovery efficiency (fig. 46).

In simulation EC-DP, the reservoir model was constructed using the permeabilities of the individual flow units at the injection and production wells and then linearly interpolating permeability between wells using the normalized grid from simulation EC-N. This scenario represents a typical reservoir model constructed from well data where the facies and permeability distributions of the interwell area are unknown. When using well data from only the left and right sides of the outcrop model (fig. 26), the relatively permeable grainstone facies in ps9 is not incorporated into the layered model. Furthermore, in simulation EC-DP only a single relative-permeability curve and a single capillary-pressure curve are used.

Initial production rates in simulation EC-DP are similar to those in simulation EC-A but do not show the drop off after about 16,000 days (fig. 44), which is reflected in a less steep water-breakthrough curve than that in simulation EC-A (fig. 45). More importantly, sweep efficiency is overestimated in this layered model (fig. 46).

Effect of injection practice—Two additional flow scenarios were simulated to evaluate the effects of different injection schemes (table 3). In simulation EC-R, injection and production are reversed when the reservoir is flooded from the right side. Although the reservoir model and properties are the same in simulation EC-R and in EC-A, the production characteristics are noticeably different. Initial production rates in simulation EC-R are lower than those in simulation EC-A (fig. 44), but they remain slightly higher after 16,000 days. That is, at later times simulation EC-R produces at a lower water-oil ratio, which is characterized by the water-cut curve that levels out at a lower value than that of simulation EC-A (fig. 45). Sweep efficiency is significantly lower in simulation EC-R than in simulation EC-A (fig. 46), indicating that the spatial distribution of permeable grainstone facies relative to the direction of the waterflood (fig. 26) is important for the overall reservoir-flow behavior.

Comparing the change in water saturation after 40 yr of waterflooding shows a much larger area of unswept oil in the center of the model in simulation EC-R (fig. 47) than in simulation EC-A (fig. 42b). More importantly, cross flow occurs on the left side of the model toward the production well in simulation EC-R, from ps9 to ps1 and 2. Although in ps3 through 6 the less permeable wackestones on the left side of the model change to grain-dominated packstones on the right side, cross flow does not occur in simulation EC-A (fig. 42). On the other hand, cross flow across ps3 through 6 on the left side of the model is facilitated by the fact that the tight mudstone layers are discontinuous, whereas on the right side they are continuous (fig. 26). However, the spatial distribution of the higher-permeability grainstone facies on the left part of the model in ps1 and 2 (table 2, unit 10) and in ps9 (table 4, unit 11) are crucial for cross flow through ps3 through 6 on the left. As indicated in simulation EC-A
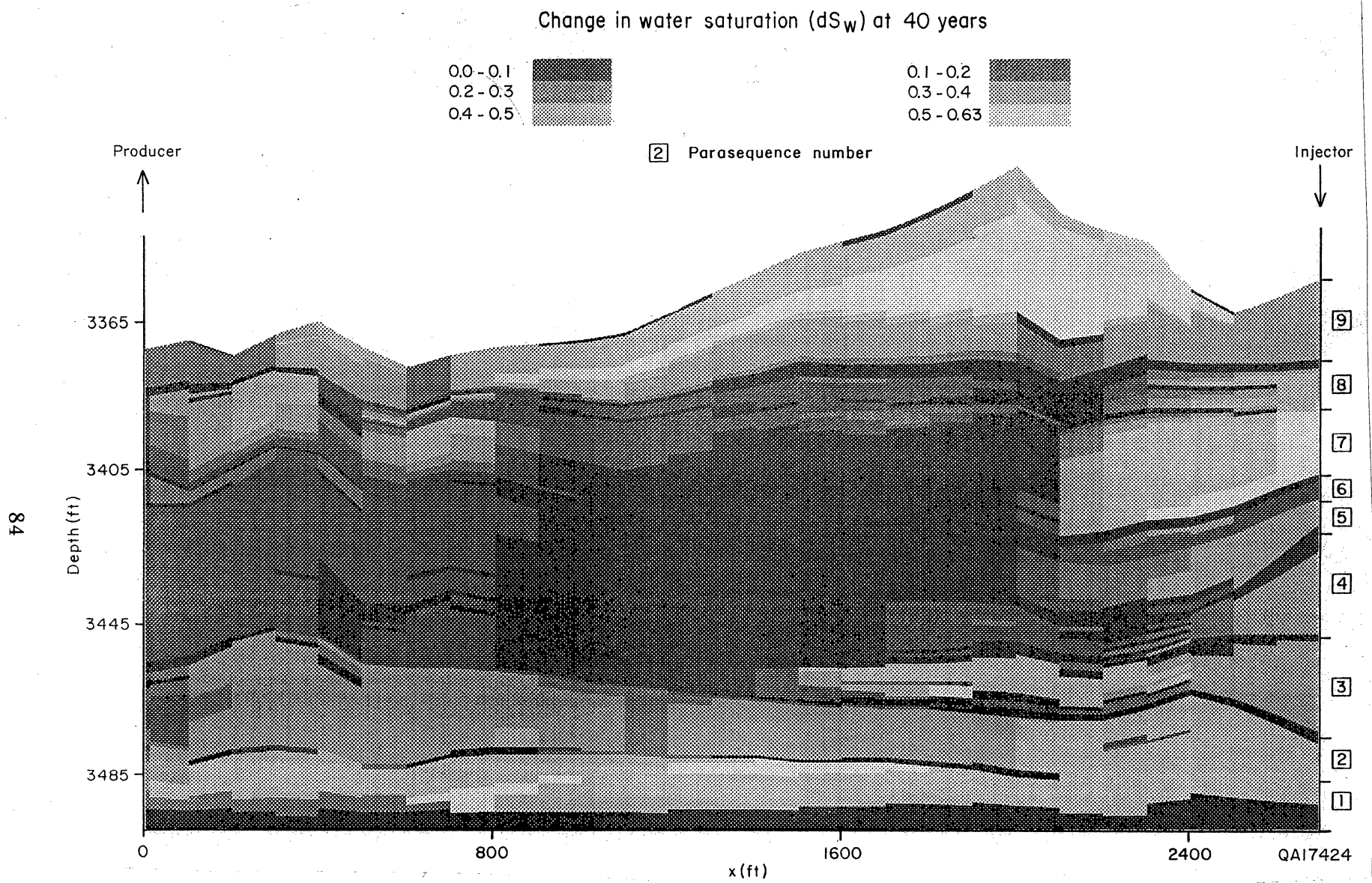
Figure 47. Computed changes in water saturation after 40 yr of waterflooding for simulation EC-R with inverse-injection pattern.

84

(fig. 43), continuous mudstone layers do not necessarily represent flow barriers, as shown by the cross flow between ps7 and 9 in the upper right of the model.

In the final simulation EC-F, the production well was located in the center of the model, and an injection well was placed at either side of the model. Prescribed pressures were adjusted in order to create the same pressure gradient between the injection wells and production well as those used in the other simulations. As one would expect, initial production rates are much higher in simulation EC-F than those in the other simulations but subsequently show a much earlier and steeper decline. However, after 16,000 days, the production rate levels off at a slightly higher rate than that in simulation EC-A. Similar to the reverse-injection pattern in simulation EC-R, the water-cut curve breaks at a lower water-oil ratio than that is simulation EC-A (fig. 45). The sweep efficiency of simulation EC-F is also lower than in simulation EC-A, but slightly higher than in simulation EC-R (fig. 46).

Irabarne Tank 1MSA1 Outer-Ramp Window

On the basis of regional geologic analysis, outcrops of the middle San Andres fusulinid-rich portion of the San Andres illustrate two end-member modes of geologic structure. In the interior of the San Andres platform the wackestone and packstone cycles dip eastward almost imperceptibly making reasonable the assumption of horizontal correlatability that is typically used in the subsurface (fig. 48). At Lawyer Canyon (see fig. 5), the section begins in cherty fusulinid wackestone just above the cherty mudstone facies. Sections are weakly cyclic between moldic fusulinid wackestone/packstone and fusulinid peloid packstone in the basal 200 ft, becoming distinctively cyclic in the upper 80 ft (fig. 49). The 280-ft section was subdivided into 15 parasequences from 12 to 40 ft in thickness, with individual parasequences displaying a constant thickness across the 1,800-ft width of the mapped area. The lower parasequences are thicker (20 to 40 ft) and consist of cherty fusulinid wackestone to fusulinid-crinoid-peloid packstone. The upper four parasequences are thinner (15 to 20 ft) and have distinctive

Platform interior correlation

1300 ft

200 ft

Ramp crest grainstone facies

Outer ramp clinoform facies

Platform margin correlation

1300 ft

Sequence boundary

500 ft

0   1   2 mi

0   3 km

Sequence boundary

HIGHSTAND SYSTEMS TRACT

Inner-ramp algal wackestone

Ramp-crest peloid-ooid packstone/grainstone

Outer-ramp clinoform fusulinid/ pelloid/crinoid wackestone/ packstone/grainstone

Outer-ramp clinoform toe mudstone (transitional)

TRANSGRESSIVE SYSTEMS TRACT

Outer-ramp clinoform toe mudstone (transitional)

Ooid grainstone

Fusulinid wackestone/ packstone

LOWSTAND TRACT
(laterally transposed)

Silty/sandy dolostone

QA13494c

Figure 48. Conceptual carbonate ramp model showing the gross changes in cycle geometry between the platform interior and the platform margin setting in the outer ramp clinoform facies. Interwell correlation of cycles in the platform interior may be approximately horizontal, whereas in the platform margin setting interwell correlation of cycles requires incorporation of a depositional dip to accurately represent geologic structure.
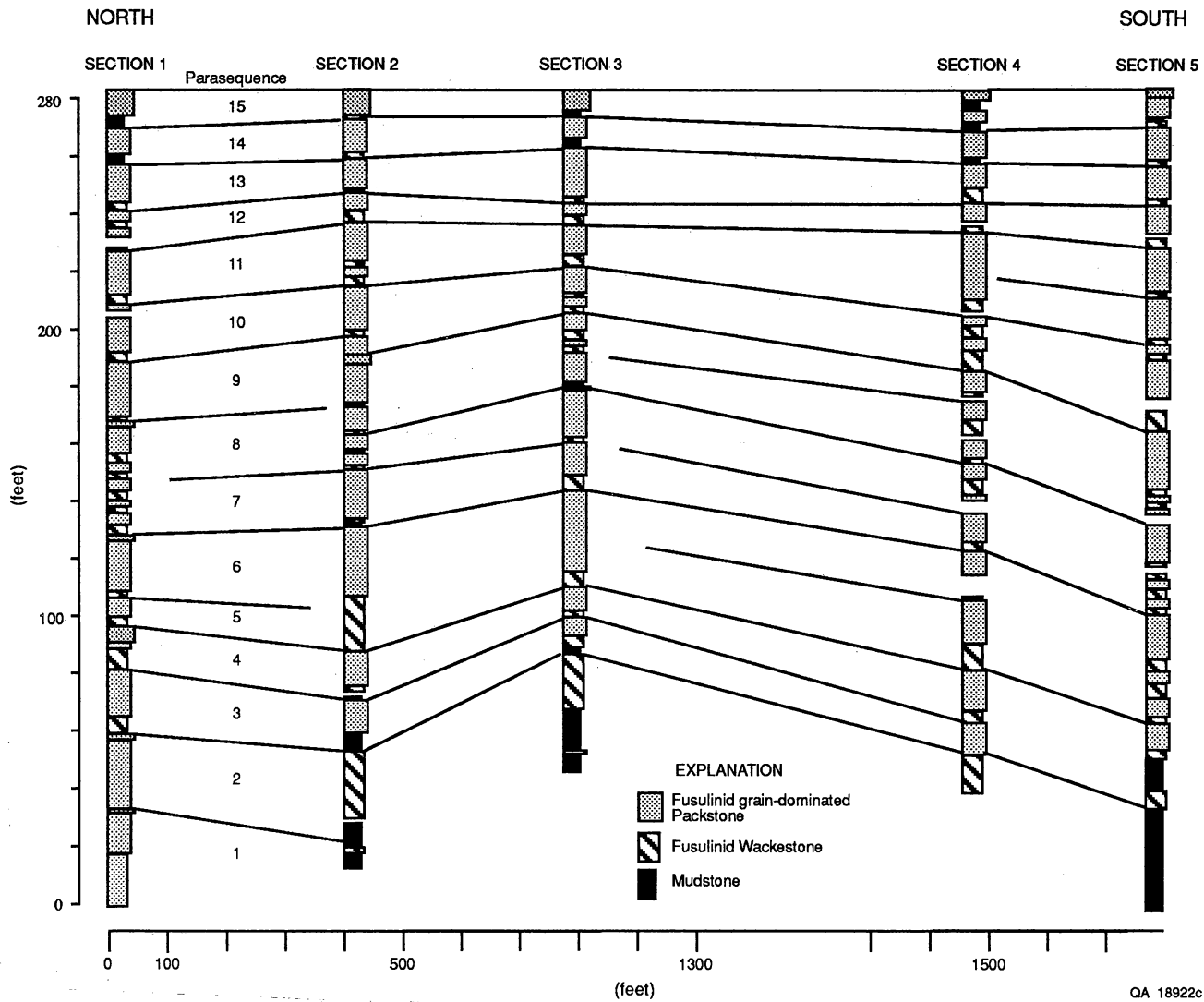
Figure 49. Cross section of middle San Andres parasequence window at Lawyer Canyon showing showing 15 cycles from mudstone through fusulinid wackestone to fusulinid grain-dominated packstone.

mudstone bases followed by fusulinid wackestone/packstone and fusulinid-crinoid-peloid packstone-grainstone caps.

Within these upper two to three parasequences, Hindrichs performed his pioneering studies of permeability distribution at Lawyer Canyon (Hindrichs and others, 1986). His work indicated that the mudstones are tight (k = 0.01md) and the fusulinid wackestone/packstone/ grainstones are permeable (k = 5 md). The permeability varies on a scale of inches with little change in the permeability structure over 1,320 ft laterally.

Farther basinward in a platform margin position the cyclic fusulinid strata are in the form of clinoforms that display depositional dips ranging from 2° to as great as 17° (fig. 48). These platform-margin clinoforms were selected for detailed reservoir-modeling studies. The key issue is to test the effect of inclined flow-units on interwell communication by building flow simulation experiments. The approaches were to describe the geologic model by mapping the vertical and lateral distribution of rock-fabric facies and to quantify the geologic model by collecting petrophysical data from the geologic framework.

Geologic Framework

The Irabarne Tank outer-ramp window is located 12 miles downdip of the Lawyer Canyon Window and largely within the uSA2 sequence (fig. 4). Excellent two- and three-dimensional exposures of these cyclic outer ramp strata are exposed along east-west trending canyon walls at Irabarne Tank (fig. 50) and show the typical inclined clinoform geometry for this facies tract (fig. 51). Average depositional dip for the outer ramp clinoforms at Irabarne Tank is only 1°–2°, but even this slight dip is apparent in figure 51 when comparing the dip of the originally flat-lying ramp-crest grainstone strata with the outer ramp deposits that were deposited on a gradual slope into the basin to the southeast. In a reservoir setting, dips of 2° are sufficient to offset correlation of flow units by 23 ft in wells with lateral separations of 660 ft.
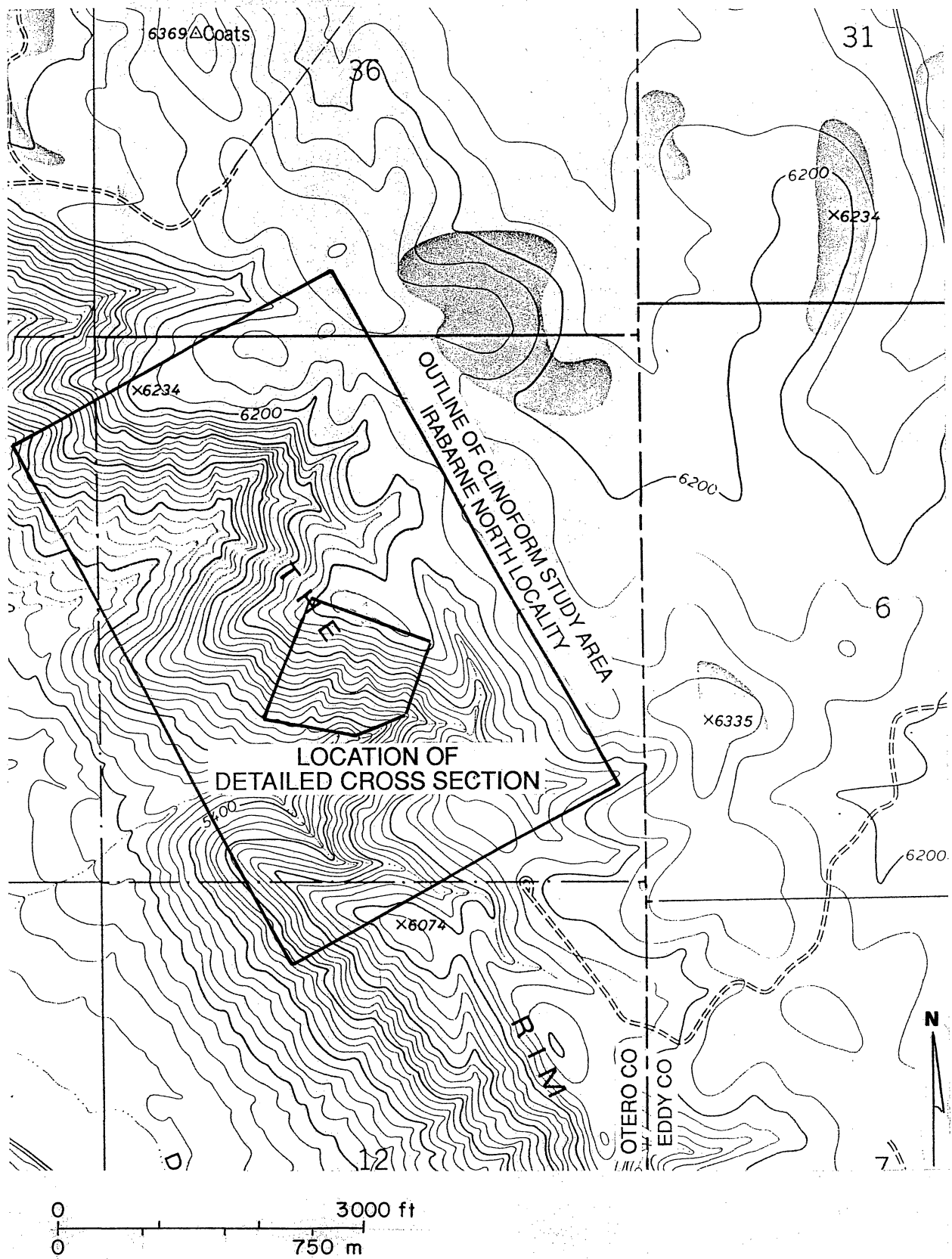
Figure 50. Topographic map showing the Irabarne Tank study area in Section 1, T25S R20E of the Picket Hill 7.5 minute topographic sheet, New Mexico, and the location of the Irabarne Tank Canyon detailed cross section. Contour interval is 200 ft.

NW

SE

Grayburg Fm

Inner Ramp

Recent

Ramp Crest

Gravity

Drainage

Drainage

Slide

Outer Ramp Clinoforms

Scree

0   200 ft
├───┴───┤
0   50 m

Scree

Distal Outer Ramp
Clinoform Toes
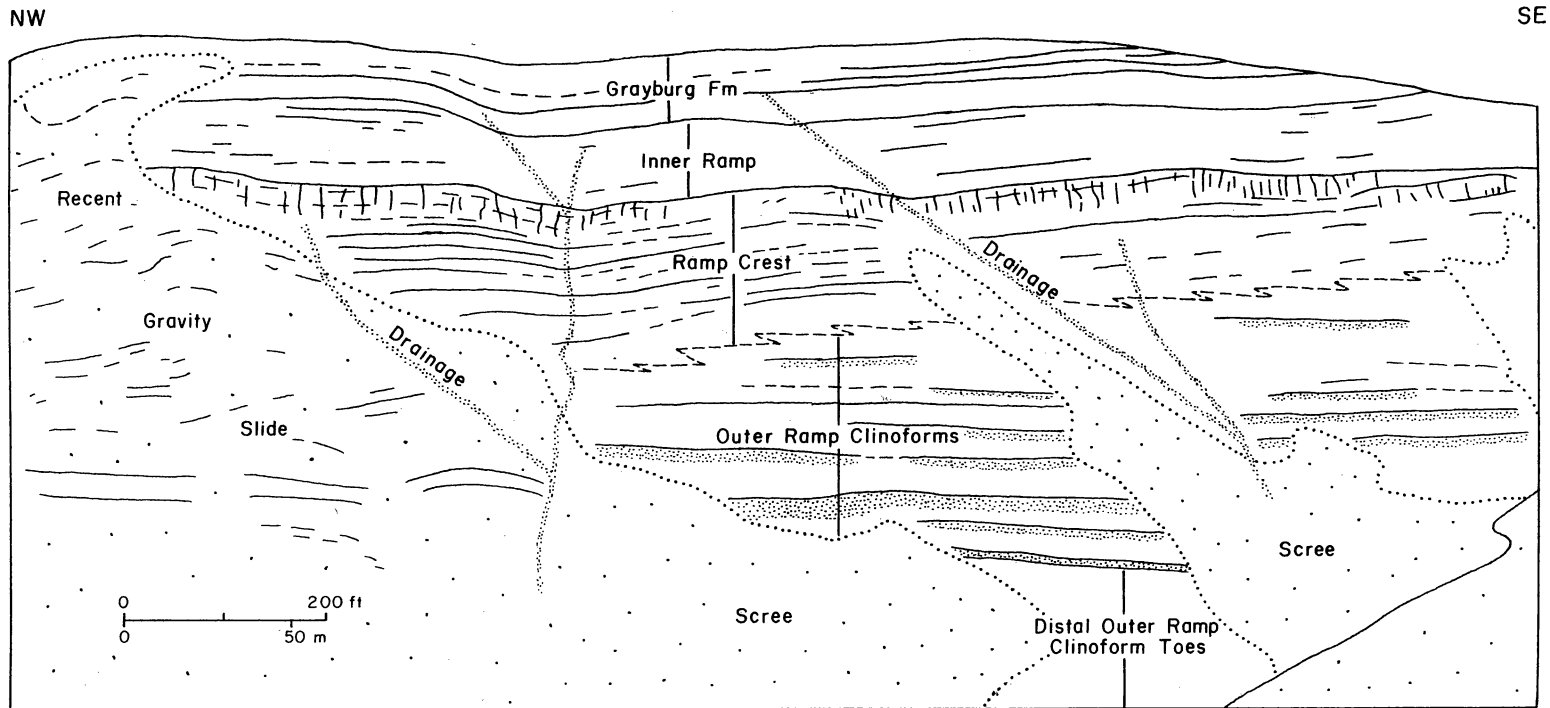
QA 13497

Figure 51. Tracing of photomosaic of San Andres platform margin at Irabarne Tank Canyon study area. Note the change in dip attitude between the ramp-crest beds and outer-ramp clinoforms. Individual upward coarsening cycles in the outer ramp are shown by white (wackestone) to stippled (grain-dominated packstone) layers.

Four detailed geologic sections were measured at 200 ft sampling distances along one east-west trending canyon wall (fig. 52). Each section covered 100–120 ft of vertical section and contained 10 clinoform depositional cycles. In general, depositional cycles in the clinoforms are upward-coarsening cycles grading from moldic fusulinid-peloid wackestone to nonmoldic and mixed moldic/nonmoldic fusulinid-peloid-crinoid packstone/grainstone. A mudstone bed defines the base of cycle 5 (fig. 52). Overlying the clinoform section is a 30 ft brachiopod-sponge-crinoid bioherm with flanking horizontally bedded peloid and crinoid-fusulinid packstone/grainstone facies. A 35-ft-thick level-bedded ooid-grainstone unit overlies the study window.

Thin-section examination shows that the cycles are composed mainly of packstones and wackestones with only a few grainstones. The fabrics consist of very large grains (500–1,000 μm) and intergranular lime mud recrystallized to a dolomite characterized by 50-μm dolomite crystals. Most of the grains are unidentifiable peloids but large echinoderm and fusulinid grains are common and dasycladacean and gastropod fragments are sparse. Fusulinids have been selectively dissolved in the mud-dominated textures and tend to be well preserved or crushed in grain-dominated textures. There is ample suggestion that the rocks once contained anhydrite which has been completely dissolved.

Petrophysics of Outcrop Samples

The outcrop was sampled for porosity and permeability using a hand-held core drill. Two sampling localities (localities A and B, fig. 52) were selected located about 500 ft apart laterally and in overlapping cycles 2, 3, 4, and 5. 105 permeability plugs were collected from the two sampling locations (fig. 53). The condition of the outcrop at locality A did not allow evenly spaced sample locations and core plugs could not be obtained at some sample locations due to weathering conditions.
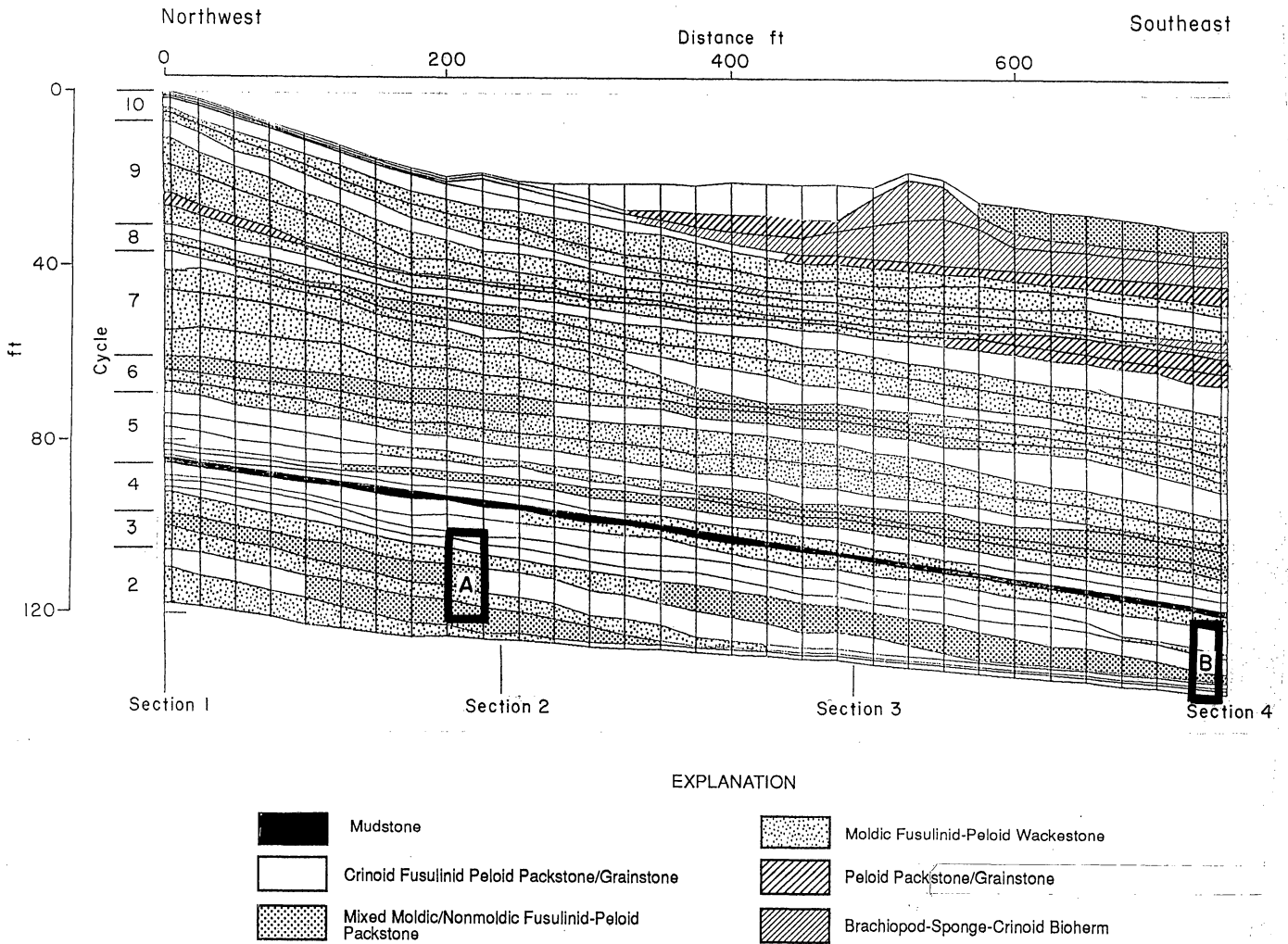
Figure 52. Geologic cross section of the north wall of Irabarne Tank Canyon (see fig. 50) showing the facies framework and the location of the core-plug sample grids. The simulation grid overlies the facies framework.
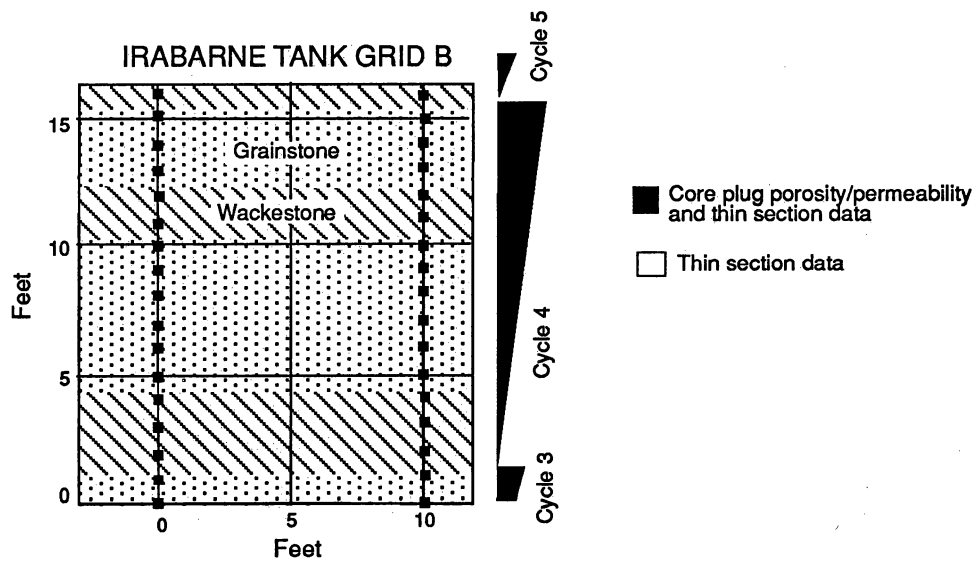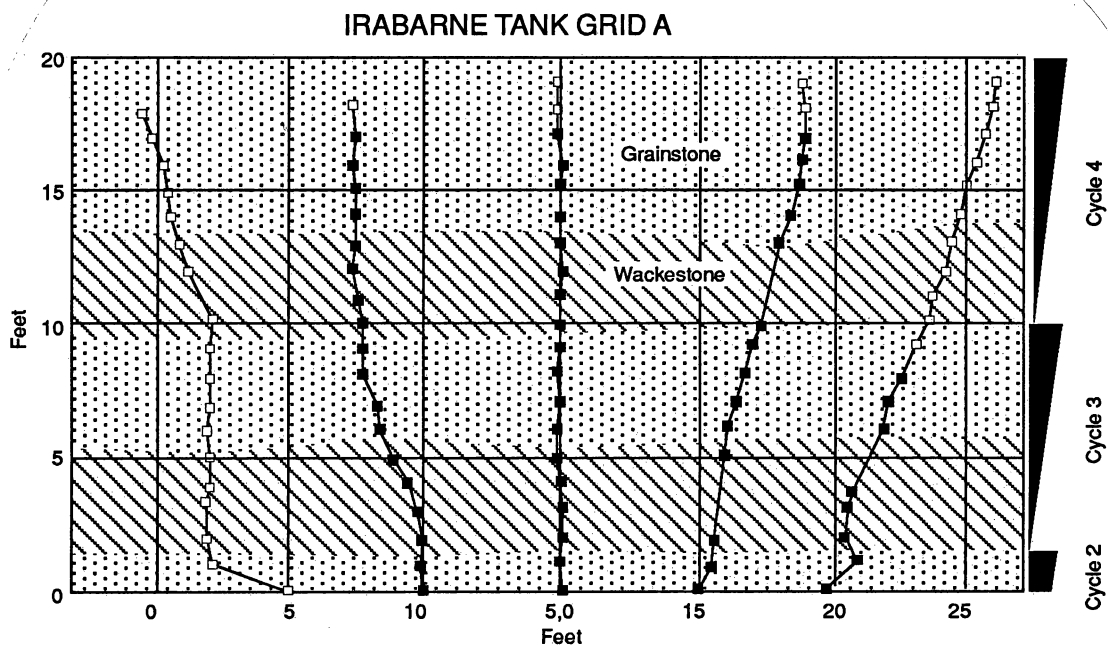
Figure 53. Sampling grids for core plugs at Irabarne Tank Canyon (see fig. 52). Lithology is based on outcrop descriptions. Lithology in figure 54 is based on thin-section descriptions.

At *locality A*, 57 samples were collected on a grid pattern 20 ft wide by 17 ft high with 4 vertical transects sampled at 1 ft vertical increments when possible (fig. 53). The samples are spread across parts of depositional cycles 2, 3, and 4. At *locality B*, 34 samples were collected from two 16 ft vertical sections spaced 10 ft apart and sampled at 1 ft vertical increments over cycles 3, 4, and 5 (fig. 53).

Thin-section descriptions show the presence of grainstones, grain-dominated packstones, and mud-dominated packstones and wackestones and the distribution of these rock fabrics is shown in figure 54. The cross sections in figure 54 show that, in general, the cycles change vertically from mud-dominated packstone and wackestone to grain-dominated packstone. However, there is some lateral variability to this generalization.

Total porosity of the core plugs was measured and is mapped in figure 55. The cross section in figure 55 shows that the porosity zones tend to be horizontal but with lateral variability. Separate-vug porosity, composed primarily of fusulinid molds, was measured by thin-section point counts and is mapped in figure 56. The highest separate-vug porosity tends to be associated with the mud-dominated fabrics and the high values of total porosity.

Zones of high vuggy porosity are preferentially weathered and form the bedding visible on the outcrop. Microscopic examination shows that much of the vuggy porosity is due to the removal of anhydrite or gypsum and that the vugs tend to be connected by microfractures probably resulting from stress fields associated with the outcrop. The microfracturing results in a touching-vug system on the scale of the core plug. Thus, the permeability map presented in figure 57 shows the highest permeabilities associated with zones of highest separate-vug porosity due to the touching-vug nature of the pore system.

To test the association of the microfractures with the outcrop and to obtain realistic permeability values for the vuggy rock fabric, a 60 ft interval of fusulinid rock from the middle San Andres core from Algerita No. 3 well was studied (fig. 11). Algerita No. 3 is one of three wells drilled and cored 1,000 ft back from the outcrop at Lawyer Canyon and spaced 330 ft apart. Core slabs and thin sections show this interval to have textures and fabrics similar to the

Figure 54. Rock fabric distribution in sampling grids A and B, Irabarne Tank Canyon Window based on thin-section descriptions.
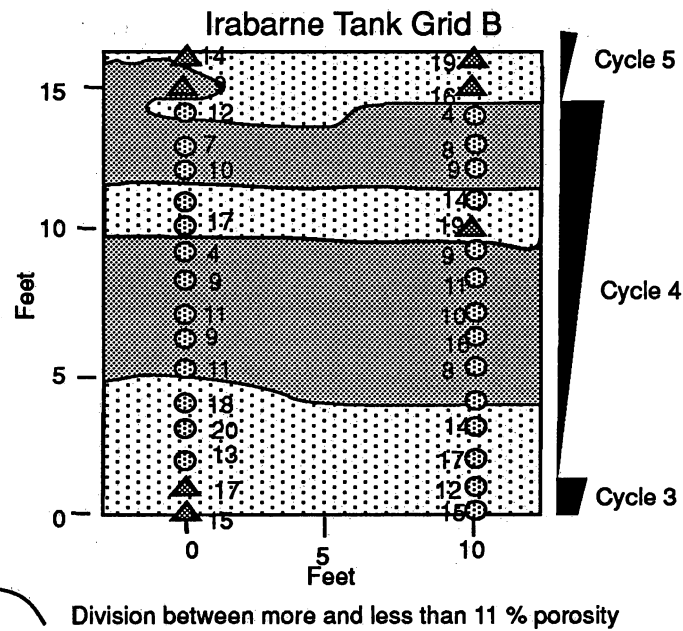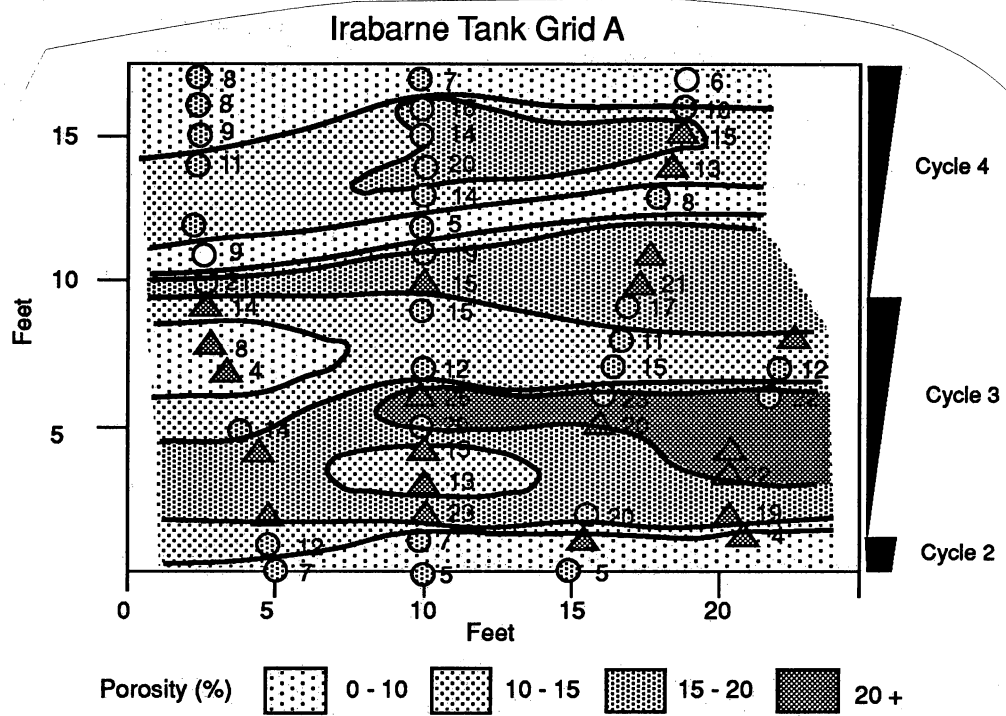
Figure 55. Porosity distribution in sampling grids A and B, Irabarne Tank Canyon Window.
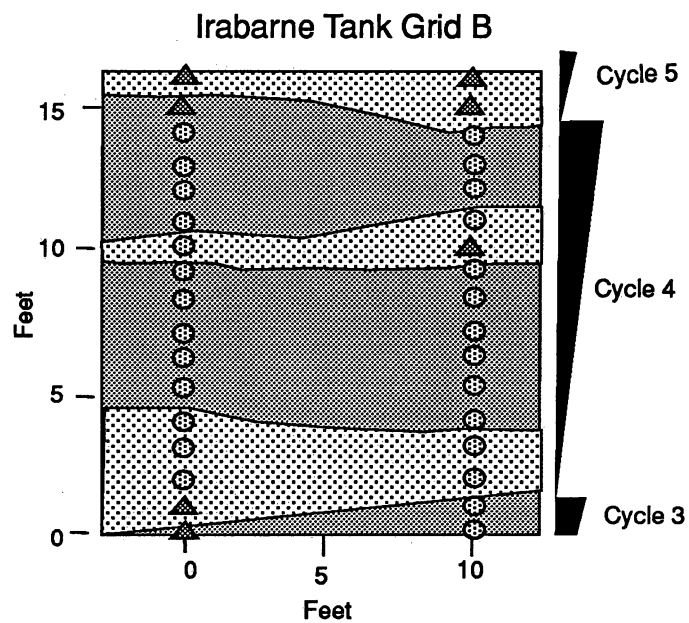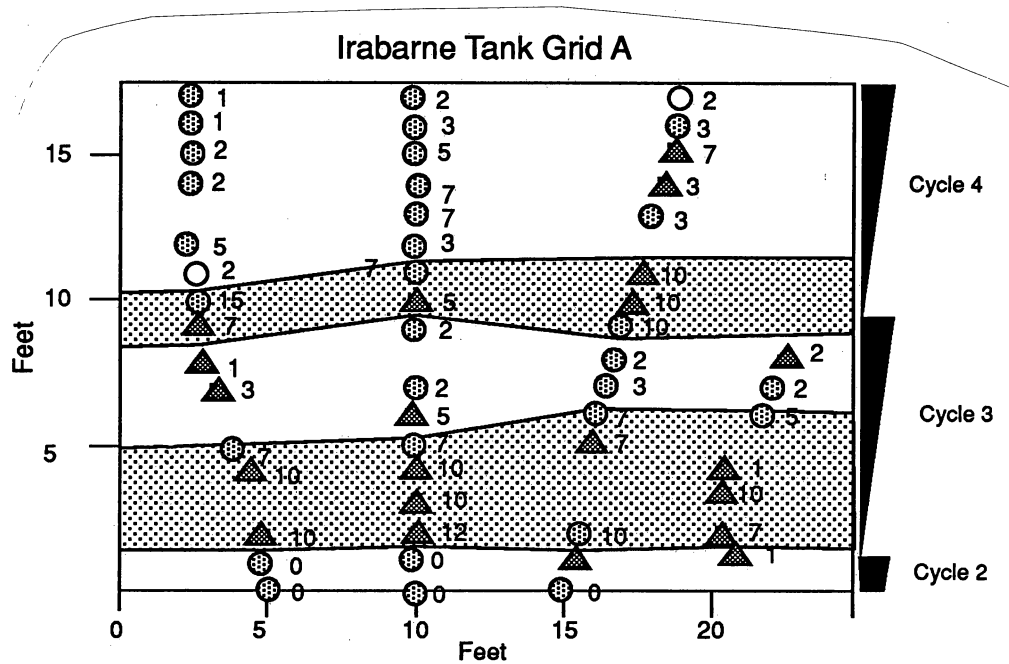
Figure 56. Separate vug distribution in sampling grids A and B, Irabarne Tank Canyon Window. Separate vugs are primarily molds of fusulinids.
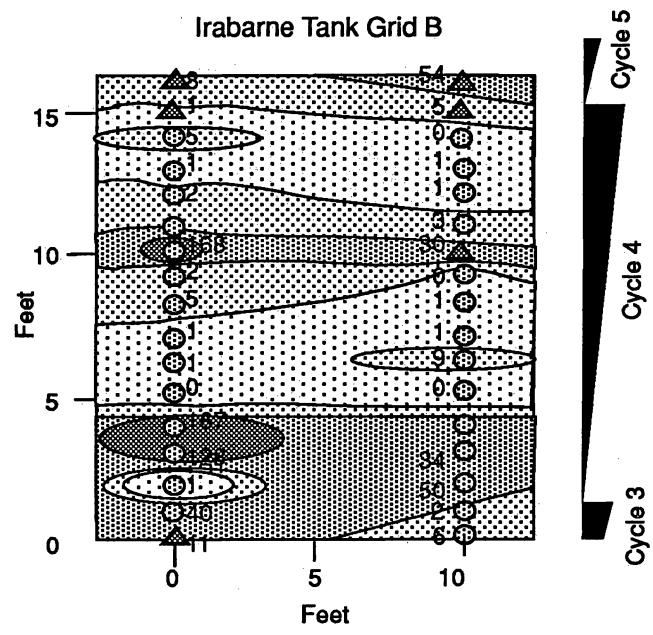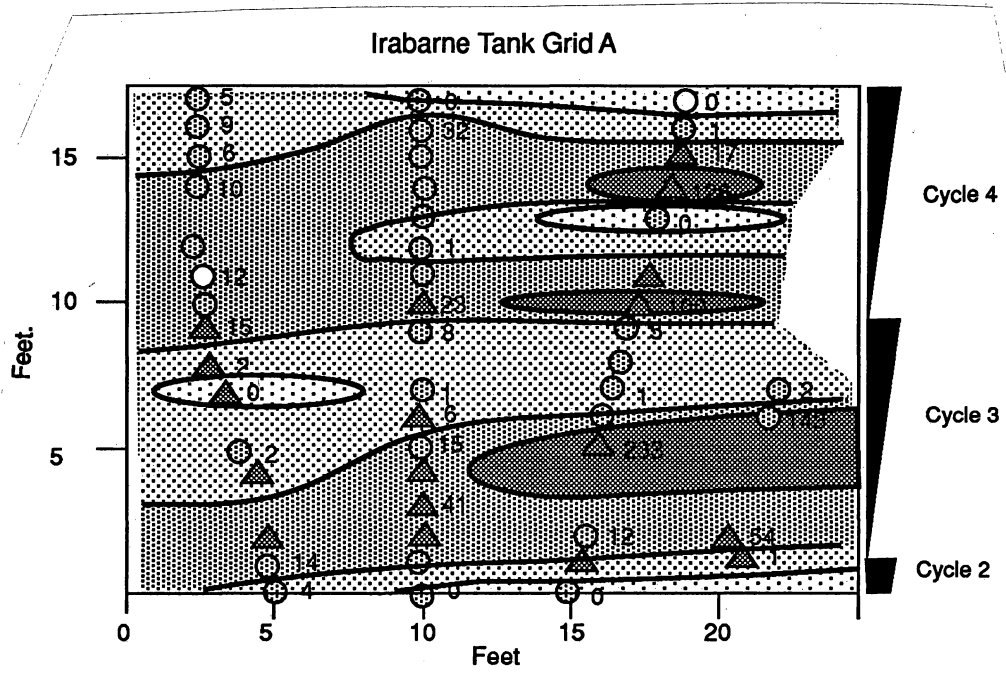
Figure 57. Permeability distribution in sampling grids A and B, Irabarne Tank Canyon Window.

samples from the Irabarne Tank outcrop and to have beds with moldic porosity and beds without moldic porosity.

Permeability was measured using an MFP; in addition, permeability and porosity were determined on 1-inch core plugs and on whole cores. MFP measurements were taken every 2 inches over the 60-ft interval from 461 to 520 ft, resulting in 360 measurements. Part of the core shows the presence of cavernous porosity forming a touching-vug system. The core permeabilities were very high in the presence of the cavernous pore system and did not compare well with the MFP permeabilities. Where the cavernous pore system was absent, however, the MFP and core data were similar. Therefore, the MFP data was concluded to be characteristic of the matrix permeability.

Arithmetic-mean porosity and permeability values for core and outcrop data are shown in table 6. The average values for the samples with low-moldic porosity (3 percent or less) are similar. For high-moldic porosity, the values are similar but the permeability of the outcrop samples is 43 md, whereas the value for the core samples is only 6 md. This difference in permeability supports the conclusion that leaching and fracturing associated with the outcrop has produced a significant microfracture pore system enhancing the permeability of the highly moldic fabrics.

Rock-fabric analyses of the porosity and permeability data from Irabarne Tank and Algerita 3 samples indicate that permeability is a function of grain size as well as sorting and interparticle porosity (fig. 58). The grain-dominated packstones are divided into two groups based on grain size—500- and 1,000-μm grains. The 500-μm grain size plots within petrophysical class 2 of figure 8 as expected, but the 1,000-μm grain size plots in class 1 rather than in class 2. This is due to larger intergranular pore sizes associated with the larger grain size and suggests a particle-size limit of about 500 μm for the rock-fabric petrophysical relationships shown in figures 8 and 9.

A few samples characterized by wackestone fabric are plotted on figure 58. Mud-dominated wackestone fabrics should normally plot in the Class 3 field but here they plot in

Table 6. Comparison of arithmetic-mean porosity and permeability data from Algerita 3 core and outcrop.

	Low Moldic		High Moldic	
	ϕ (%)	k (md)	ϕ (%)	k (md)
Core	11	3	18	6
Outcrop	10	8	18	43

ALGERITA 3 & IRABARNE TANK
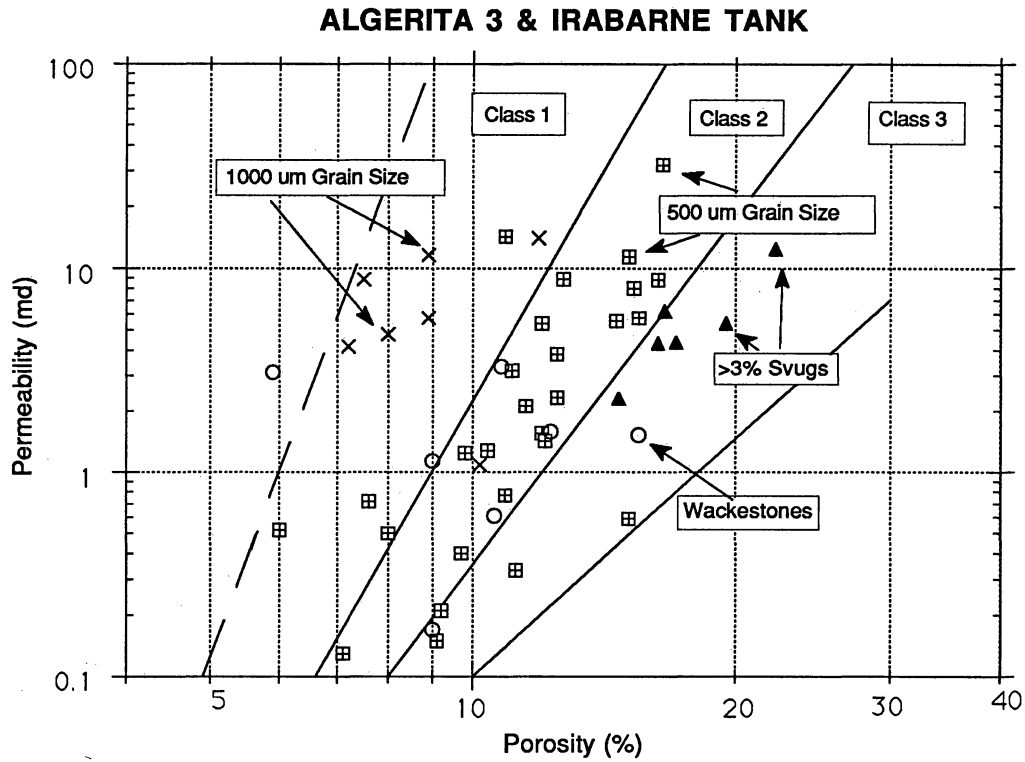
Figure 58. Porosity/permeability plot of core-plug data from Irabarne Tank Canyon grids and part of the core from Algerita No. 3 well. The plot shows that both the nonvuggy grain-dominated packstones and mud-dominated wackestones with 50-μm dolomite crystals plot in Class 2 while samples with very large particles plot and class 1 and samples with separate vugs plot in class 3.

class 2 along with grain-dominated packstones. This fact is due to the replacement of the fine-particle-size lime mud with 50-μm dolomite crystals resulting in an interparticle pore size increase.

The few samples with >3 percent separate-vug porosity plotted in figure 58 are from the Algerita 3 core. The samples show that, in the absence of touching-vug pore geometries (microfractures and cavernous pores), the addition of vugs does not increase permeability.

Geostatistical analysis

Because of the presence of microfractures in the highly vuggy samples, only data from the upper, nonvuggy packstone fabric of cycle 4 was statistically analyzed. The arithmetic-mean porosity and permeability of 17 samples from upper cycle 4, grid A are 11.35 percent and 20.33 md. The arithmetic-mean porosity and permeability of 14 samples from upper cycle 4, grid B, are 9.2 percent and 0.83 md, respectively. The results of an analysis of the permeability values using a two-sample Koimogorov-Smirhov test indicates that the null hypotheses can be rejected implying that the permeability data for the two grids represent different populations at the 5 percent confidence level. The statistically different permeability distributions of the individual grids located 500 ft apart suggests a long-range spatial correlation of nested structures on a scale 100's of ft similar to that observed in ps1 at Lawyer Canyon.

In order to characterize the vertical spatial distribution of permeability in the fusulinid cycles, a geostatistical analysis of the MFP data from Algerita No. 3 was made. Spatial permeability patterns in the core were determined using variogram analysis (Journel and Huijbregts, 1978). Spatial permeability characteristics can be described by the nugget, the correlation range, the sill, and the variogram model. The latter is obtained by fitting a certain type of mathematical function to the experimental variogram. In this study the computer package GEOPACK (Yates and Yates, 1990) was used to compute the experimental variogram.

The variogram, constructed from permeability data obtained from MFP measurements on the core from the Algerita No. 3 well, indicates a correlation range of 1.6 ft, a nugget of 0.057 md^2, and a sill of 0.10 md^2, based on a spherical variogram model (fig. 59). The variogram results are similar to those from outcrop measurements in the Upper San Andres parasequences at Lawyer Canyon. Permeability is characterized by local random heterogeneity (nugget effect) and by a relatively small correlation range of permeability in the vertical direction.

Waterflood Simulation of Upper Cycle 4

The results from the Lawyer Canyon study suggested that facies-averaged petrophysical data can be used for input into numerical reservoir simulators because of the near-random permeability patterns within a rock-fabric facies. Permeabilities for upper cycle 4 of Irabarne Tank are assumed to have a small correlation range in the vertical direction with local random variability based on the measured data from Algerita 3 core. Spatial permeability correlation in the horizontal direction is assumed to be characterized by a long-range correlation of nested structures on a scale of 100's of ft, based on the different mean permeability of the two outcrop measurement grids spaced 500 ft apart.

Three methods of characterizing the permeability distribution were evaluated using a reservoir simulator. A simple model of upper cycle 4 was generated consisting of a 20- by 500-ft grid composed of 2,000 blocks measuring 0.5 by 10 ft. Three experiments were run using (1) a facies-averaged geometric-mean permeability of 1.35 md, (2) permeability values interpolated between the geometric-mean values of grids A and B, and (3) a conditional simulation of permeability incorporating the vertical variogram model from the analysis of the Algerita No. 3 data and assuming a horizontal variogram model with a range of 150 ft, a nugget of 0.57 md^2, and a sill of 0.10 (fig. 60). Saturation, capillary pressure, and relative permeability curves were derived using methods outlined in the section on Lawyer Canyon simulation.
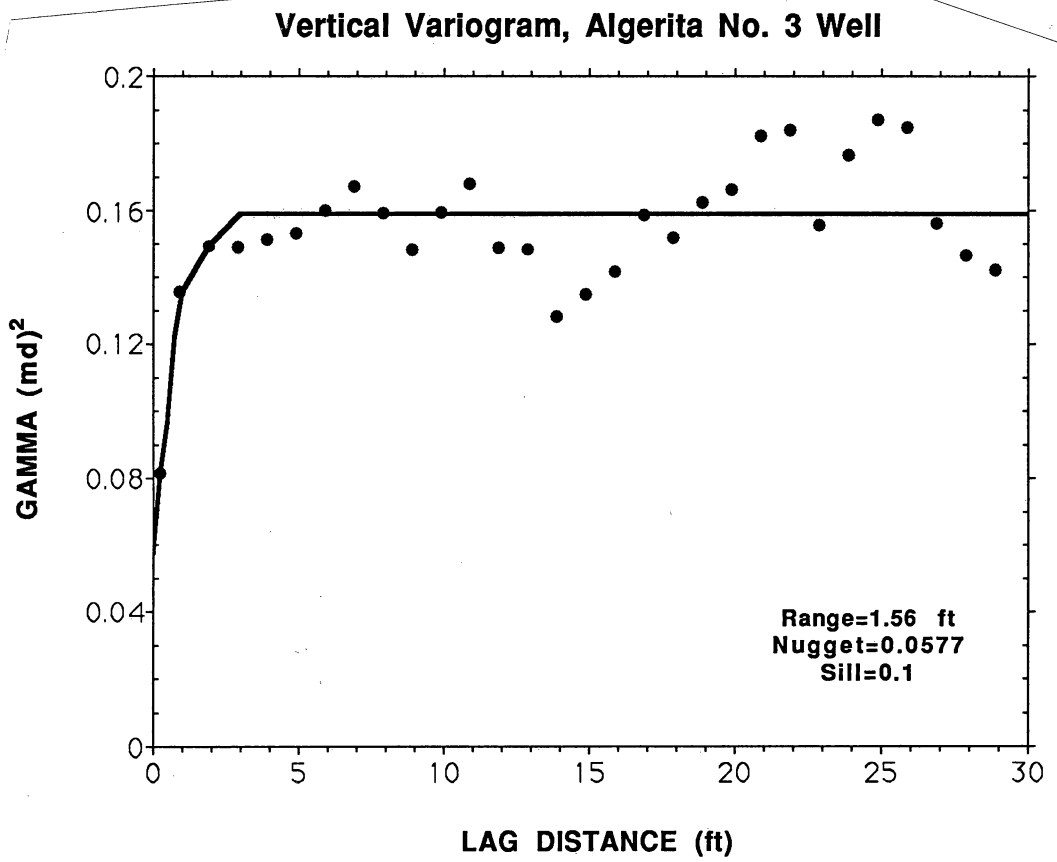
Figure 59. Vertical variogram model for the interval from 460 to 520 ft in the core from Algerita No. 3 well.
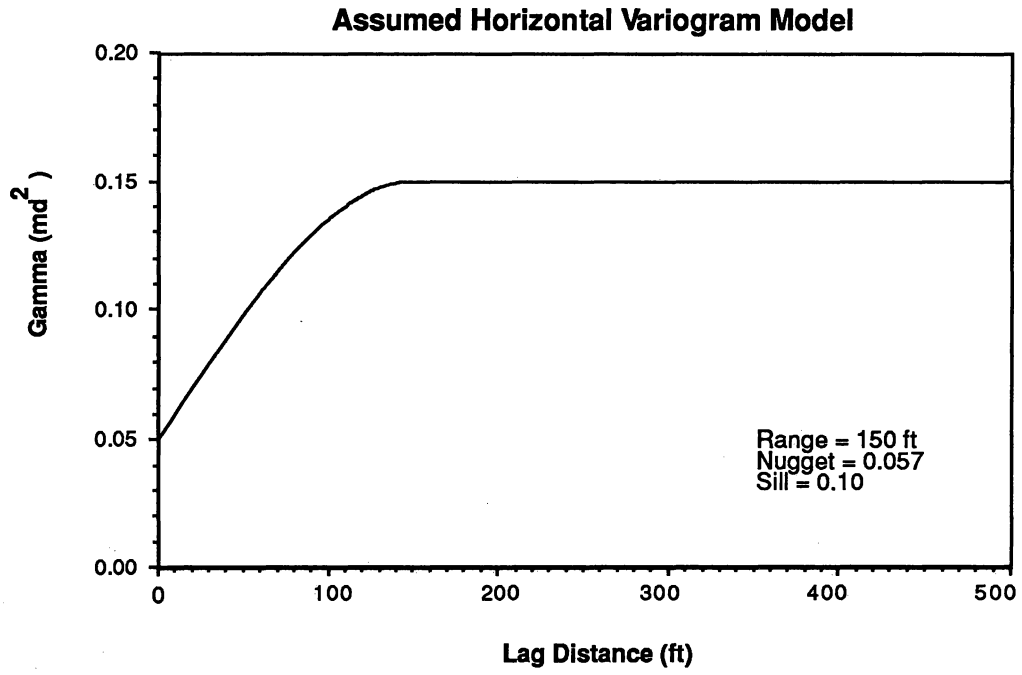
Figure 60. Assumed horizontal variogram model for input into Irabarne Tank Canyon simulation experiments.

Production rate and cumulative production for the three experiments are compared in figures 61 and 62. Production rates of the facies-averaged and conditional-simulation experiments are similar but the conditional-simulation experiment, which included a long-range permeability structure (150 ft), had higher initial production rates than did the facies-averaged experiment. The initial production rate for the interpolated experiment was significantly higher than both other experiments. This result is similar to those of experiments using data from ps1 at Lawyer Canyon, where production rates from kriged permeability maps, which included a long-range permeability structure, were higher than rates from facies-averaged simulations. In both Irabarne Tank cycle 4 and Lawyer Canyon ps1 there is very little difference in the cumulative production characteristics of the various experiments.

Waterflood Simulation of Irabarne Tank Window

Development of flow model

A cross-sectional reservoir simulation model was constructed by using facies-averaged petrophysical values for the six depositional facies described in the geologic framework. As mentioned above, permeability and porosity from outcrop samples of high-moldic fabrics yielded unrealistically high values due to dissolution and fracturing associated with the outcrop. Alternately, permeability data from a core drilled 1,000 ft back from the outcrop in Algerita No. 3 well were used to characterize the spatial variability of permeability in the vertical direction. There is very little difference in the average permeability between moldic and nonmoldic fabrics in the core (see table 7), but subsurface data from the Seminole San Andres Unit indicates a considerable permeability difference between moldic and nonmoldic facies. The reason for the low permeability values in the subsurface is that the moldic porosity is occluded with anhydrite.

In order to obtain permeability values for the moldic and nonmoldic fusulinid fabrics observed in the outcrop that are comparable to subsurface values, data from subsurface
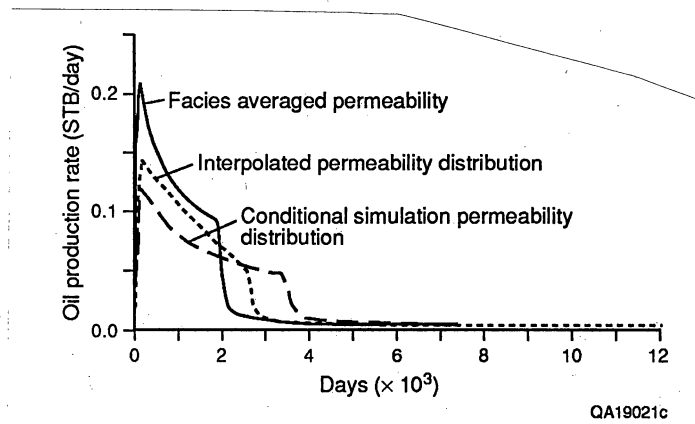
Figure 61. Oil-production-rate versus time for three permeability models of cycle 4, Irabarne Tank Canyon; facies averaged, interpolated, and conditional simulation.
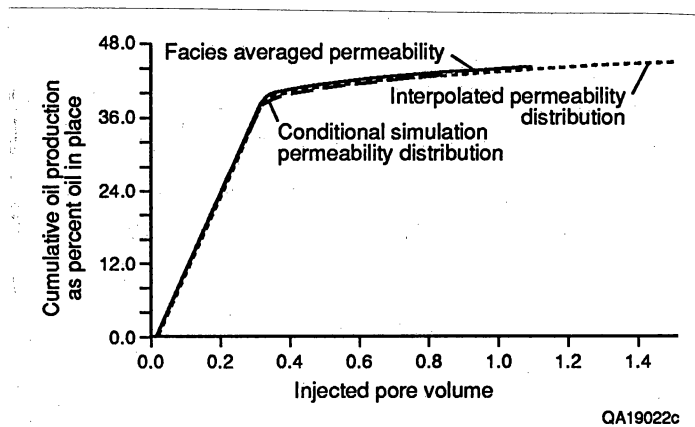
Figure 62. Cumulative-oil-production versus injected-pore-volumes for three permeability models of cycle 4, Irabarne Tank Canyon: facies averaged, interpolated, and conditional simulation.

Table 7. Petrophysical characteristics of rock-fabric units used in Irabarne Tank flow model shown in figure 52.

Unit No.	Rock Fabric	Porosity (%)	Permeability (md)	Initial Water Saturation (%)
1	Mudstone	4.0	0.01	90.0
2	Moldic fusulinid-peloid packstone	12.0	0.34	24.0
3	Mixed moldic/nonmoldic fusulinid-peloid packstone	11.0	0.34	26.9
4	Mixed moldic/nonmoldic fusulinid-peloid packstone/grainstone	8.6	2.61	22.5
5	Peloid packstone/grainstone	10.0	9.00	17.3
6	Brachiopod-sponge-crinoid bioherm	4.0	0.01	90.0

equivalent rocks in the Seminole San Andres Unit were used. Permeabilities and porosities were calculated from geophysical logs in eight wells for two fusulinid cycles, cycles 10 and 11 (see section on Seminole San Andres Unit). The lower parts of cycles 10 and 11 are characterized by moldic and mixed-moldic fusulinid-wackestone facies having a geometric-mean permeability of 0.34 md and an arithmetic-mean porosity of 11.5 percent. The upper part of cycles 10 and 11 are characterized by nonmoldic fusulinid-packstone facies havng a geometric-mean permeability of 2.61 md and an arithmetic-mean porosity of 8.6 percent. The histogram and overall statistics of the two facies are shown in figure 63. Comparison of the mean permeability indicates that the two distributions are significantly different (fig. 64).

A two-dimensional grid composed of 37 layers of varying thicknesses divided laterally into 25 ft segments was constructed to encompass the heterogeneity of the Irabarne Tank geologic framework (fig. 52). The petrophysical values used to calibrate the geologic framework are shown in table 7. Values for the three fusulinid facies (nos. 2, 3, and 4) are from subsurface data. The values for the peloid packstone/grainstone were taken from Lawyer Canyon bar-flank grainstone (table 4). The mudstone and bioherm fabrics are dense and were given typical values for dense carbonate. Water saturation, relative permeability curves, and capillary pressure curves required for the reservoir-flow model were generated for each facies using the rock-fabric approach described in the section on Lawyer Canyon simulation (see equations [1] through [6]).

Simulation results

Two simulation experiments were run to test the effect of dip on recovery and direction of water flow. The first simulation used the model with a dip of 2°. The second simulation used the same model except that the dip of the clinoform cycles was increased from 2° to 5°, more representative of equivalent clinoform units farther basinward.
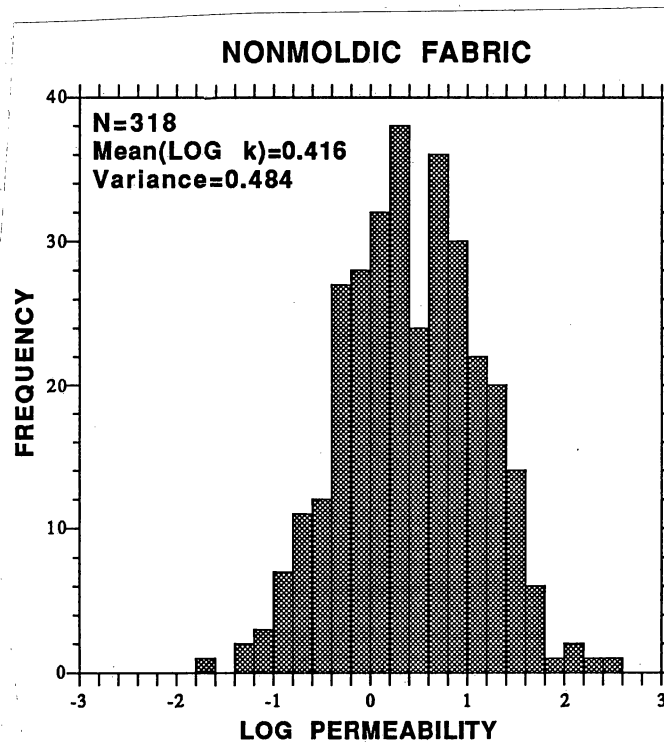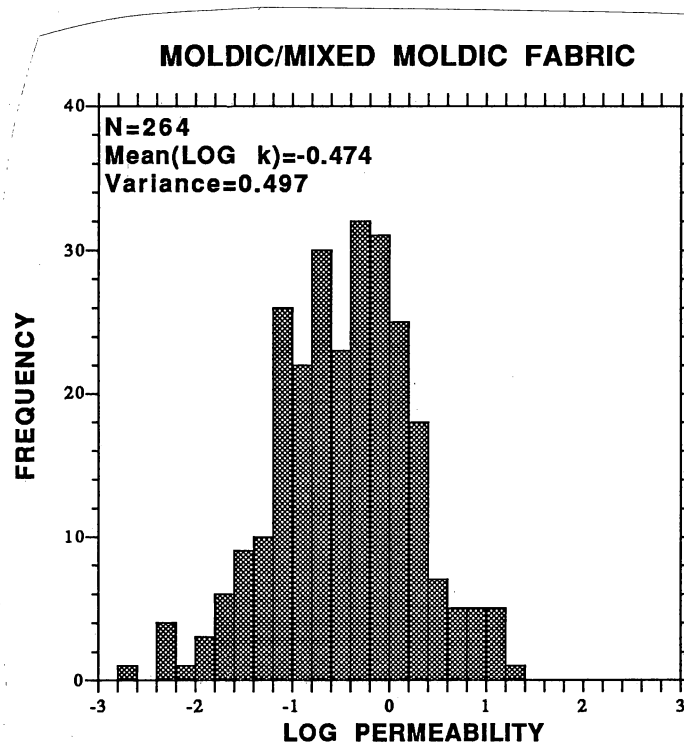
Figure 63. Histograms of (a) nonmoldic and (b) moldic/mixed moldic facies of cycles 10 and 11, Seminole San Andres Unit.
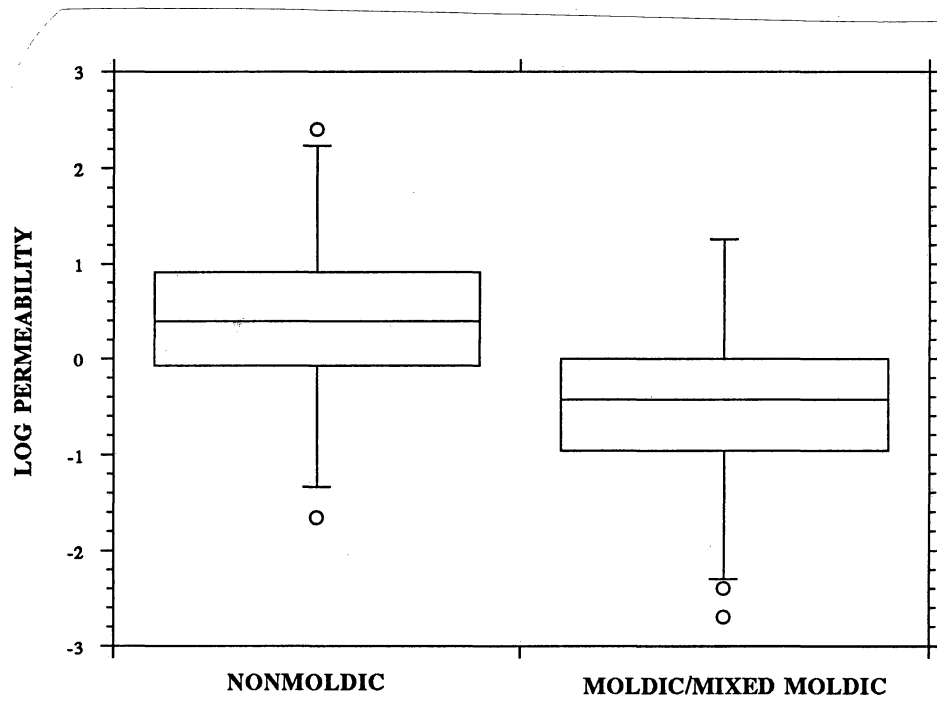
Figure 64. Comparison of geometric means of permeability between nonmoldic and moldic facies from cycles 10 and 11, Seminole San Andres Units.

Results of the numerical waterflood simulations are shown in figures 65 and 66. The water saturation and changes in water saturation after injecting water for 20 yr from the right side of the cross-sectional model and producing from the left side of the model are shown in figure 65. The water-injection front advances farthest through the nonmoldic, high permeability fabrics; the distance is dependent on how continuous the beds are. The potential trapping of mobile oil by cross flow is shown by the water saturation map after 20 yr of injection; this map shows areas of relatively low water saturation enclosed by areas of high water saturation. One area is in cycle 7 on the right side. Other areas are in cycles 4, 5, and 6.

The oil-production rates and water-cut curves (fig. 66) do not show any difference between 2° and 5° in depositional dip on the clinoforms. On the other hand, the curves indicate some differences associated with the waterflood direction, illustrating the importance of the spatial distribution of the facies.

RESERVOIR CHARACTERIZATION APPLICATION—SEMINOLE SAN ANDRES UNIT

Regional Setting of the Seminole San Andres Unit

The Seminole San Andres Unit lies on the northern Central Basin Platform immediately south of the San Simone Channel. Preliminary interpretation of regional seismic data suggests that the Seminole is one of several isolated lower to middle San Andres buildups that became linked with the rest of the San Andres platform only during youngest phases of San Andres sedimentation. Other such buildups include West Seminole, East Seminole, and Hanford. Significantly, reservoir character and quality in the San Andres at Seminole should thus change toward the margins of the productive structure because this structure mimics original depositional geometry.

Initiation of the Seminole buildup followed flooding of the subaerially exposed uppermost Clearfork platform, in a manner analogous to the major flooding event observed atop the Yeso along the Algerita Escarpment. In a dip cross section from Seminole basinward
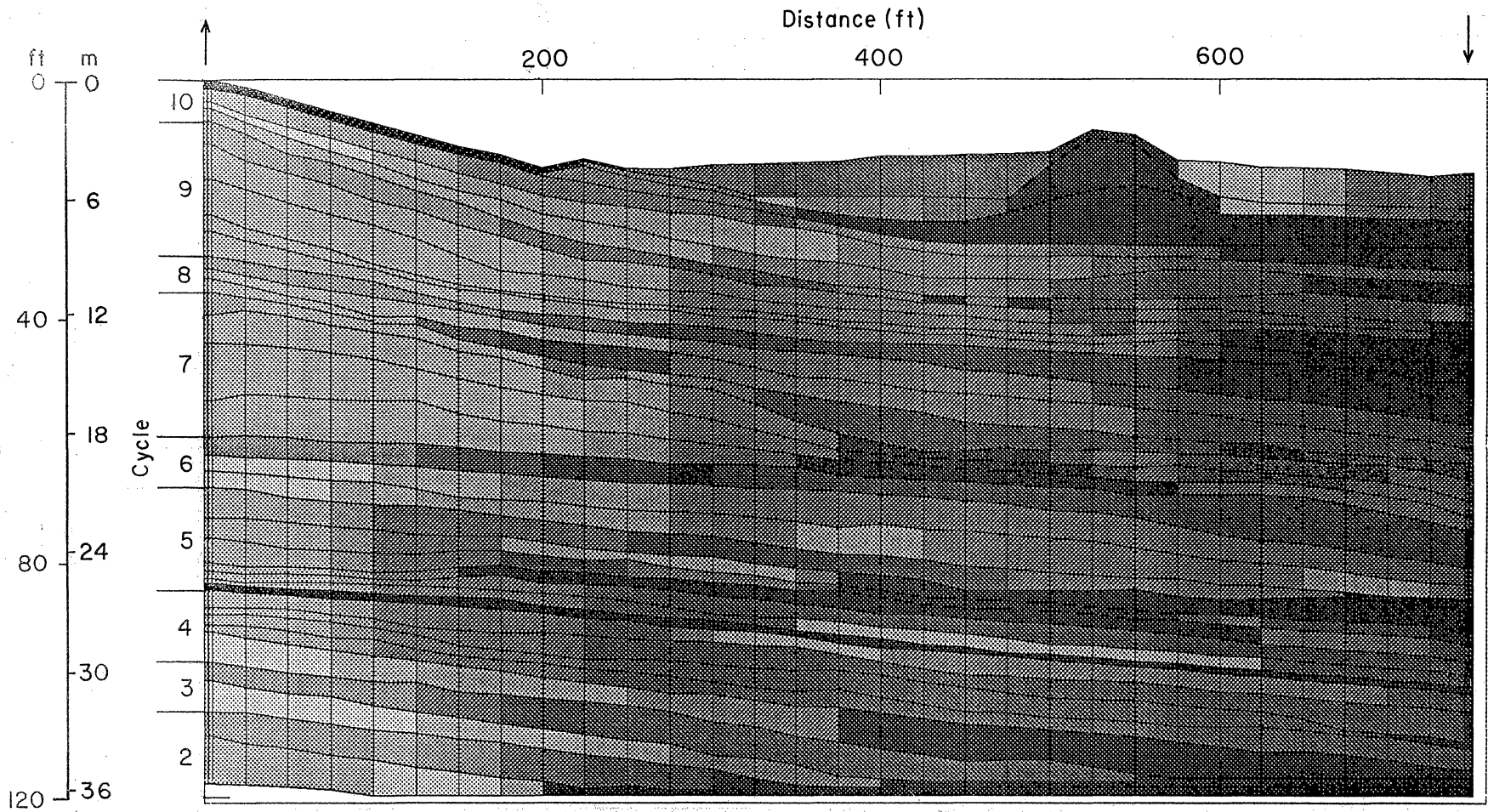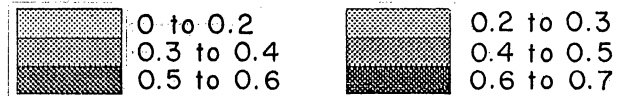
Figure 65. Results of computer simulation of Irabarne Tank Canyon flow model injecting from right to left. (a) Change in water saturation after 20 years of waterflooding. (b) Distribution of water saturation after 20 years of waterflooding.

QAI9038

Figure 65. (cont.)

QAI9037

114

(a)

Right to left
2 and 5 degree dip

Left to right
2 and 5 degree dip

QA19020c

F66

(b)

Left to right
2 and 5 degree dip

Right to left
2 and 5 degree dip

QA19019c
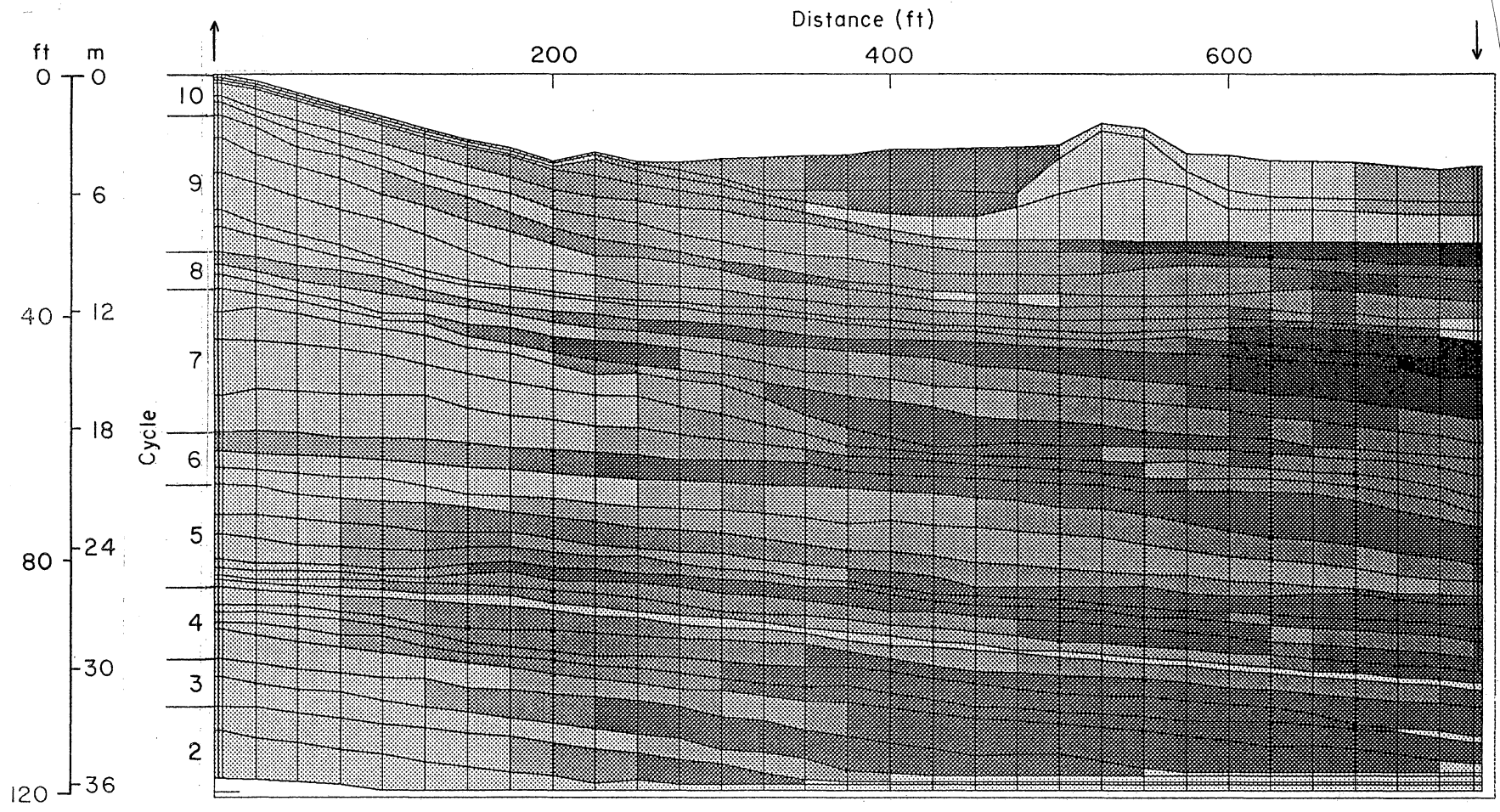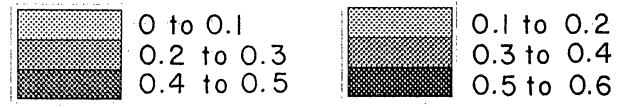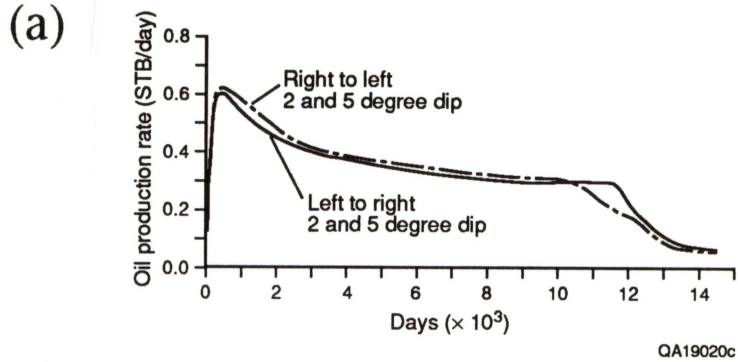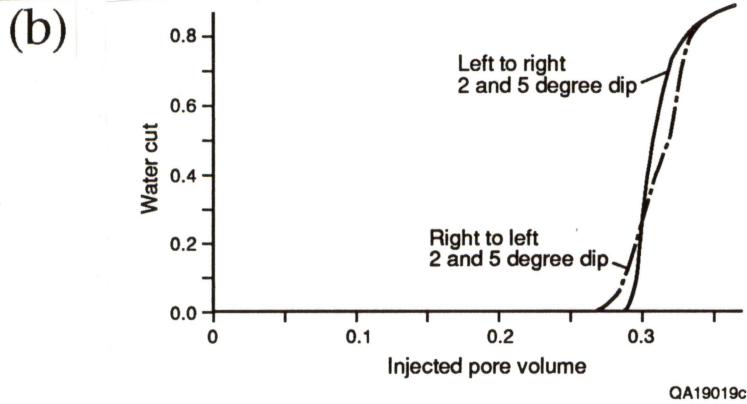
Figure 66. Results of computer simulation of Irabarne Tank Canyon flow model. (a) Oil-production rate versus rate assuming 2° and 5° dip (curves overlie each other) and injecting from right and from left side of model. (b) Water cut versus injected pore volume assuming 2° and 5° dip (curves overlie each other) and injecting from right and from left side of model.

115

toward the San Simone Channel, the San Andres lmSA1 platform margin stepped back 2 mi; the backstep to the contiguous San Andres margin of the Central Basin Platform is 9.5 mi. In the Guadalupe Mountain outcrops, the equivalent shelf margins backstep 20 mi from latest Leonardian below (terminal Victorio Peak/Bone Springs facies contact) to earliest lmSA1 San Andres above (bioclastic shallow-shelf wackestone/packstone to distal outer ramp mudstones).

The sequence boundary between the upper Clearfork and the San Andres is not cored but it is interpreted to be near the top of a series of stacked tidal-flat complexes in the position of the Glorieta gamma-ray pick. The only core at Seminole that penetrates the lower San Andres TST is the SSAU-5309 core. This core shows this interval to contain skeletal grainstones and packstones, and it has open-marine fauna comparable to that of the lower San Andres TST of the outcrop. The TST, which is 750 ft thick, has high porosity and permeability, but it is in the water leg and nonproductive.

Maximum flooding is represented at Seminole by cherty fusulinid wackestones. No true cherty mudstone interval comparable to that seen in the middle San Andres at Lawyer Canyon, Algerita Escarpment, is developed. This transition from open-marine shallow-ramp wackestones and packstones to HST restricted-ramp wackestones and packstones is similar to the TST to HST transition in the northern parts of the Algerita Escarpment (sections AC, WC, fig. 5).

The remainder of the cored interval is undivided highstand deposits that include approximately 450 ft of porous carbonates and 380 ft of largely anhydrite-cemented tidal-flat(?) cycles. The lower porous reservoir section is thought to contain highstand deposits of at least two sequences, the equivalent of the lmSA1 and uSA1 sequences of the Algerita outcrop model. The equivalents of the uSA2 through uSA4 sequences are presumed to be equivalent to the upper tidal-flat section at Seminole.

Data for Geologic Analysis

Data for the sequence-scale geologic characterization at Seminole included (1) a regional log cross section from the outcrop in New Mexico to the San Simone Channel area, (2) a regional seismic grid, and (3) nine cores and associated well logs along a north-northwest-trending fieldwide cross section along the axis of the reservoir. For the detailed interwell study a two-section area in the north part of the reservoir (sections 230 and 231) was selected that contained (1) 62 wells and log suites, (2) 11 cored wells, 4 on the corners of a 10-acre 5-spot, and (3) per-well production data (fig. 67).

Detailed Geologic Mapping—the Parasequence Framework

The goal of the geologic characterization was to develop a three-dimensional framework that accurately portrays the distribution of geologic facies and that can be translated into petrophysical rock types for generating maps of such basic attributes as K/h, phi/h, Swi, and So/phi/h.

A key result of the integrated outcrop study was the recognition that the basic architecture of the San Andres is dominated by 10 to 30 ft upward-shallowing, -coarsening cycles or parasequences that are mappable on the scale of 1,000's of ft laterally and that can be related to petrophysical and flow properties via a rock-fabric facies mapping approach (see section on Petrophysical Description, Upper Interval). Although upward- shallowing cycles are widely recognized in carbonate deposits (Wilson, 1975; James, 1977), the role of these cycles in controlling fluid flow and recovery properties within a reservoir has not been quantified.

Using the results of the detailed parasequence window mapping from the outcrop as a guide, the Seminole cores from the main pay section were logged in detail and interpreted in terms of a series of upward-shallowing parasequences. The study focused on the upper 250 ft of the Seminole reservoir because lower parasequences in the fusulinid-dominated section showed

117

Legend:

—■— Line of cross section in Figure 16

RCRL detailed study area

Amerada window simulation study

■ Cores selected for study

△ RFT data

o Well

0   1   2 mi
0   1   2   3 km

N

QA12561
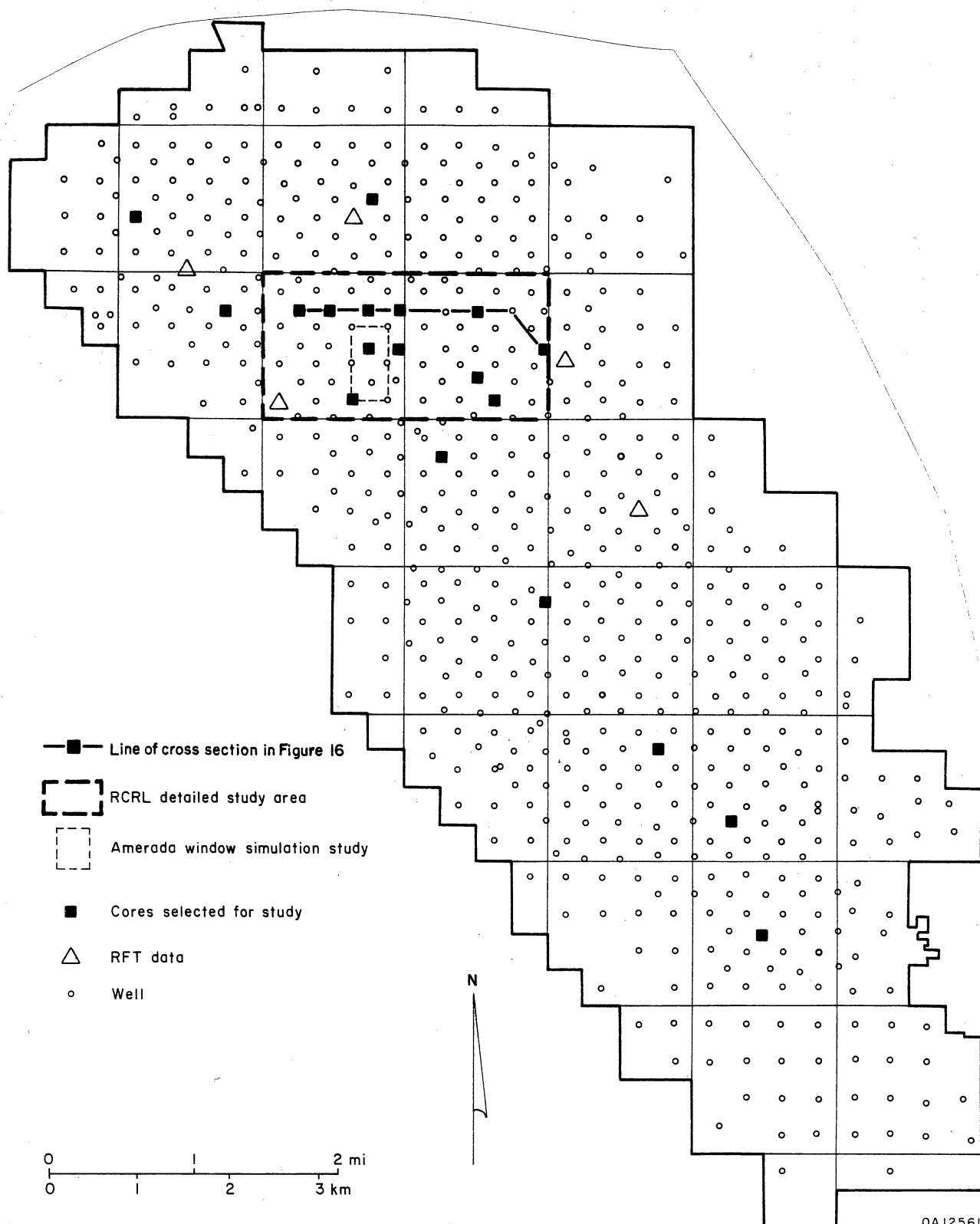
Figure 67. Well location map of Seminole San Andres Unit indicating cores used in this study and the two-section area selected for detailed geologic/petrophysical analysis. Location of detailed cross section in figure 68 is also shown.

little rock-fabric variability. Cores were described on a foot-by-foot basis and linked to well-log response (mainly gamma ray) before, during, and after core description. Through an iterative process of description and correlation, 11 parasequences were confidently identified in cored and uncored wells both in the detailed study area and on the reservoir-wide cross section (fig. 68).

The lower three parasequences (10 through 12) are 20- to 30-ft-thick units containing dense moldic fusulinid-peloid wackestone/packstone coarsening upwards into skeletal-preserved crinoid-fusulinid-peloid packstone/grain-dominated packstone. The coarser grained upper portion of these parasequences typically displays high porosity values.

Parasequences 6, 8, and 9 are transitional between the outer ramp fusulinid-dominated lower parasequences (ps10 through 12) and the inner ramp tidal-flat-capped parasequences (ps1 through 5). They display laterally variable internal facies mosaics that include ramp-crest grain-dominated packstone to grainstone fabrics comparable to those of ps1/uSA1 at Lawyer Canyon. True crossbedded ooid grainstones are rare, however, and thick single-cycle grainstone bars such as ps9/uSA1 of Lawyer Canyon are not observed in the detailed section study area. Seminole ps6 does show marked thickening of its grainstone facies in a southerly direction from 2 ft in the north to 20 ft ~5 mi south along the north-northwest fieldwide cross section.

Another difference between the Seminole ramp-crest grain-rich parasequences and their equivalents on the outcrop is the lack in the subsurface of thick basal mudstone-peloid-wackestone flooding surfaces. Instead, fusulinid-peloid wackestone-packstone typically marks parasequence flooding surfaces. This is significant for the flow-modeling perspective because some of the Seminole wackestone-packstones have moderate permeabilities rather than the low permeabilities described at Lawyer Canyon.

The upper five parasequences (ps1 through 5) are thinner (5- to 20-ft-thick) inner ramp units that all aggrade at least locally into fenestral peritidal deposits. Parasequences 2 through 5 have thin, laterally discontinuous grainstone intervals and are therefore analogous to Lawyer Canyon parasequences ps3 and 5/uSA1. Extension of detailed mapping outside the detailed

119
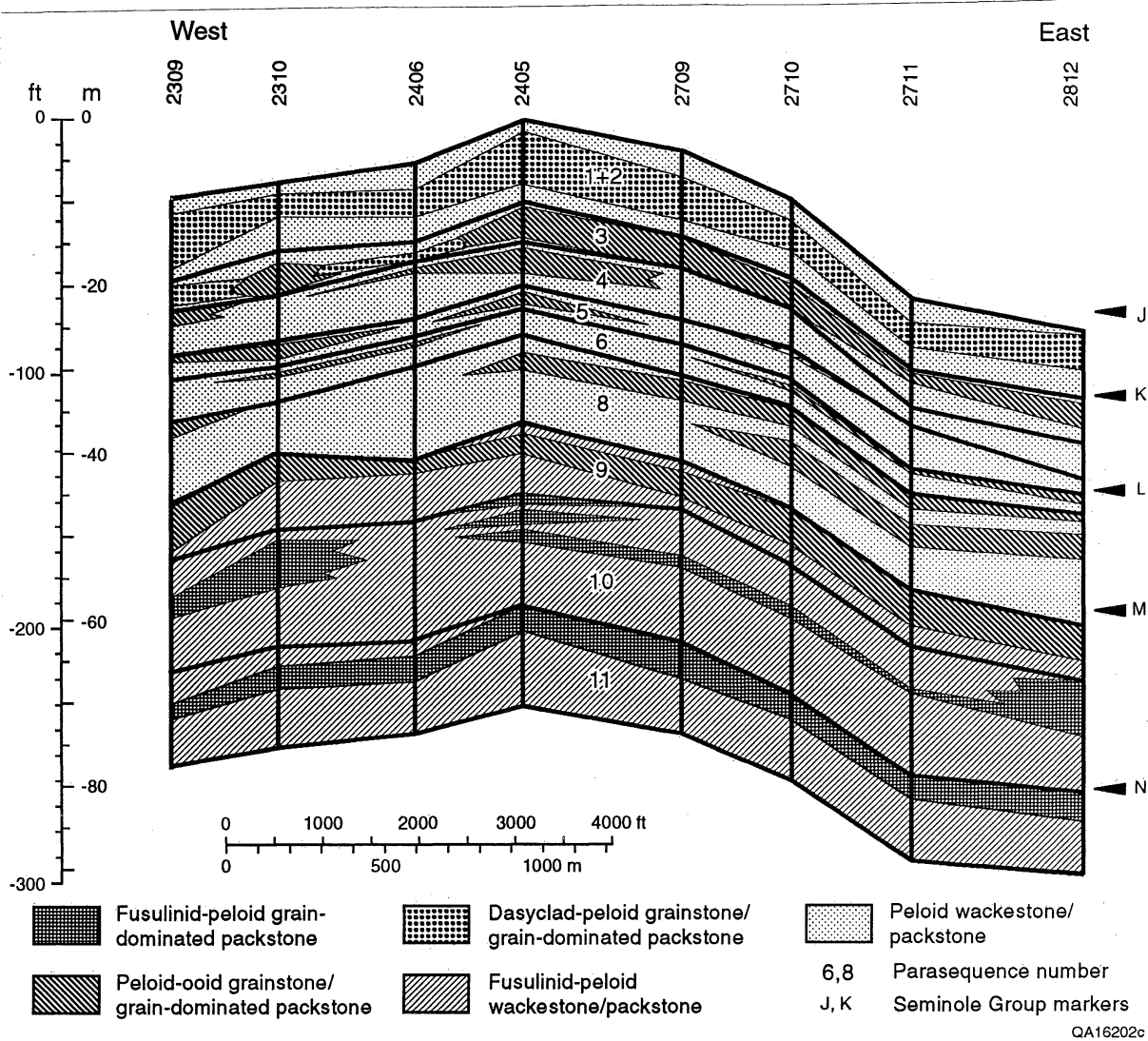
Figure 68. Simplified geologic west-east cross section through the detailed study area based on core data only. High-energy grain-dominated packstones and grainstones are indicated for both outer ramp and ramp-crest parasequences. Line of section shown in figure 67.

two-section study area will probably demonstrate these upper parasequences to be most heterogeneous and therefore least efficiently swept. Tracing these upper parasequences from the detailed study area southward demonstrated that the top of porosity moved downward so that in the detailed study area it was at the top of ps1, whereas 3 mi south it was at the top of ps3.

Petrophysical Description, Upper Interval

The Seminole San Andres reservoir is located on the northern edge of the Central Basin Platform in the Permian Basin. A two-section area in the northern sector of the reservoir was selected for a detailed reservoir study because of the excellent core control available (figs. 67 and 69). Only the upper interval of the productive zone has been studied in detail. All 11 cores have been described and 1 core has been analyzed in detail using thin sections. Quantitative relationships between wireline-log response, rock fabrics, pore types, saturation, and permeability have been developed and used to define a rock-fabric flow model.

Core Description

The core from Amerada No. 2505 well was chosen for detailed thin-section analysis. Thin sections were prepared from each foot of core; 150 thin sections were prepared from the upper interval of the San Andres reservoir. Percentages of minerals, grains, mud, cement, interparticle pores, and separate vugs were determined by the point-count method. Average crystal and grain sizes were estimated using an ocular micrometer.

Rock fabrics

Three basic dolomite rock fabrics are present in the upper productive interval of the Seminole San Andres reservoir: (1) fine crystalline grainstones, (2) grain-dominated packstones,

121
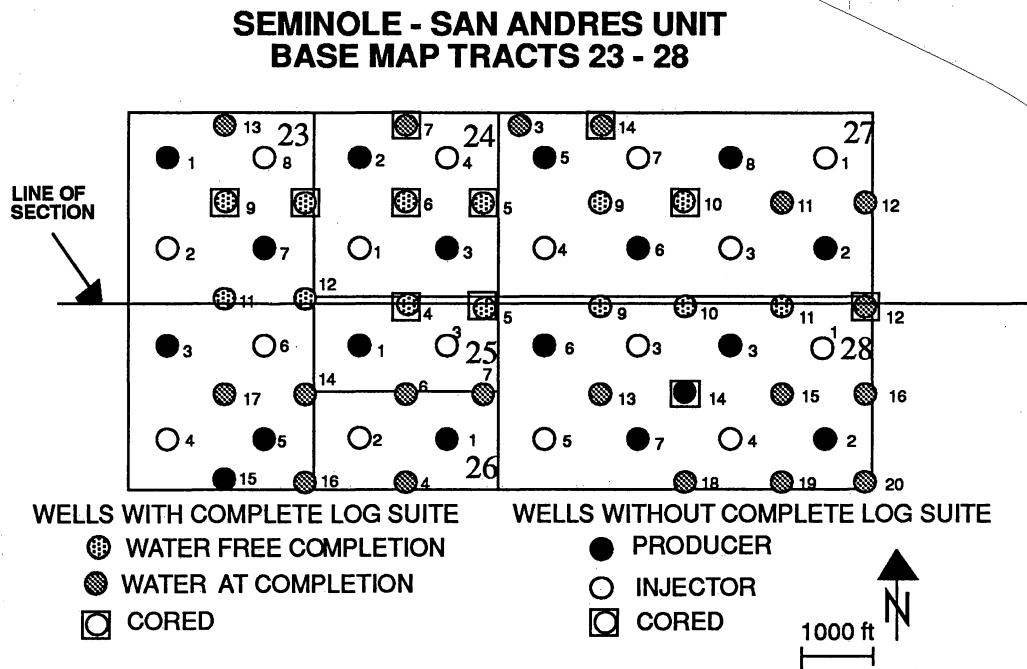
Figure 69. Index map of the two-section study area in the Seminole field, Gaines County, Texas.

and (3) mud-dominated wackestones (fig. 19). The dolomite crystal size is generally 10 to 20 μm in diameter but increases slightly to 25 μm at the base of the upper interval. This increase in dolomite crystal size defines a fourth rock fabric, a mud-dominated dolomite with medium crystal size.

Particle size and sorting

A depth plot of particle size and sorting is shown in figure 70. Grainstones are composed of grains averaging ~250 μm in diameter. Grain-dominated packstones are composed of a mixture of 250 μm grains, intergranular dolomitized mud, and intergranular pore space and cement. Grain-dominated packstones are indicated in figure 70 by a particle size of 100 μm. Mud-dominated fabrics have particle sizes equal to the dolomite crystal size of 10 to 25 μm.

Particle size increases upward within each cycle representing upward-shoaling conditions. Grain-dominated packstones, however, dominate the upper parts of the cycles, with grainstones increasing in importance in the upper cycles.

Anhydrite

All four rock fabrics contain poikilotopic and pore-filling anhydrite in varying amounts. The volume of anhydrite in the thin sections was measured by the point-count method (TSD). Samples from the same foot were crushed and the volume of anhydrite determined by XRD. Sample density was overlying most of the cored interval at every foot. The XRD results show higher amounts of anhydrite than does the TSD. The average anhydrite from XRD is 23 percent whereas the average value from TSD is 13 percent (fig. 70).

The TSD and XRD values were averaged and a depth plot was made. Where only one value was present it was used, and where no value was present a value was interpolated. To correlate with wireline logs, 3-ft running averages were made of the depth plot. Anhydrite volumes range from 5 to 45 percent in the upper productive interval. However, a plot of

123
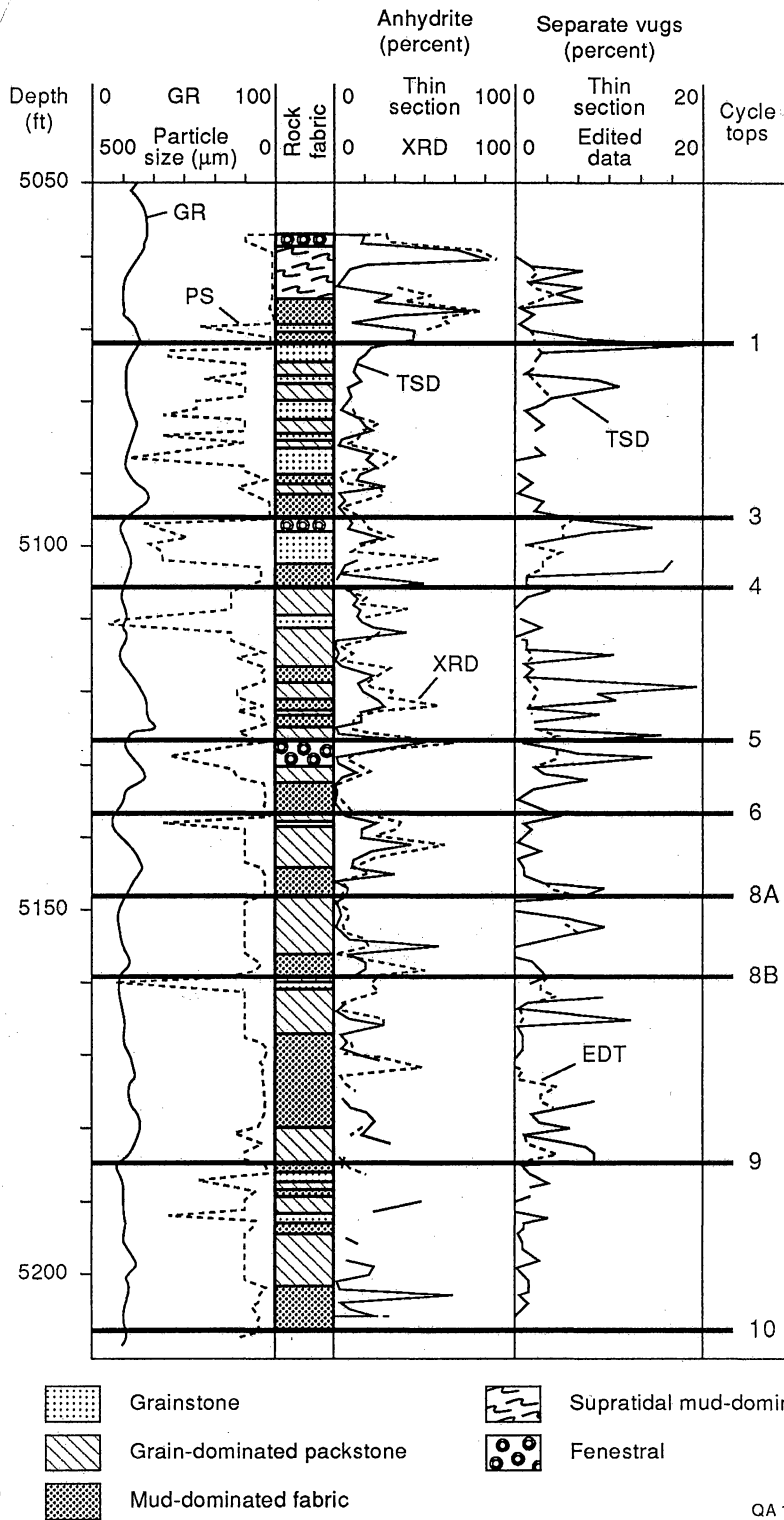
Figure 70. Depth plot from upper productive interval of Amerada No. 2505 well, illustrating gamma-ray log, particle size, rock fabric, anhydrite volume, separate-vug porosity, and parasequences.

124

whole-core porosity versus percentage of anhydrite in the thin section (fig. 71) shows no correlation. This suggests that anhydrite is predominantly replacement rather than pore filling.

The volume of poikilotopic anhydrite varies significantly within a whole-core sample. Commonly, the amount of anhydrite varies by a factor of 2 and occasionally by a factor of 10 (fig. 72). The values from the original thin sections and from the XRD fall mostly within the range of values from the three plugs.

Porosity

The relationship between point-count porosity from thin sections and Boyles-law porosity from whole-core samples is shown in figure 73. In general, point-count porosity is expected to be lower than core-analysis porosity because very small pores are not visible in thin section. However, many of the data points show thin-section porosity higher than core-analysis porosity. This anomalous relationship was investigated by measuring porosity and permeability of 3 plug samples from each of 12 whole-core samples and point-counting thin sections made from the samples. Porosity and permeability were measured before and after sample cleaning.

The results show that porosity in the cleaned plugs is several units higher than in the uncleaned plugs and that the porosity of the cleaned plugs is as much as 4 porosity percent higher than porosity from whole-core analysis (fig. 74). Plug porosity values from one whole-core sample typically vary by 2 or 3 porosity percent. Thin-section porosity varies but is always less than plug porosity.

Adding 4 porosity percent to the whole-core porosity values results in most thin-section porosity values being lower than the corrected core-analysis porosity (fig. 73). Thin sections that have more porosity than the corrected core porosity also tend to have the highest separate-vug porosity. Core examination shows high values of separate-vug porosity to be concentrated in beds that are a few inches thick, suggesting that thin sections with high separate-vug porosity are not representative of the core. Indeed, a statistical analysis of the

125

ANHYDRITE VS TOTAL POROSITY
UPPER INTERVAL - WELL SSAU 2505
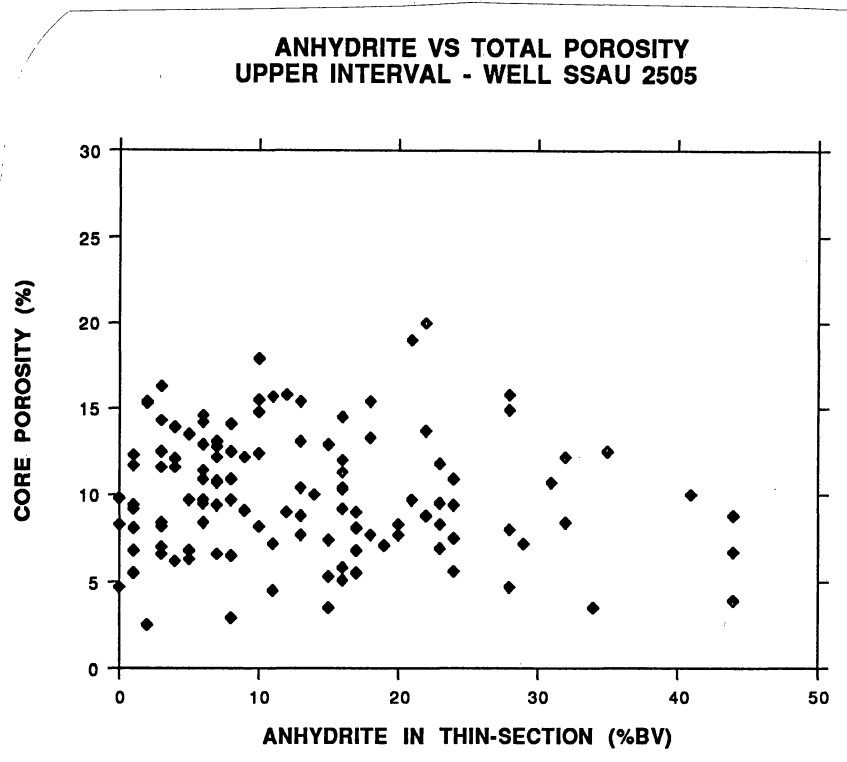
Figure 71. Plot of percent anhydrite versus percent porosity, showing that porosity is not a function of anhydrite volume.
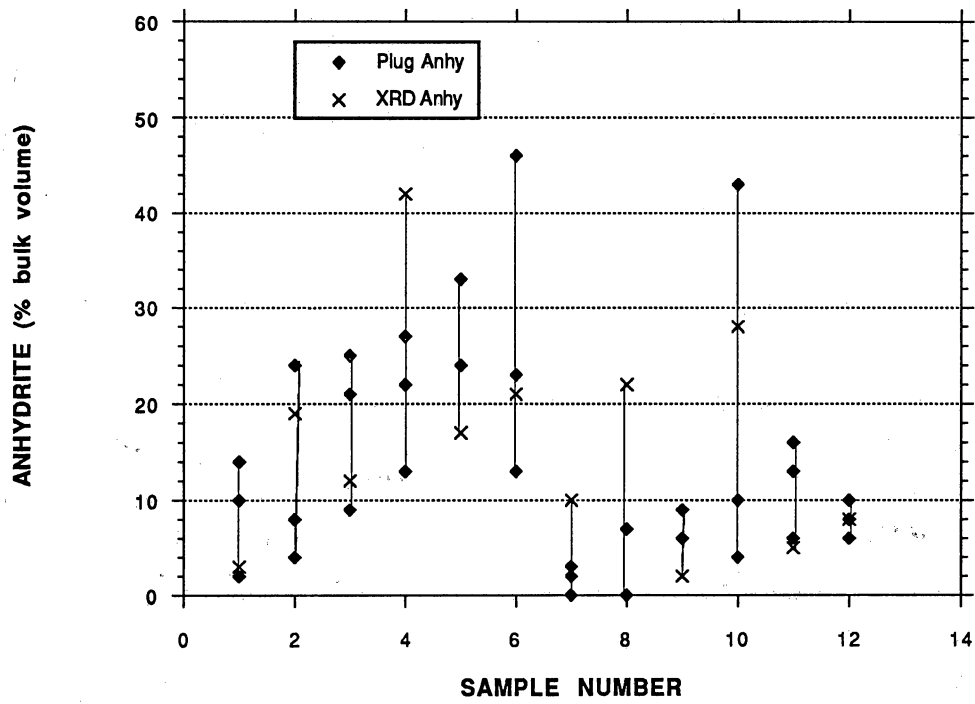
Figure 72. Graphic display showing the range of anhydrite in selected whole-core samples. Values are from three plugs about 1 inch apart and one XRD sample of a small area.
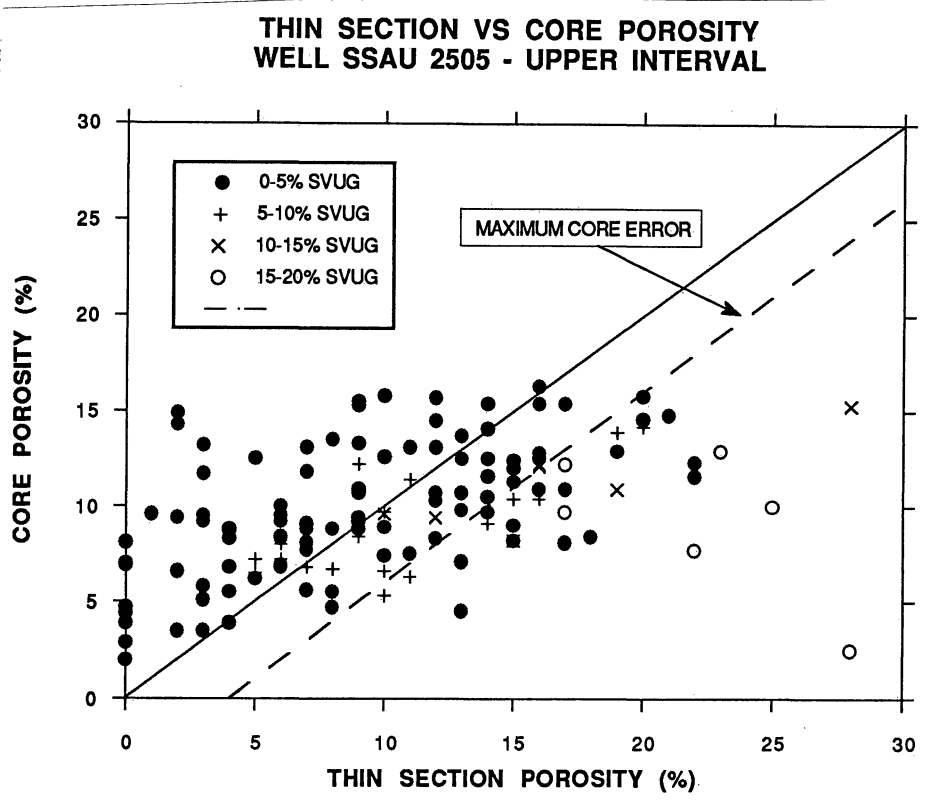
Figure 73. Plot of thin-section porosity versus whole-core porosity showing that thin-section porosity is larger than core-analysis porosity in many samples. The amount of separate-vug porosity is labeled, showing that many samples with high thin-section porosity also have high values of separate-vug porosity. The dashed line assumes that core-porosity values are too low by 4 porosity percent, the maximum porosity error measured (fig. 74).

CLEANED PLUGS VS WHOLE-CORE POROSITY
SSAU WELL 2505
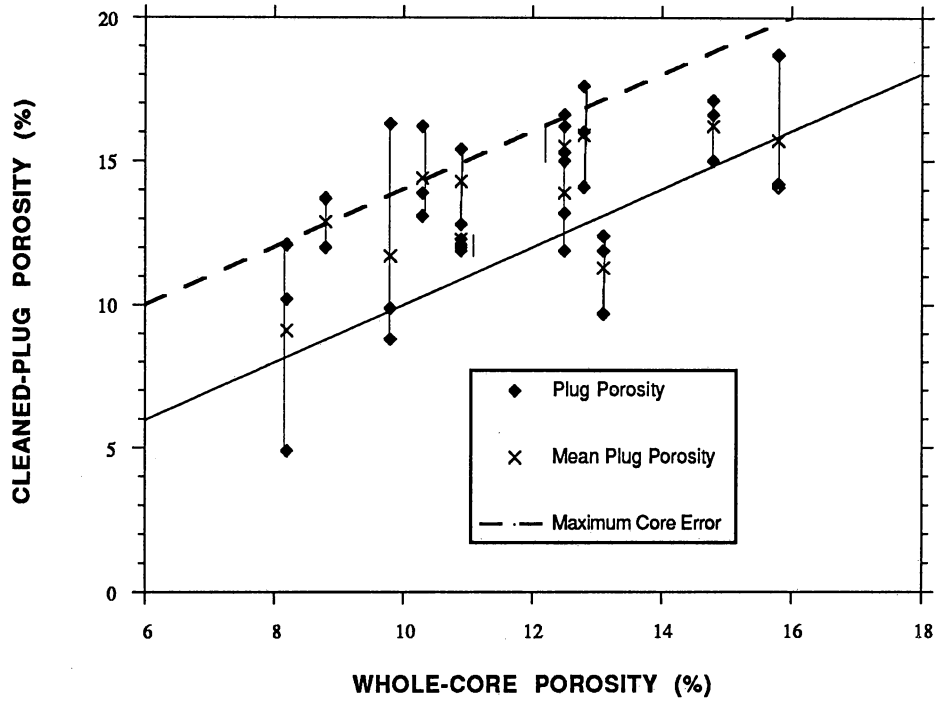
Figure 74. Cross plot of whole-core porosity values versus porosity values of plug samples taken from the whole-core samples and cleaned. Whole-core porosity is too low by 0 to 4 porosity percent.

frequency of separate-vug porosity shows a modal value of 2 percent and that 90 percent of the samples have a separate-vug porosity of less than 10 percent (fig. 75). The reservoir can be characterized as having a few thin beds with greater than 10 percent separate-vug porosity dispersed within beds containing separate-vug porosity of 0 to 9 percent with a mode of 2 percent.

A depth plot of separate-vug porosity was made by deleting separate-vug porosities of 10 percent or more from the thin-section data and then calculating a 3-ft running average on the resulting data. The results, shown in figure 70, show no intervals of consistently high vuggy porosity.

Permeability

The difference in permeability values between whole-core, averaged uncleaned-plug, and averaged cleaned-plug samples is not significant, probably because residual oil is present in the small pores, pores which do not effectively contribute to permeability. A significant range is present, however, between the three plug measurements (fig. 76).

MFP measurements were made on the slabbed faces of the 12 whole-core samples at a density of about 1 measurement/1 inch^2 (fig. 77). As shown in table 8, the arithmetic-mean average MFP values are similar to the whole-core permeability values. In many samples, however, the standard deviation is about equal to the average permeability, suggesting that the permeability can vary by an order of magnitude within a 6-inch core sample.

Rock-fabric, porosity, and permeability transforms

Cross plots of porosity and permeability of specific rock fabrics, using the original whole-core values, show permeability values too high for corresponding porosity values because the porosity values are too high. Cross plots based on data from the plug samples, however, show transforms that are in agreement with the petrophysical rock-fabric classes defined in this

(a)

FREQUENCY DISTRIBUTION - WELL 2505
SEPARATE-VUG POROSITY

(b)
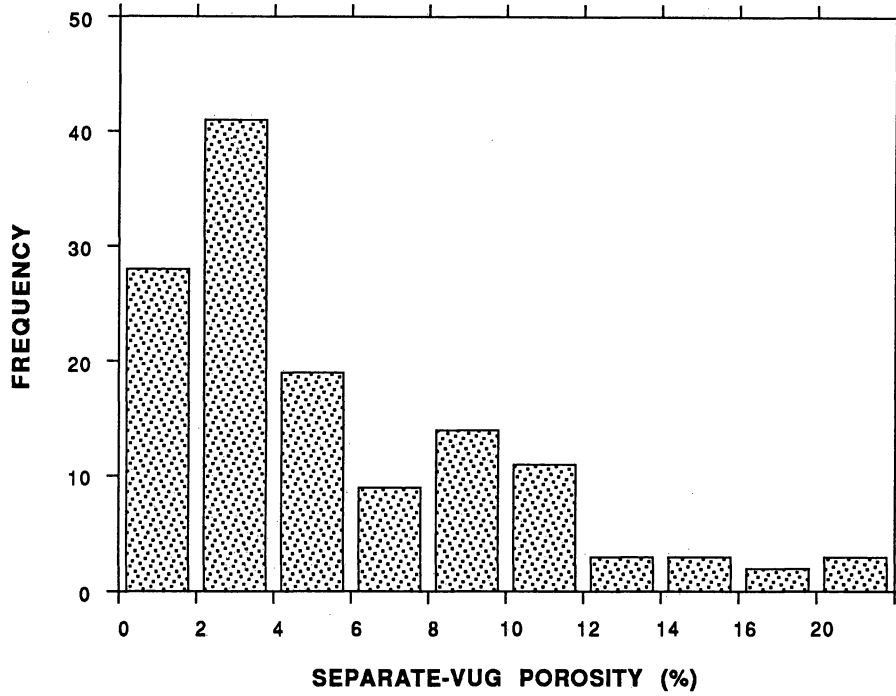
CUMULATIVE FREQUENCY - WELL 2505
SEPARATE-VUG POROSITY
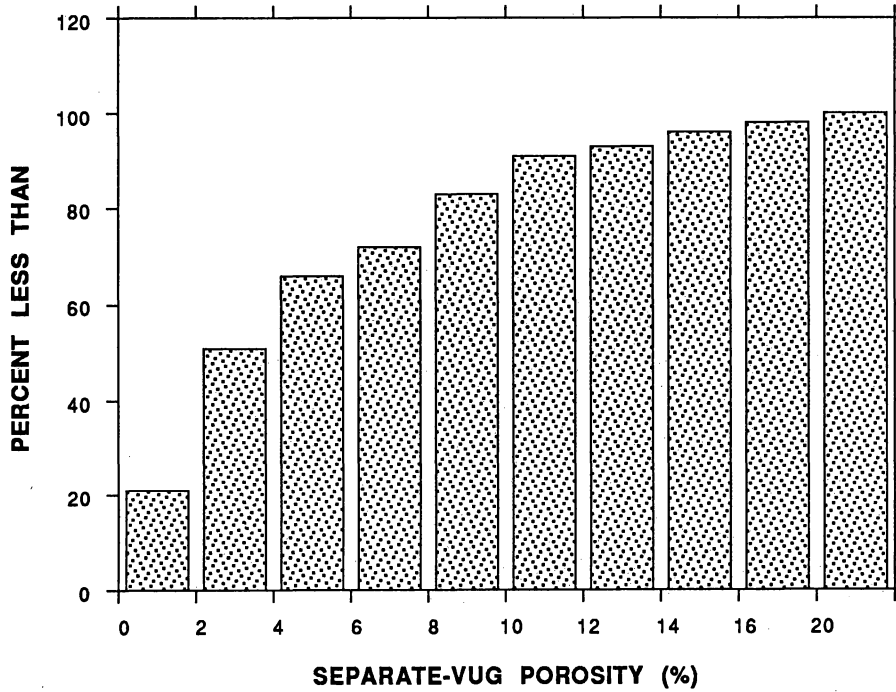
Figure 75. Separate-vug porosity statistics: (a) frequency distribution of separate-vug porosity and (b) cumulative frequency distribution of separate-vug porosity.

131
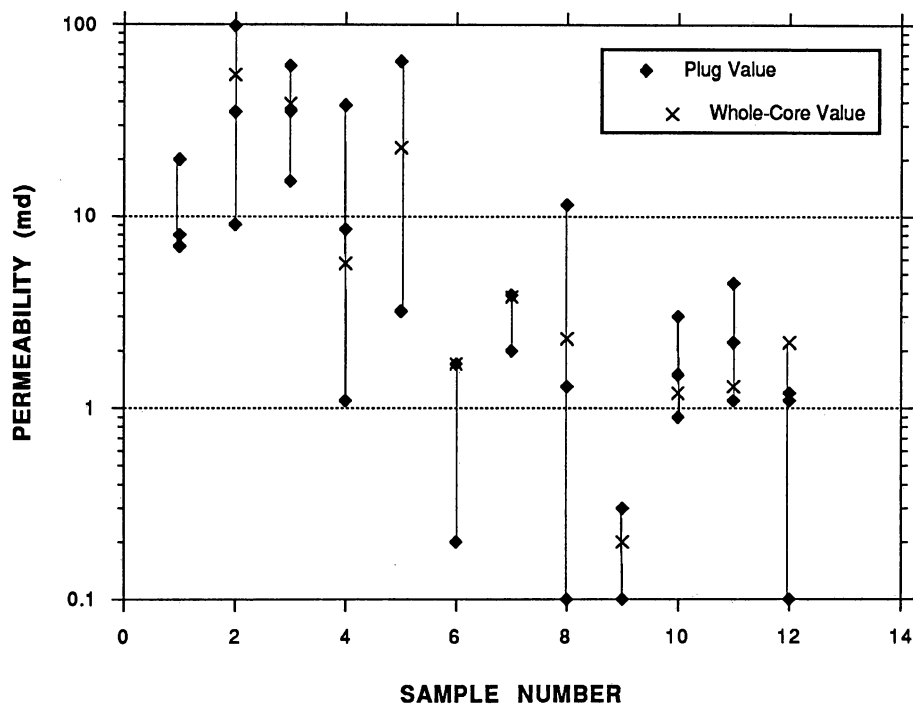
Figure 76. Graphic display showing the range of permeability in selected whole-core samples. Values from three plugs about 1 inch apart are compared with original whole-core values.
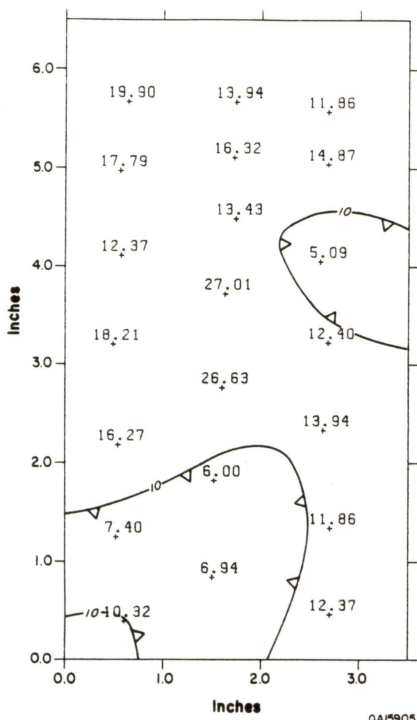
Depth 5106 ft
Grain-Dominated Packstone
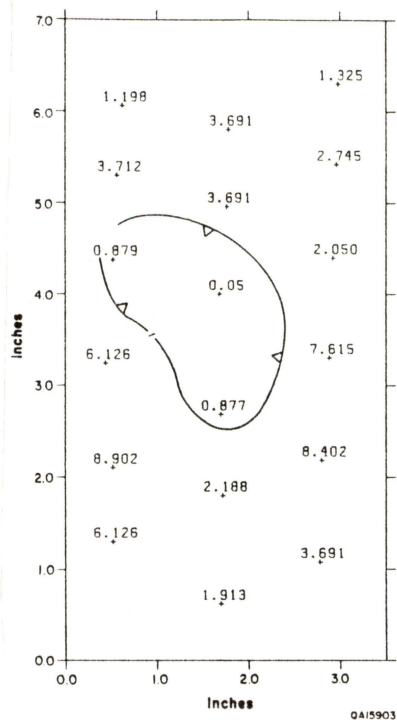
Depth 5144 ft
Wackestone
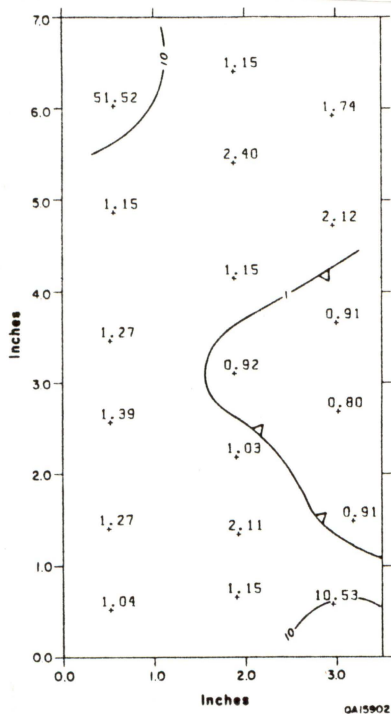
Depth 5166 ft
Wackestone
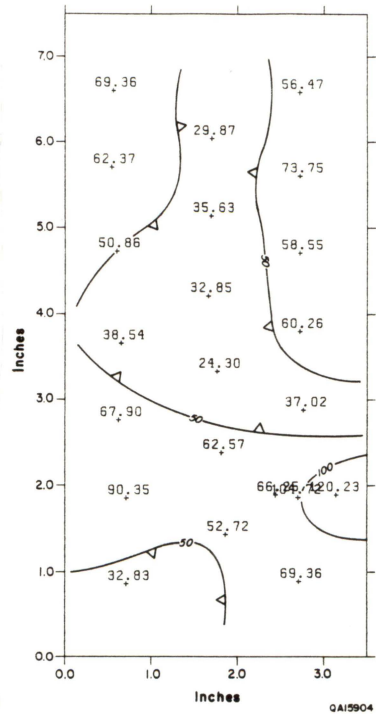
Depth 5107 ft
Grain-Dominated Packstone

Figure 77. Examples of permeability distribution based on miniairpermeameter measurements spaced 1 inch apart on the face of core slabs of selected whole-core samples. Values are in millidarcys.

133

Table 8. Mechanical field permeameter measurements on slab-core surfaces.

Depth (ft)	MFP Arith.-mean perm. (md)	Standard deviation (md)	Whole-core perm. (md)	Rock-fabric classification
5,106	14.15	13.7	7.5	grain-dominated packstone
5,107	56.1	26.4	55.0	grain-dominated packstone
5,108	52.1	28.6	39.0	grain-dominated packstone
5,109	4.8	4.0	5.7	grain-dominated packstone
5,110	14.0	23.7	23.0	grainstone
5,143	0.9	1.1	1.7	wackestone
5,144	3.8	2.8	3.8	wackestone
5,145	1.8	3.0	2.3	wackestone
5,146	0.9	.07	0.2	wackestone
5,166	1.8	2.2	1.2	wackestone
5,167	5.1	6.1	1.3	wackestone
5,168	2.1	1.6	2.2	wackestone

T8

report and in Lucia (1983) (fig. 78). Porosity-permeability transforms are based on interparticle porosity, not total porosity. The transform for the grain-dominated packstones falls in the middle field (fig. 78a), as expected. The transform for mud-dominated wackestones (fig. 78b) falls at the upper limit of the fine-dolomite field because the crystal size is about 20 μm, the upper crystal-size limit for dolomite fabrics in this field.

Log Analysis

Core description and analysis of the accuracy and variability of porosity, permeability, and fabric elements were used to calibrate wireline log response. Numerical relationships were developed to calculate porosity, separate-vug porosity, rock fabrics, and permeability using CNL, density, acoustic, and laterologs. The Terra Science log-analysis program was used in this analysis.

Calculation of porosity and lithology

Lithology was calculated from the wireline logs assuming a composition of anhydrite, dolomite, and porosity. Minor amounts of calcite and quartz identified by XRD were ignored. The amount of anhydrite in the well was established by thin-section analysis and by XRD as described above and plotted versus depth. A 3-ft running average of the anhydrite data was calculated and was used to compare with log calculations.

Only when all three porosity logs were included in the log calculations were reasonable anhydrite volumes calculated (fig. 79). The combination of density and CNL logs resulted in wide swings from 0 to 100 percent anhydrite. Combining density and acoustic logs resulted in low anhydrite values, whereas using the CNL-acoustic combination resulted in high anhydrite values. To obtain a reasonable fit between log and core anhydrite volumes and to correctly calculate porosity, the fluid transit time was reduced from the standard 189 μs/ft to 150 μs/ft. Using 189 μs/ft resulted in low porosity values (fig. 80).

135
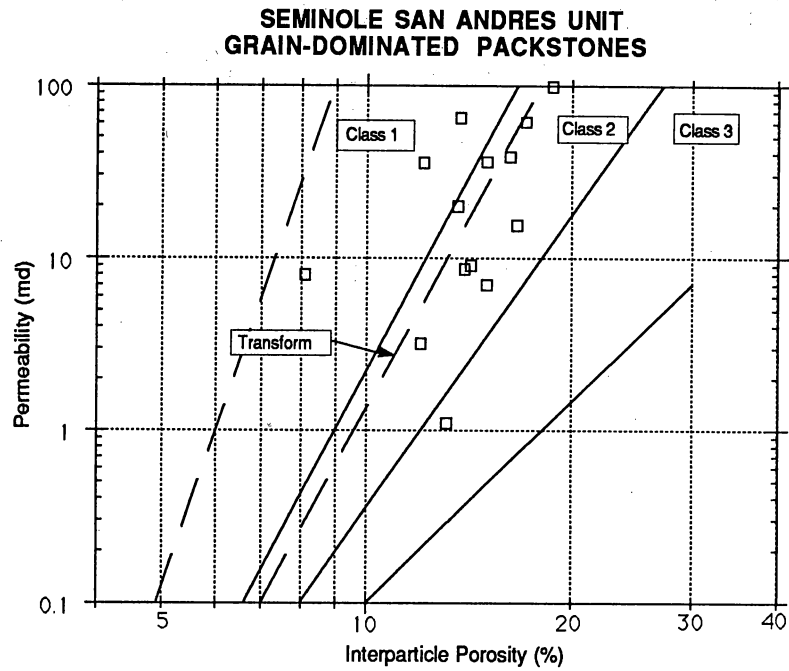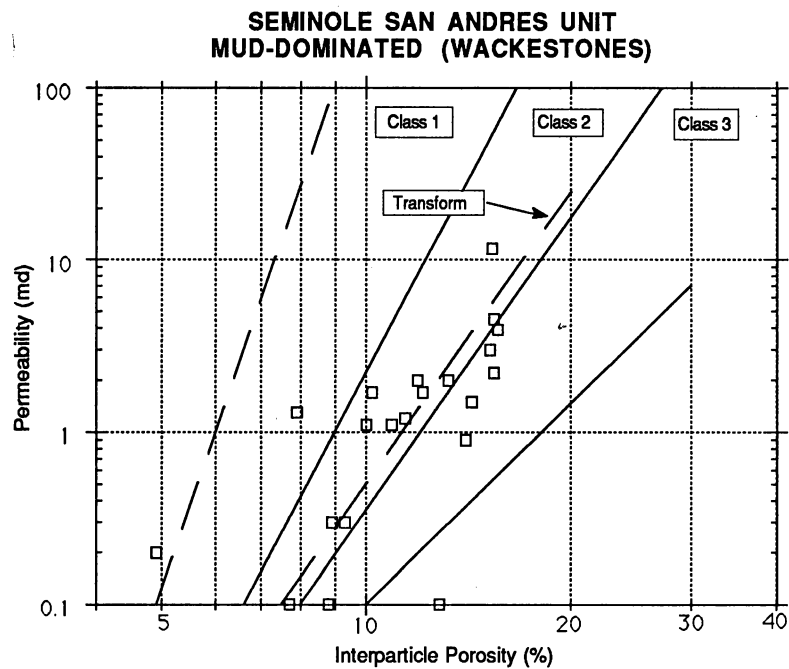
Figure 78. Porosity, permeability, rock-fabric transforms from selected plug samples, Seminole San Andres Unit. (a) Cross plot of interparticle porosity versus permeability for plug samples of grain-dominated packstone. (b) Cross plot of interparticle porosity versus permeability for plug samples of mud-dominated wackestone with 20-μm dolomite crystals. The three petrophysical/rock-fabric fields are shown for comparison.

136

Amerada Hess SSAU 2505
Seminole (San Andres) reservoir

Log	Matrix values		
	Dolomite	Anhydrite	Porosity
Density	2.87	2.95	1.00
Acoustic	43.5	50.0	150.0
CNL	4.0	-0.2	100.0

QA 15764c
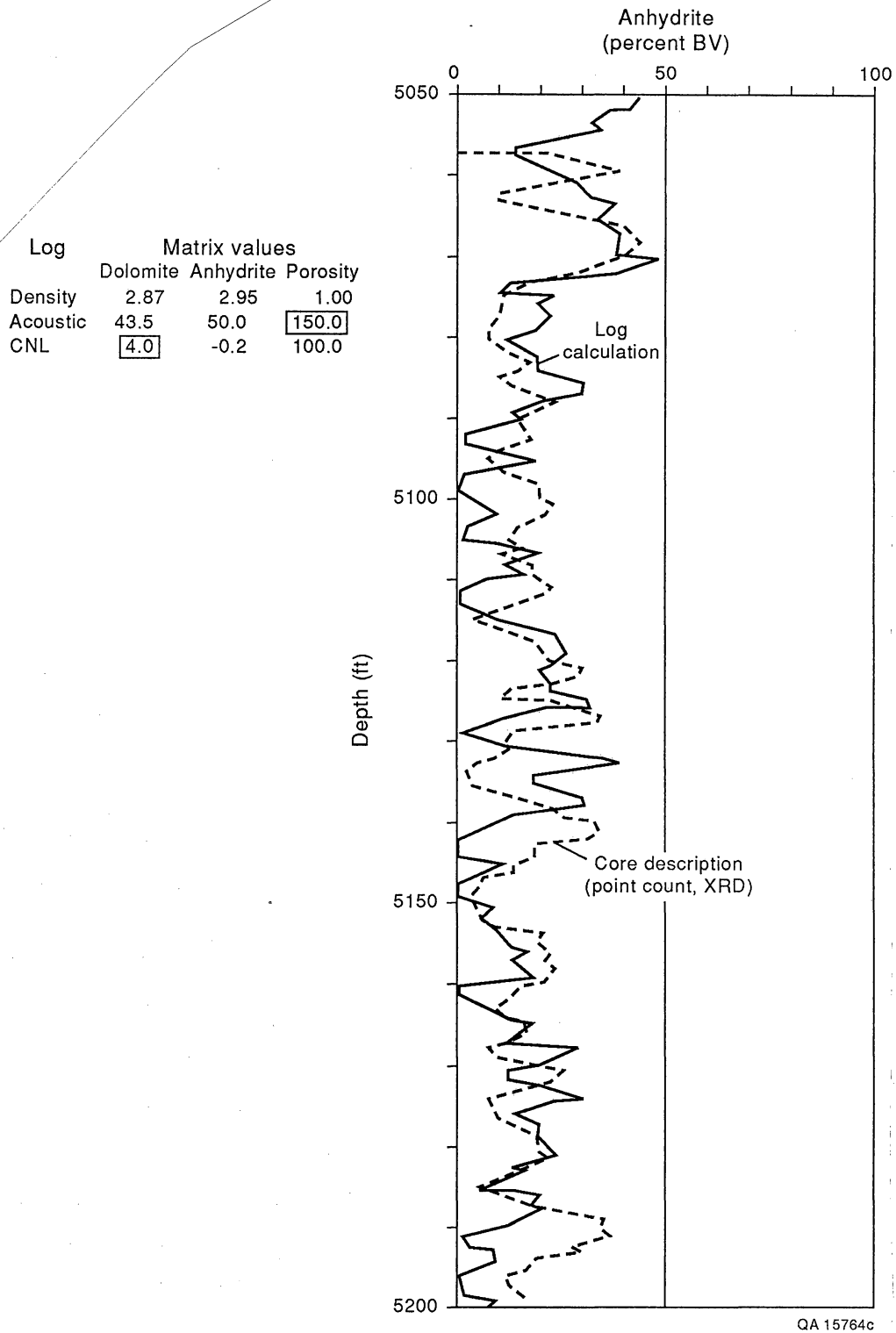
Figure 79. Comparison of log-calculated anhydrite volumes and anhydrite volumes from thin section descriptions in Amerada No. 2505 well, Seminole San Andres Unit.
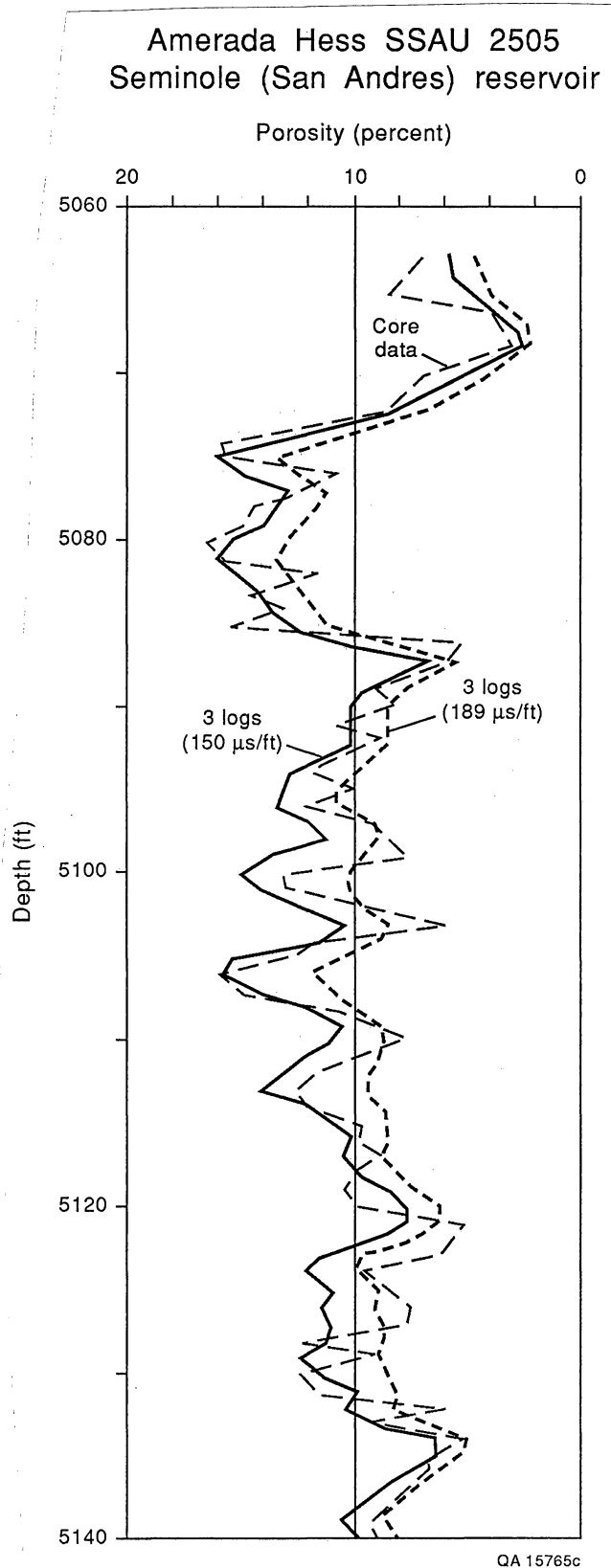
Figure 80. Comparison of porosity calculated from three porosity logs using 150 and 189 μs/ft with core-analysis porosity values in Amerada No. 2502 well, Seminole San Andres Unit.

Comparison of CNL limestone porosity values with porosity values from the plug samples suggests that true porosity is 4 porosity percent lower than CNL limestone porosity. Therefore, the neutron porosity parameter was reduced from 7.5 to 4. Using a value of 7.5 resulted in high anhydrite values. Table 9 presents the matrix values that showed the best fit between log analysis and anhydrite and corrected-porosity values from core analysis.

Calculation of separate-vug porosity

Interparticle porosity is calculated by subtracting separate-vug porosity from total porosity. In cores, the volume of separate vugs can be determined visually. In uncored intervals, the acoustic log can be used to estimate separate-vug porosity. To calibrate wireline log response with separate-vug porosity in the Seminole field, a 3-ft running average of the separate-vug porosity from thin-section analysis was calculated. A Z-plot of acoustic transit time, total porosity calculated from porosity logs, and separate-vug porosity from core description shows a systematic relationship (fig. 81).

The slope of the line relating transit time to porosity in figure 81 indicates a fluid transit time of about 150 μs/ft. Because no fluid has a travel time of 150 μs/ft, the faster travel time is probably related to the presence of separate-vug porosity. Acoustic waves respond to separate-vug porosity more like mineral than pore space. If no separate-vug porosity were present, or if separate-vug porosity were constant and did not vary with porosity, the slope of the line would indicate a fluid transit time of 189 μs/ft. Assuming this to be true, parallel lines with slopes equal to a fluid velocity of 189 μs/ft can be drawn representing various separate-vug values. The intercept of these lines with the transit time axis can be plotted against values of separate-vug porosity (fig. 82). A line connecting these points describes the semilog relationship between separate-vug porosity, total porosity, and interval transit time given in equation 10. This relationship applies to anhydritic dolomites only. A relationship for vuggy limestones developed by Lucia and Conti (1987) has a similar slope but a different intercept.

139

Table 9. Matrix values used for porosity log calculations.

Log	Matrix Values		
	Dolomite	Anhydrite	Porosity
Acoustic (μs/ft)	43.5	50.0	150
CNL (P.U.)	4	−0.2	100
Density (g/cc)	2.87	2.95	1.00
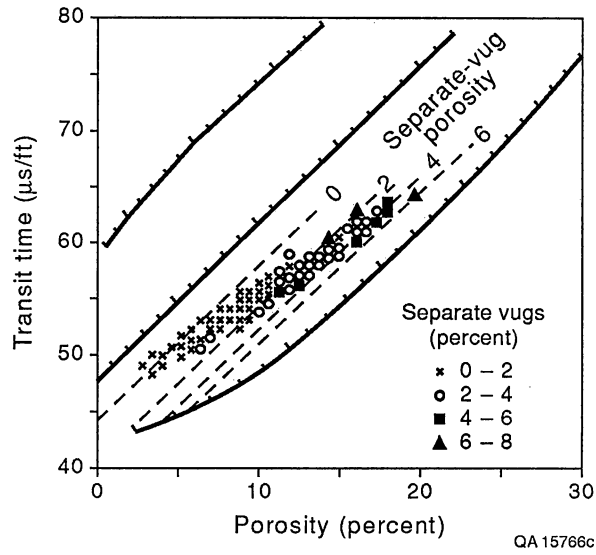
Figure 81. Relationship between transit time, total porosity, and separate-vug porosity in Amerada No. 2505 well, Seminole San Andres Unit.
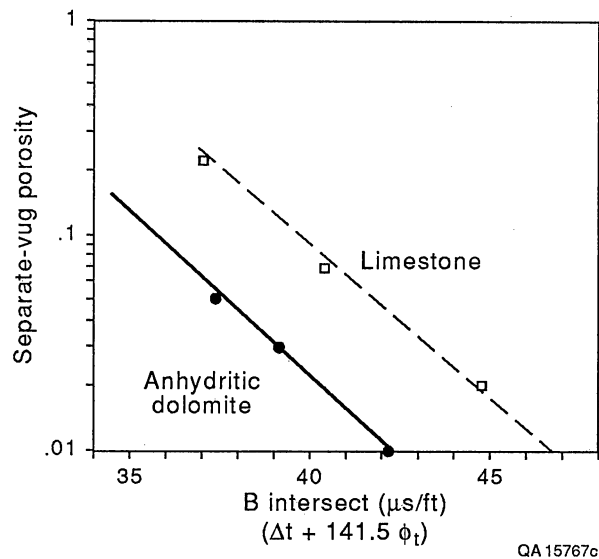
Figure 82. Transforms for separate-vug porosity, transit time, and total porosity for anhydritic dolomite and limestone. The dolomite transform is developed from Amerada No. 2505 well, Seminole San Andres Unit (fig. 81) and Conti (1987).

$$\phi_{sv} = (2.766 \times 10^{-4}) \, (10^{[-0.1526 \, (\Delta t - 141.5\phi)]}) \tag{10}$$

where

ϕ = total porosity (fraction)

ϕ_{sv} = separate-vug porosity (fraction)

Δt = interval transit time (μs/ft)

Using equation 10, separate-vug porosity is calculated from acoustic log values and calculated total porosity. In figure 83 the calculated separate-vug porosity and the 3-ft averages of the thin-section separate-vug values are compared in a depth plot. While the calculated values are in the correct range, the two profiles do not match well. This may be due to the difficulty in obtaining a reasonable value for separate-vug porosity from core descriptions or because of the inadequacy of the wireline logs in reflecting separate-vug porosity.

Calculation of rock fabric

Particle size and interparticle porosity control pore size and pore-size distribution. Water saturation can be calculated from wireline logs and is controlled by pore size and height above the free water table. In the Seminole field, cross plots of the log of porosity versus the log of water saturation can be used to determine particle size and rock fabric. Water saturation was calculated using the Archie equation. Water resistivity was determined to be 0.2 Ω-m, the saturation exponent n was assumed to be 2, and the lithology exponent m was calculated from the following relationship between separate-vug porosity and m:

$$m = 2.14 \left(\frac{\phi_{sv}}{\phi}\right) + 1.76 \tag{11}$$

Figure 84 shows that mud- and grain-dominated fabrics are clearly grouped into separate porosity-saturation fields. The data were obtained by averaging porosity and water saturation values for the mud- and grain-dominated intervals of ps1 through 8. The mud-dominated
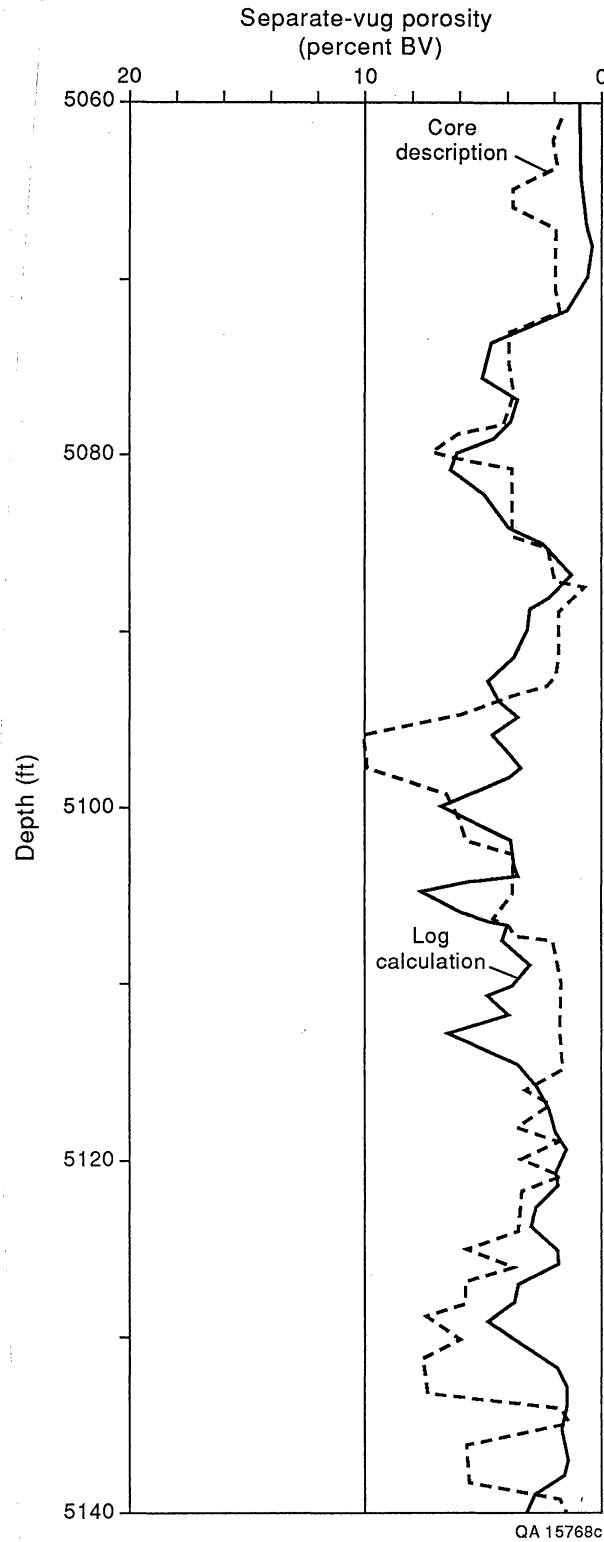
Figure 83. Comparison of separate-vug porosity calculated from logs with separate-vug porosity from core description in Amerada No. 2505 well, Seminole San Andres Unit.
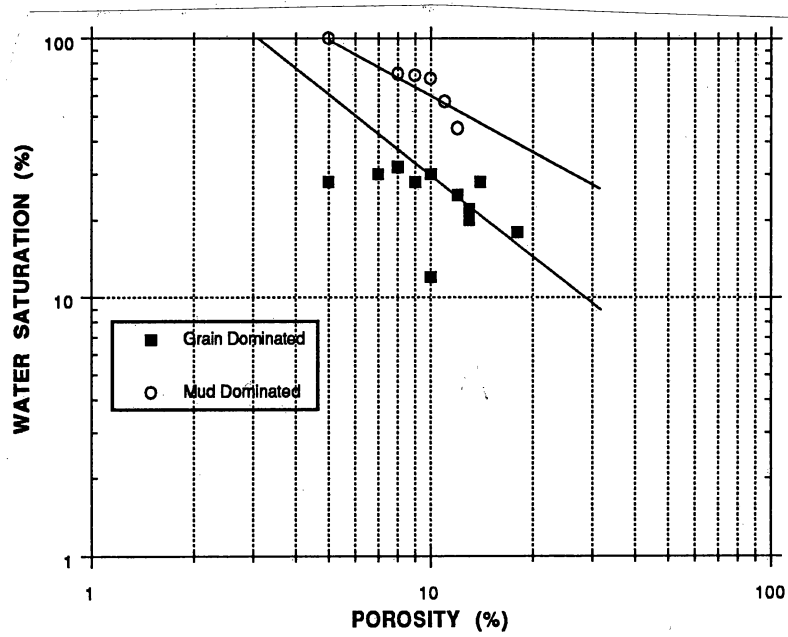
Figure 84. Porosity, water-saturation, rock-fabric cross plot for the upper productive interval in Amerada No. 2505 well, Seminole San Andres Unit, using averaged data from each parasequence.

interval of ps9 is a medium-crystal dolomite and is petrophysically similar to the grain-dominated fabrics.

A line interpolated between the points of figure 84 was used to separate mud- from grain-dominated fabrics. In addition, a line separating grain-dominated packstones from grainstones was added based on the presence of a few grainstone intervals. These lines which divide the porosity-saturation graph into three petrophysical rock-fabric fields are shown on figure 85 and the equations are presented in the following:

The boundary between mud-dominated (<20 μm) and grain-dominated fabrics is given as:

$$S_w = (3.05 \times 10^{-2}) \times (\phi^{-0.9813}) \tag{12}$$

The boundary between (1) grainstones and (2) grain-dominated packstone and medium-crystalline mud-dominated fabrics is given as:

$$S_w = (6.522 \times 10^{-3}) \times (\phi^{-1.401}) \tag{13}$$

Porosity, permeability, and rock-fabric transforms

Porosity, permeabiity, rock-fabric transforms were prepared using core permeability values and log-calculated porosity values. Log-calculated porosity values were used because the core porosity values are too low. Total porosity was converted into interparticle porosity by subtracting separate-vug porosity calculated from logs. The rock fabrics used to group the porosity and permeability data were determined from log analysis and checked by core descriptions. Figure 85 shows the data points used in the porosity-permeability plots shown in figure 86. The resulting transforms are:

Mud-dominated (<20 μm) fabrics

$$k(md) = (1.2303 \times 10^6) \times (\phi - \phi_{sv})^{5.90} \tag{14}$$

Grain-dominated packstones and medium crystal mud-dominated dolomites

$$k(md) = (6.6069 \times 10^9) \times (\phi - \phi_{sv})^{8.85} \tag{15}$$

146

QA 15769c
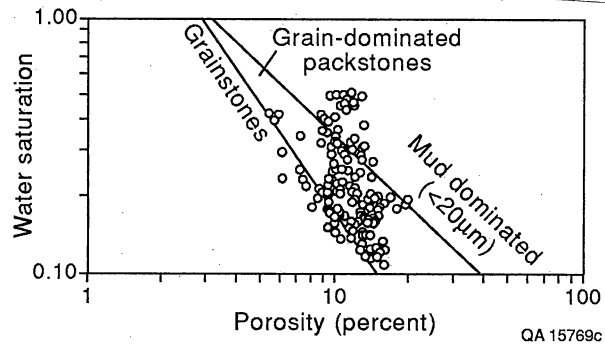
Figure 85. Porosity, water-saturation, rock fabric cross plot for the upper productive interval in Amerada No. 2505 well, Seminole San Andres Unit, based on 1-ft data points.

QA 15770c
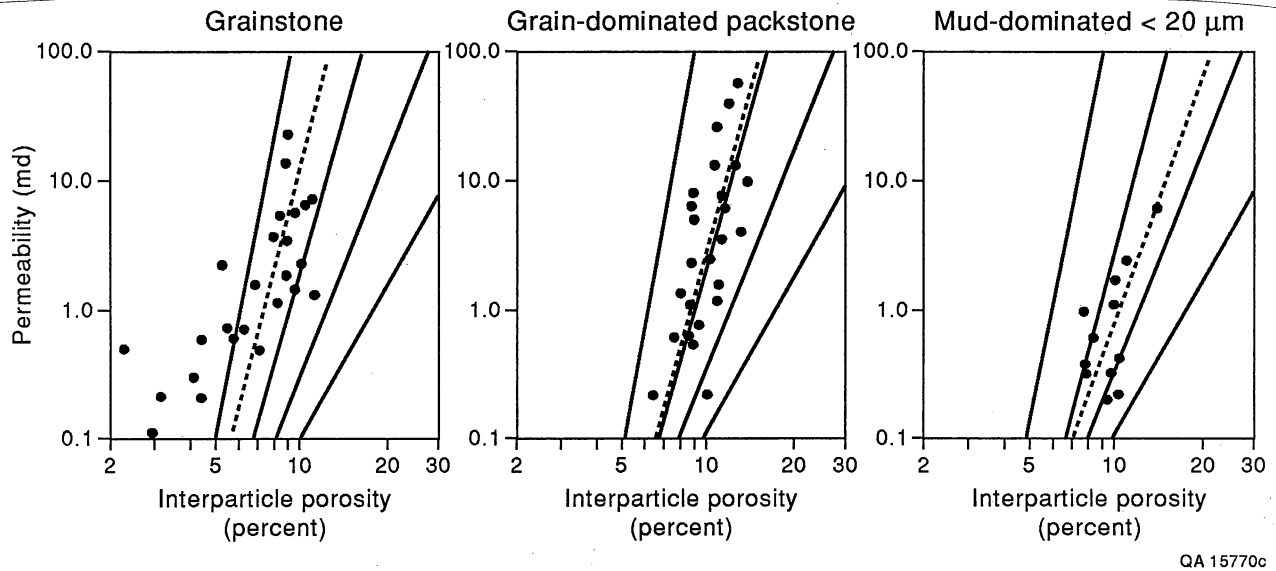
Figure 86. Porosity, permeability, and rock-fabric transforms from log calculations. The rock fabric is from porosity-water saturation relationships shown in figure 85, interparticle-porosity is from log calculations, and permeability is from core analysis. The transforms are based on the data points and on the geometry of the petrophysical/rock-fabric fields.

147

Grainstone fabrics

$$k(md) = (7.9432 \times 10^9) \times (\phi - \phi_{sv})^{8.75} \tag{16}$$

The transforms are similar to those determined from the core plugs (fig. 78) but are shifted slightly to the left. This suggests that either the log-calculated porosity values are still low by 1 to 2 porosity percent, or that the separate-vug porosity is too high by 1 to 2 porosity percent.

Permeability is calculated from wireline logs by (1) calculating total porosity from three porosity logs, (2) calculating separate-vug porosity from acoustic logs and total porosity, (3) calculating interparticle porosity by subtracting separate-vug porosity from total porosity, (4) calculating water saturation by the Archie method using separate-vug porosity to estimate the Archie m factor, (5) determining the rock fabric from saturation/porosity relationships, (6) selecting the proper rock-fabric transform, and (7) using interparticle porosity to calculate permeability.

The rock-fabric method of calculating permeability was tested in well 2309 located about 0.75 mi west of the Amerada No. 2505 control well (fig. 69). The results are shown in figure 87. The depth plots compare well except in four intervals where the calculated permeability is significantly higher than the core permeability. However, the total footage that does not compare well is 18 ft, 11 percent of the 160 ft tested. Causes of the poor comparison in the four intervals are being investigated.

Rock-Fabric Flow Model

The quantitative rock-fabric flow model of the two-section study area is illustrated in figure 88. The parasequence framework is based on core descriptions and log correlations. The rock fabrics are based on wireline log calculations that were compared with core descriptions. The permeability profiles are calculated from logs calibrated by core analysis and descriptions.

The flow model is similar to the Lawyer Canyon flow model shown in figure 26. Zones characterized by grain-dominated fabrics have the highest permeabilities and those

148
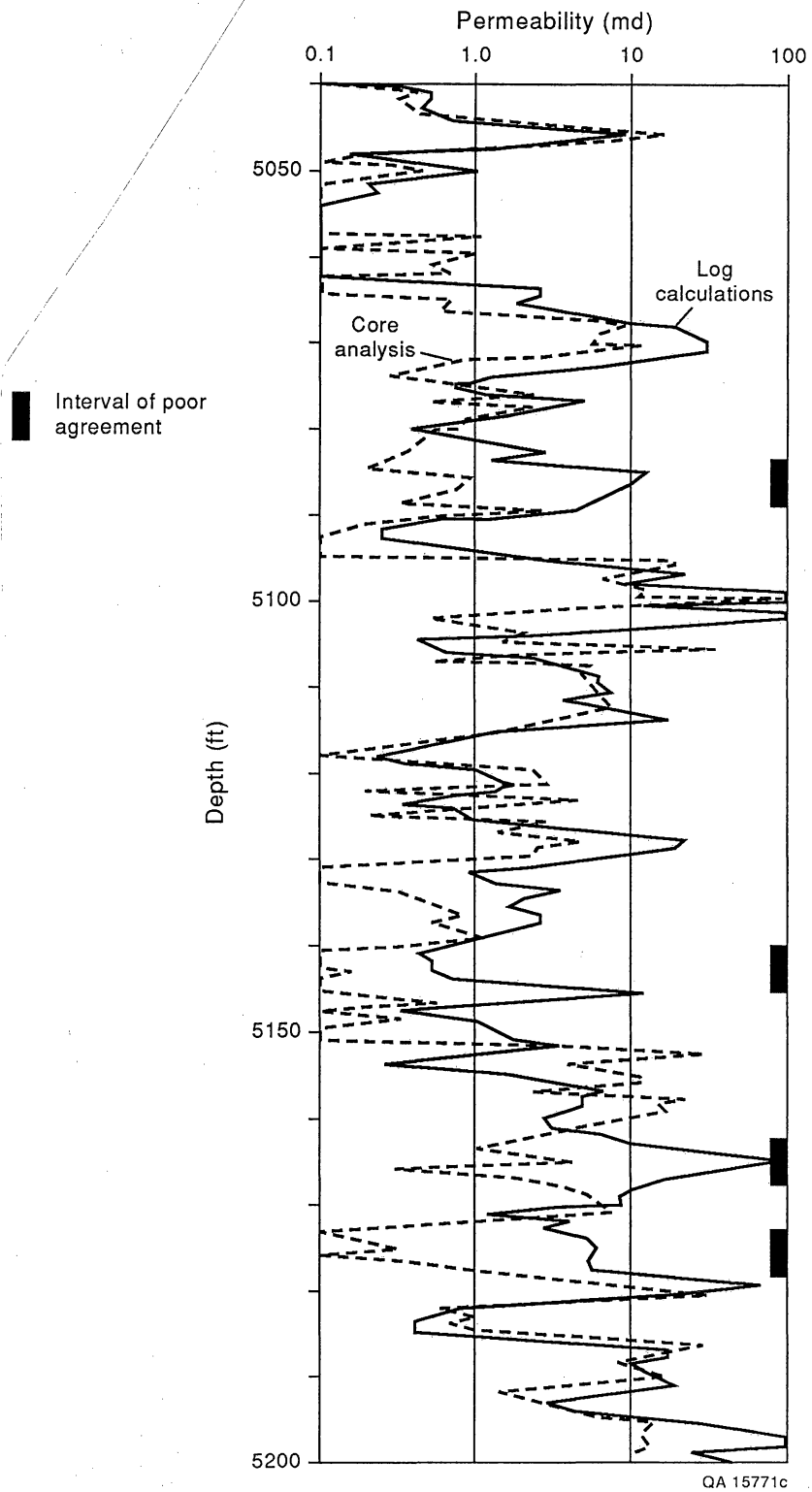
Figure 87. Comparison of permeability calculated from logs and permeability from core analysis in Amerada No. 2505 well, Seminole San Andres Unit. The four intervals where the difference in the two permeability values is greater than an order of magnitude are shown.

149
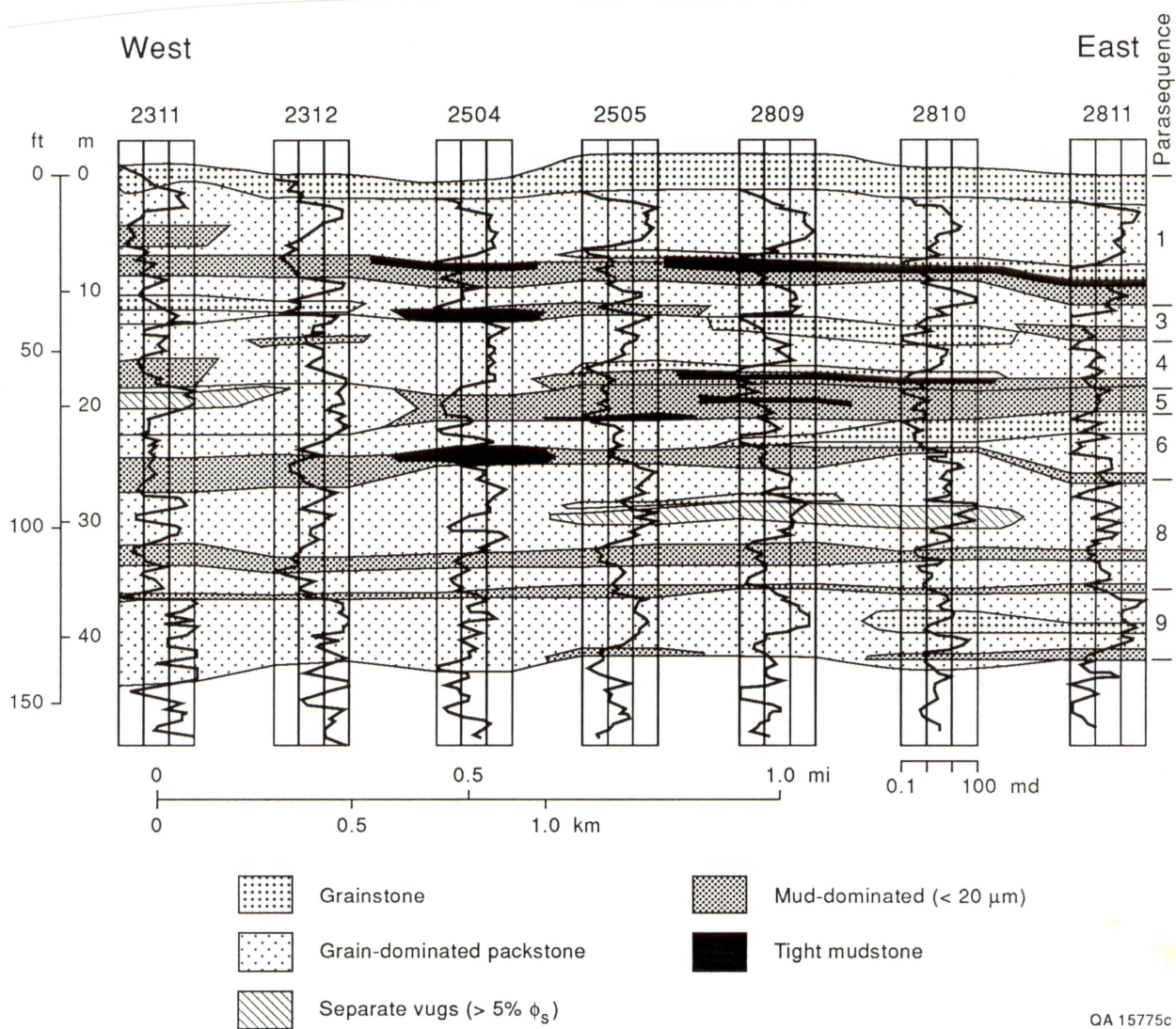
Figure 88. Cross section illustrating the rock-fabric flow model of the upper productive interval in the two-section study area of the Seminole San Andres Unit. Rock fabric and permeability of each well are from log calculations. Correlations are based on stratigraphic framework. See figure 69 for location of cross section.

150

characterized by mud-dominated fabrics have the lowest permeabilities. There are zones characterized by separate-vug porosity but they have limited extents. Tight mudstones (k = <0.1 md) are present at the base of some cycles but are discontinuous. All of these characteristics are similar to the Lawyer Canyon model. The principal difference is that there are few true grainstones and there is little lateral variation from grainstone to grain-dominated packstone to mud-dominated packstones and wackestones in the Seminole field flow model. This suggests that the upper productive interval of the study area in the Seminole field is in a lower energy depositional environment than the Lawyer Canyon Window. Perhaps because of the lower energy environment, depositional units composed of packstones and wackestones are more continuous than grainstone depositional units.

CONCLUSIONS

Geologic Framework

Outcrop analysis for evaluating styles and scales of reservoir heterogeneity of the San Andres Formation has demonstrated that the most effective way to characterize these complex and heterogeneous carbonates is through a combination of regional and highly detailed descriptions at sequence and parasequence scales. The parasequence approach is particularly useful for providing a meaningful framework for describing facies variability on a scale of 10's to 100's of ft laterally and from 1 to 10's of ft vertically. Specific results of the outcrop analysis are:

(1) The San Andres Formation of the Algerita Escarpment is divided into at least five sequences. The lower to middle San Andres is still considered a third-order sequence (lmSA1) as indicated by Sarg and Lehmann (1986). The upper San Andres third-order sequence is now divided into four fourth-order sequences (uSA1 through uSA4). The lmSA1 sequence is strongly aggradational, whereas upper San Andres sequences become increasingly progradational upwards and have 3- to 5-mi basinward shifts in ramp-crest position between highstands.

(2) Nine parasequences averaging 20 ft in thickness have been mapped continuously across the Lawyer Canyon upper San Andres ramp-crest parasequence window (140 by 2,600 ft). Each parasequence records a distinct episode of flooding and aggradation. Within these parasequences the bar-crest and -flank facies show the best reservoir quality and marked lateral variability in thickness.

(3) In the Lawyer Canyon middle San Andres outer ramp parasequence window, 15 upward-shallowing, -coarsening parasequences 15 to 40 ft thick are continuous across the 1,800-ft lateral dimension of the study area. The lower 10 parasequences are defined largely by subtle changes from wackestone to packstone, whereas the upper 5 have distinctive mud-rich wackestone to mudstone bases and packstone to grain-dominated packstone caps.

(4) Outer ramp parasequences of the Irabarne Tank upper San Andres parasequence window are comparable to those at Lawyer Canyon, consisting of fusulinid wackestones and packstones. These parasequences were deposited on an outer ramp surface that dipped 1° to 2° basinward, but little change in depositional texture is observed within parasequences across the 1,300-ft study area.

The geologic characterization methods developed in the outcrop phase of the study, and used at the Seminole San Andres Unit, showed that the parasequence framework is useful in developing a detailed genetically based zonation using both geologic facies and key log markers to subdivide the reservoirs. Specific conclusions related to the geologic part of the Seminole study are:

(1) The sequence-stratigraphic framework of the Seminole San Andres is comparable to that developed along the Algerita Escarpment, including development of a thick lower to middle San Andres sequence (minimum 850 ft), followed by a rapidly shallowing succession of parasequences (800 ft) that are the record of the four upper San Andres sequences of the outcrop model.

(2) The 250-ft main-pay interval contains 11 upward-shallowing parasequences that together define an upward-shallowing, -thinning parasequence set. This parasequence set

152

probably contains parts of at least two of the San Andres sequences defined in outcrop, probably the uppermost lmSA1 and the uSA1.

(3) Greatest lateral heterogeneity of facies appears in the upper five parasequences of the reservoir where grain-dominated intervals <1 to 20 ft thick are commonly continuous for only one or two well spacings.

Quantification of Geologic Framework

One of the most significant problems in reservoir characterization is quantification of the geologic framework in terms of petrophysical parameters. Petrophysical parameters of porosity, permeability, and capillarity can be related to rock fabrics through descriptions of interparticle porosity, particle size and sorting, separate-vug porosity, and touching-vug porosity. These fabrics can be related to stratigraphic models through depositional and diagenetic processes. The results of this study show that, although petrophysical properties vary on a scale of inches, particle size and sorting are relatively constant on the scale of 100's to 1,000's of ft, providing a useful method for mapping petrophysical parameters.

Mapping the distribution of rock fabrics within the parasequence framework provides the key element needed to quantify the geologic framework in petrophysical terms. Previous work has shown that rock fabrics can be grouped into three petrophysical rock-fabric classes. These are (1) grainstones, dolograinstones with any size of dolomite crystals, and mud-dominated dolomites with large crystal sizes (>100 μm); (2) grain-dominated packstones, both limestones and dolomites with fine to medium crystal sizes (<100 μm), plus medium crystal mud-dominated dolomites; and (3) mud-dominated limestones and dolomites with fine crystal sizes (<20 μm).

Conclusions related to rock fabrics resulting from this study are:

(1) The rock fabrics described both from the Lawyer Canyon Window and from the upper productive interval of Seminole San Andres Unit are (a) dolomitized grainstones, (b) fine to medium crystalline dolomitized grain-dominated packstones, and (c) fine crystalline mud-

dominated dolomites. These fabrics are stacked systematically vertically and laterally within a parasequence.

(2) The fusulinid-rich clinoform cycles in the Irabarne Tank Window and the fusulinid-rich lower productive interval in Seminole San Andres Unit are characterized by medium crystalline dolograin-dominated packstones and dolomud-dominated fabrics.

(3) Each petrophysical rock-fabric class can be characterized by a porosity-permeability transform and a porosity-saturation-reservoir-height transform. These relationships are used to quantify the outcrop geologic frameworks.

(4) In the Seminole San Andres Unit reservoir, core descriptions and wireline log calculations can be used to develop predicable relationships between water saturation, porosity, and three rock-fabric classes. A porosity-permeability transform developed for each class creates a more accurate estimation of permeability.

(5) Developed as part of this study, a new method for calculating separate-vug porosity using interval transit time and total porosity provides a more accurate measure of interparticle porosity needed to estimate permeability from rock-fabric specific porosity-permeability transforms.

The permeability structure within a rock-fabric unit was investigated geostatistically and the significance of the results tested using a reservoir simulator. The main conclusions of this research are

(1) Variogram analysis of grid permeability data from the grainstone rock-fabric unit of ps1 and moldic-grainstone rock-fabric unit of ps7 shows a near-random permeability distribution on a scale of 10's of ft. This distribution suggests that mean values of petrophysical parameters can be used to characterize rock-fabric units.

(2) Waterflood simulations of ps1, comparing averaged data with conditional simulation data, showed little difference in production performance indicating that averaged data for rock-fabric units are sufficient for input into reservoir simulators.

154

(3) Variogram analysis of widely spaced data suggested a permeability structure on a scale of 100's of ft. The Irabarne Tank data show statistically different permeability populations 500 ft apart. Initial waterflood simulation runs indicate that at this scale permeability structure has a significant effect on production performance and should not be averaged out.

Simulation Results

Reservoir-flow simulations of the entire Lawyer Canyon Window underscore the importance of knowing the facies architecture between wells. Results from this research show that the spatial distribution of facies relative to the waterflood direction can significantly affect how the reservoir produces.

(1) Comparing the standard approach to subsurface reservoir model of linear interpolation of properties between wells with the detailed outcrop model shows that the standard approach overestimates the cumulative oil production.

(2) An important mechanism for bypassing unswept oil is cross flow of injected water across low-permeability mudstones where high permeability zones terminate. An area of unswept oil develops because of the slower advance of the water-injection front in the adjacent flow units.

(3) When the injection pattern is reversed, the cross-flow effect becomes more dominant and a greater area of unswept oil develops. Comparison of production characteristics indicates that simply changing the waterflood direction affects sweep efficiency.

(4) The simulations further document that although the parasequence boundaries, represented by mudstone-wackestone units, strongly control waterflooding, these low-permeability mudstone layers do not necessarily represent flow barriers but can allow for significant cross flow.

155

ACKNOWLEDGMENTS

REFERENCES

Back, W., Hanshaw, B. B., Plummer, L. N., Rahn, P. H., Rightmire, C. T., and Rubin, M., 1983, Process and rate of dedolomitization: Mass transfer and ^{14}C dating in a regional carbonate aquifer: Geological Society of American Bulletin, v. 94, no. 12, p. 1415–1429.

Bebout, D. G., Lucia, F. J., Hocott, C. R., Fogg, G. E., and Vander Stoep, G. W., 1987, Characterization of the Grayburg reservoir, University Lands Dune field, Crane County, Texas: The University of Texas at Austin, Bureau of Economic Geology Report of Investigations No. 168, 98 p.

Craig, D. H., 1988, Caves and other features of Permian karst in San Andres Dolomite, Yates Field Reservoir, West Texas, in James, N. P., and Choquette, P. W., eds., Paleokarst: New York, Springer-Verlag, p. 342–363.

Dunham, R. J., 1963, Classification of carbonate rocks according to depositional texture, in Ham, W. E., ed., Classification of carbonate rocks: American Association of Petroleum Geologists Memoir 1, p. 108–121.

Fogg, G. E., 1989, Stochastic analysis of aquifer interconnectedness, Wilcox Group, Trawick area, East Texas: The University of Texas at Austin, Bureau of Economic Geology Report of Investigations No. 189, 68 p.

Goggin, D. J., Thrasher, R. L., and Lake, L. W., 1988, A theoretical and experimental analysis of minipermeameter response including gas slippage and high velocity flow effects: In situ, v. 12, no. 1/2, p. 79–116.

Harris, P. M., Dodman, C. A., and Bliefnick, D. M., 1984, Permian (Guadalupian) reservoir facies, McElroy field, West Texas, *in* Harris, P. M., ed., Carbonate sands—a core workshop: Society of Economic Paleontologists and Mineralogists Core Workshop No. 5, p. 136–174.

Hayes, P. T., 1964, Geology of the Guadalupe Mountains, New Mexico: U.S. Geological Survey Professional Paper 446, 69 p.

Hinrichs, P. D., Lucia, F. J., and Mathis, R. L., 1986, Permeability and reservoir continuity in Permian San Andres shelf carbonates, Guadalupe Mountains, New Mexico, *in* Moore, G. E., and Wilde, G. L., eds., lower and middle Guadalupian facies, stratigraphy, and reservoir geometries, San Andres-Grayburg Formations, Guadalupe Mountains, New Mexico and Texas: Society of Economic Paleontologists and Mineralogists, Permian Basin Section, Publication No. 86-25, p. 37–47.

_____ 1987, Permeability distribution and reservoir continuity in Permian San Andres shelf carbonates, Guadalupe Mountains, New Mexico, *in* Moore, G. E., and Wilde, G. L., eds., Lower and Middle Guadalupian facies, stratigraphy and reservoir geometries, San Andres-Grayburg Formations, Guadalupe Mountains, New Mexico and Texas: Society of Economic Paleontologists and Mineralogists, Permian Basin Section, Publication No. 86-25, p. 37–48.

Honarpour, M., Koederitz, L., and Harvey, A. H., 1986, Relative permeability of petroleum reservoirs, Boca Raton, Florida: CRC Press, 143 p.

James, N. P., 1977, Facies models 8; shallowing upward sequences in carbonates: Geoscience Canada, v. 4, p. 126–136.

Journel, A. G., and Huijbregts, Ch. J., 1978, Mining geostatistics: New York, Academic Press, 600 p.

King, P. B., 1948, Geology of the southern Guadalupe Mountains, Texas: U.S. Geological Survey

   Professional Paper 480, 183 p.

Kittridge, M. G., Lake, L. W., Lucia, F. J., and Fogg, G. E., 1990, Outcrop-subsurface comparisons of

   heterogeneity in the San Andres Formation: Society of Petroleum Engineers, 64th Annual

   Technical Conference, SPE 19596.

Longacre, S. A., 1980, Dolomite reservoirs from Permian biomicrites, in Halley, R. B., and Loucks,

   R. G., eds., Carbonate reservoir rocks: Society of Economic Paleontologists and Mineralogists

   Core Workshop No. 1, p. 105–117.

Lucia, F. J., 1961, Dedolomitization in the Tansill (Permian) formation: Geological Society of

   America Bulletin, v. 72, no. 7, p. 1107–1109.

_____ 1983, Petrophysical parameters estimated from visual descriptions of carbonate rocks: A

   field classification of carbonate pore space: Journal of Petroleum Technology, v. 35, no. 3,

   p. 629–637.

Lucia, F. J., and Conti, R. D., 1987, Rock fabric, permeability, and log relationships in an upward-

   shoaling, vuggy carbonate sequence: The University of Texas at Austin, Bureau of Economic

   Geology Geological Circular 87-5, 22 p.

Moore, G. E., and Wilde, G. L., eds., 1986, Lower and Middle Guadalupian facies, stratigraphy, and

   reservoir geometries, San Andres-Grayburg Formations, Guadalupe Mountains, New Mexico

   and Texas: Society of Economic Paleontologists and Mineralogists, Permian Basin Section,

   Publication No. 86-25, p. 1–36.

Ruppel, S. C., and Cander, H. S., 1988, Effects of facies and diagenesis on reservoir heterogeneity: Emma San Andres field, West Texas: The University of Texas at Austin, Bureau of Economic Geology Report of Investigations No. 178, 67 p.

Sarg, J. F., and Lehmann, P. J., 1986, Lower-middle Guadalupian facies and stratigraphy, San Andres-Grayburg Formations, Permian Basin, Guadalupe Mountains, New Mexico, *in* Moore, G. E., and Wilde, G. L., eds., Lower and middle Guadalupian facies, stratigraphy and reservoir geometries, San Andres-Grayburg Formations, Guadalupe Mountains, New Mexico and Texas: Society of Economic Paleontologists and Mineralogists, Permian Basin Section, Publication No. 86-25, p. 1–36.

Van Wagoner, J. C., Posamentier, H. W., Mitchum, R. M., Jr., Vail, P. R., Sarg, J. F., Loutit, T. S., and Hardenbol, J., 1988, An overview of the fundamentals of sequence stratigraphy and key definitions, *in* Wilgus, C. K., Hastings, B. S., Kendall, C. G. St. C., Posamentier, H. W., Ross, C. A., and Van Wagoner, J. C., eds., Sea-level changes: an integrated approach, Society of Economic Paleontologists and Mineralogists, Special Publication No. 42, p. 39–46.

Wilson, J. L., 1975, Carbonate facies in geologic history: New York, Springer-Verlag, 471 p.

Yates, S. R., and Yates, M. V., 1990, Geostatistics for waste management: A user's manual for the GEOPACK (Version 1.0) Geostatistical Software System: U.S. Environmental Protection Agency Report EPA/600/8-90/004, 70 p.